ARTICLE

Synaptopodin stress fiber and contractomere at the epithelial junction

Timothy Morris[1] , Eva Sue[1] , Caleb Geniesse[1] , William M. Brieher[1] , and Vivian W. Tang[1]

The apical junction of epithelial cells can generate force to control cell geometry and perform contractile processes while maintaining barrier function and adhesion. Yet, the structural basis for force generation at the apical junction is not fully understood. Here, we describe two synaptopodin-dependent actomyosin structures that are spatially, temporally, and structurally distinct. The first structure is formed by the retrograde flow of synaptopodin initiated at the apical junction, creating a sarcomeric stress fiber that lies parallel to the apical junction. Contraction of the apical stress fiber is associated with either clustering of membrane components or shortening of junctional length. Upon junction maturation, apical stress fibers are disassembled. In mature epithelial monolayer, a motorized "contractomere" capable of "walking the junction" is formed at the junctional vertex. Actomyosin activities at the contractomere produce a compressive force evident by actin filament buckling and measurement with a new α-actinin-4 force sensor. The motility of contractomeres can adjust junctional length and change cell packing geometry during cell extrusion and intercellular movement. We propose a model of epithelial homeostasis that utilizes contractomere motility to support junction rearrangement while preserving the permeability barrier.

Introduction

Epithelial cells cover body cavities and line internal organs, providing continuous protection from biological, chemical, and mechanical insults. The maintenance, stability, and physiological functions of an epithelium require the assembly of a specialized cell–cell junction known as the apical junction. Epithelial apical junction provides adhesions between cells, forms a permeability barrier against macromolecules and microorganisms, and regulates epithelial cell packing and geometry. Force exerted by the epithelial junction can not only reshape cell boundaries and adjust junctional length but also facilitate cell rearrangement during dynamics processes, including wound migration and morphogenesis (Pinheiro and Bellaiche, 2018). Moreover, junction contractility is necessary for cell extrusion and purse-string wound closure, which are essential for epithelial homeostasis (Bement et al., 1993; Clark et al., 2009; Danjo and Gipson, 1998; Florian et al., 2002).

Force generation at the junction depends on myosin II, a >300 nm bipolar minifilament consisting of anti-parallel arrangement of barbed-end-directed myosin II motors. Activation of junctional contractility results in shortening of the junction and destabilizes E-cadherin adhesions (Cavanaugh et al., 2020). In contrast, the application of orthogonal force to the junction results in the strengthening of E-cadherin adhesions (Gomez et al., 2011; Kannan and Tang, 2015; Kannan and Tang, 2018; Katayama et al., 2010). Thus, the biological outcome of force at the junction appears to depend on the orientation of the applied force, which is the directional information embedded within the force vector.

What is the molecular and structural basis that allows the generation of orthogonal and parallel force at the apical junction? How does the cell organize actomyosin populations to control the direction of force? Can the junction pull on actin filaments or is the junction being pulled by actomyosin? Do we know whether contractile force is generated at the junction or is the junction on the receiving end of cytoplasmic force? At least two actomyosin structures could exert orthogonal force on the apical junction. The apical–medial actomyosin meshwork in polarized epithelial cells can generate isotropic contractile force, pulling the junction orthogonally (Roper, 2015). Contraction of cytoplasmic actomyosin network also can exert a force on cell–cell adhesions (Kannan and Tang, 2015; Wu et al., 2014). Myosin IIA is organized into actin cables underneath the junction, whereas myosin IIB is found on membrane adhesions. Contractions of these two actomyosin populations could exert a

[1]Department of Cell and Developmental Biology, University of Illinois, Urbana-Champaign, IL.

Correspondence to Vivian W. Tang: vtang@illinois.edu

A preprint of this paper was posted in bioRxiv on September 30, 2021.

parallel force on the junction (Heuze et al., 2019). Earlier studies have shown that myosin IIB controls actin accumulation whereas myosin IIA regulates E-cadherin stability (Smutny et al., 2010). Furthermore, myosin IIB, but not myosin IIA, plays a role in α-catenin mechanoregulation (Heuze et al., 2019). Myosin IIB has a higher duty ratio than myosin IIA, and its rate-limiting step is regulated by both ADP release and Pi release (Kovacs et al., 2003; Rosenfeld et al., 2003). It has been postulated that the ratio of myosin IIA and IIB embedded within the same actomyosin structure could affect the overall biophysical properties of the structure (Beach et al., 2014). Indeed, differential regulation of myosin IIA and IIB could differentially affect filament assembly, localization, and actomyosin mechanical properties in cells (Dulyaninova and Bresnick, 2013; Ecsedi et al., 2018; Kuragano et al., 2018; Melli et al., 2018; Sato et al., 2007).

In this paper, we describe 2 novel actomyosin structures, apical stress fiber and a myosin II motorized organelle we name "contractomere." We provide evidence for an essential molecular component, synaptopodin, for their assembly. We have generated a novel α-actinin-4 tension sensor to show that the junction and the contractomere experience compressive force in the homeostatic epithelial cell monolayer.

Results

To understand how actomyosin organization contributes to force generation at the epithelial junction, we focused on three actin-binding proteins, α-actinin-4, synaptopodin, and myosin IIB, which are known regulators of cellular contractility (Asanuma et al., 2005; Hotulainen and Lappalainen, 2006; Kannan and Tang, 2015; Mundel et al., 1997; Solinet and Vitale, 2008). Synaptopodin is a vertebrate-specific protein expressed ubiquitously in humans (Uhlen et al., 2015). Using antibodies against different spliced regions, we showed that epithelial and endothelial cells express different variants of synaptopodin (Fig. S1 A). Synaptopodin decorates the apical junction and stress fibers of epithelial and endothelial cells (Fig. S1 B). In MDCK cells, synaptopodin, α-actinin-4, and myosin IIB form a network of stress fibers connecting cell–cell adhesions across multiple cells (Fig. S2, A and B). Thin-section electron microscopy of T84 intestinal epithelial cells revealed that apical stress fiber with distinctive "sarcomere" is attached via actin thin-filaments to the apical junction (Fig. S2 C). In this study, we focus on synaptopodin–actomyosin structures at the apical junction of MDCK cells.

Organization of two novel actomyosin structures at the apical junction

MDCK cell monolayers grown on Transwells develop apical junctions with strong cell–cell adhesion and a robust permeability barrier (Kannan and Tang, 2015). We grew MDCK cells on Transwells and compared their actomyosin structures at various stages of junction development using super-resolution microscopy. At an early stage of junction development, myosin IIB and synaptopodin exhibit a periodic and alternating pattern (Figs. 1 A, S1 B, and S2 A). Apical stress fibers are positioned parallel to

the junction and spatially separated from E-cadherin junctions, except at points of insertion (Fig. 1 A, orange arrowheads). This is analogous to basal stress fibers where attachments at focal adhesions occur at the ends of stress fibers. An alternating pattern of myosin II and α-actinin is a signature organization for contractile stress fibers (Naumanen et al., 2008; Pellegrin and Mellor, 2007). During junction development, apical stress fibers form side-on interactions with the apical junction via synaptopodin linkers (Fig. 1 B, arrowheads). Upon association with E-cadherin junctions, apical stress fibers become less organized, and the characteristic sarcomeric-repeats are less recognizable. As junctions mature over time, the alternating pattern of myosin IIB and synaptopodin completely dissolves (Fig. 1 C). Concomitantly, E-cadherin, myosin IIB, and synaptopodin accumulate at the ends of linear junctions, also known as junction vertices. Upon maturation of the epithelial monolayer, apical stress fibers are absent, and a novel complex containing myosin IIB, synaptopodin, and α-actinin-4 is formed at junction vertices (Fig. 1 D). We refer to these two structures as "type I" when myosin IIB and synaptopodin are arranged in an alternating pattern and "type II" when they overlap (Fig. 1 E). We termed the type II structure as "contractomere" since it has not been described before; "contracto" refers to the contractile activity of myosin II that can pull on actin filaments during isometric, eccentric, or concentric contraction and "mere" refers to it being a standalone structure that can be isolated biochemically. The goal of this study is to determine whether these actomyosin assemblies are associated with junctional processes and whether synaptopodin is required for their assembly.

Synaptopodin stress fibers are inserted at both apical and basal junctions

Synaptopodin has emerged as one of the best markers for actin cytoskeletal structures. To image stress fiber dynamics at the apical junction, we co-expressed synaptopodin with ZO-1 (Figs. 2 A and S3 A), which is a junction protein that interacts with synaptopodin and α-actinin-4 (Chen et al., 2006; Van Itallie et al., 2013). ZO-1 has previously been shown to decorate apical and basal junctions (Anderson et al., 1988; Danjo and Gipson, 1998; Millan et al., 2010; Tornavaca et al., 2015). In MDCK monolayers, synaptopodin apical stress fibers (Fig. 2 A, blue box) are spatially segregated from synaptopodin basal stress fibers (Fig. 2 A, yellow box). Both apical and basal stress fibers can attach to the junction via end-on interactions (Figs. 2 A and S3 A). When an apical stress fiber is attached head-on, the junction would experience orthogonal force. Live-imaging shows that contractions of end-on apical stress fibers are associated with junction shortening (Fig. 2, B and C; and Video 1) and cell-shape changes (Fig. 2 D and Video 2).

We also imaged synaptopodin with vinculin, a junction marker in epithelial and endothelial cells (Efimova and Svitkina, 2018; Huveneers et al., 2012; Katayama et al., 2010; Kobielak et al., 2004; Schnabel et al., 1990; Tornavaca et al., 2015; Twiss et al., 2012; Zhang et al., 2005). In sparsely-plated MDCK cells, synaptopodin stress fibers are inserted end-on at vinculin-decorated basal junctions and focal adhesions on the basal focal plane (Fig. S3 B).
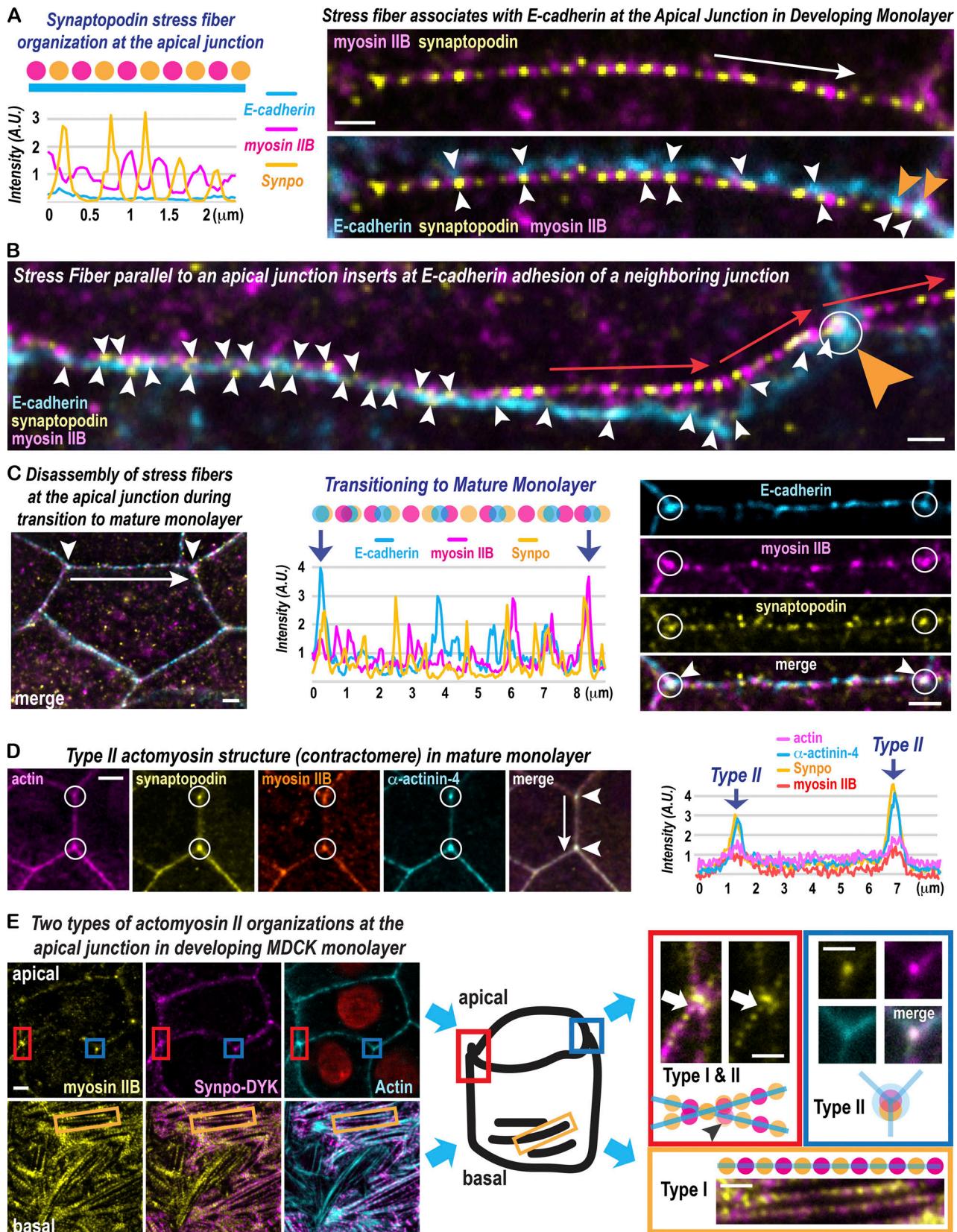
Figure 1. Superresolution microscopy of two actomyosin structures at the apical junction. (A) Apical stress fiber has an alternating myosin IIB and synaptopodin pattern and lies parallel to the E-cadherin junction. Orange arrowheads point to the end of an apical stress fiber marked by E-cadherin. White arrowheads point to junctional regions where synaptopodin is in proximity to E-cadherin. White long arrow shows the stretch of junction used for the x-axis of the graph. Scale bar is 500 nm. **(B)** Apical stress fiber is inserted head-on to E-cadherin junction, marked by an orange arrowhead. Synaptopodin overlaps with

E-cadherin at the insertion point of the stress fiber, in white circle. White arrowheads mark the sites where synaptopodin is in proximity to or overlapping with E-cadherin. Scale bar is 500 nm. **(C)** Disassembly of apical stress fibers in maturing junction leads to loss of alternating pattern of synaptopodin and myosin IIB. Disassembly of apical stress fiber coincides with formation of type II actomyosin structures containing myosin IIB, synaptopodin, and α-actinin-4, marked by white arrowheads on the left panel and blue arrows in graph. White long arrow on the left panel shows the stretch of junction used for the x-axis of the graph. White circles in the right panels show type II structures and white arrowheads in the right panels mark the colocalization of myosin IIB, synaptopodin, α-actinin-4. Scale bars are 1 µm. **(D)** Apical stress fibers disappear upon junction maturation whereas type II actomyosin structures are prominent at mature apical junctions. Actin accumulates at type II actomyosin structure, circled in white, colocalizing with myosin IIB, synaptopodin (Synpo), and α-actinin-4, as marked by white arrowheads. Graph shows the absence of apical stress fiber and the presence type II structure, named contractomere. White long arrow shows the stretch of the junction used for x-axis of the graph. Scale bar is 1 µm. **(E)** Two actomyosin structures at the apical junction of MDCK cells. Apical stress fibers are labeled as Type I actomyosin structures with alternating synaptopodin and myosin IIB organization. In maturing junction, Type I apical stress fiber coexists with Type II contractomeres with overlapping synaptopodin (Synpo-DYK) and myosin IIB. White arrows point to synaptopodin colocalizing with myosin IIB. Basal stress fibers have alternating synaptopodin and myosin IIB organization, same as Type I apical stress fibers. Scale bars are 1 µm.

Retrograde flow of synaptopodin during stress fiber assembly

In a developing monolayer, synaptopodin is continuously incorporated at the basal junctions, creating a retrograde flow of synaptopodin along the long axis of basal stress fibers (Fig. S4, A–C and Videos 3, 4, and 5). In polarized cells, basal stress fibers are several microns away from apical stress fibers on a different focal plane (Fig. S4 D). On the apical plane, retrograde flow of synaptopodin is initiated at the apical junction (Fig. S5 A and Videos 6, 7, and 8). In contrast to the basal junction, synaptopodin retrograde flow from the apical junction gives rise to stress fibers that are parallel to the junction; this is a 90° change in the orientation of the stress fibers with respect to the direction of synaptopodin flow (Fig. 3 A and Video 9), implying different mechanisms for stress-fiber assembly at the apical and basal junctions.

Contractility and evolution of apical stress fibers during junction maturation

As the junction develops over the next few days, retrograde synaptopodin flow ceases. Synaptopodin apical stress fibers now exhibit contractility, resulting in local clustering of junctional components (Figs. 3 B, S5 B, and Videos 10, 11, 12, and 13). In the following few days, synaptopodin apical stress fibers begin to flow toward junction vertices (Fig. 3 C; and Videos 14 and 15). At the vertices, nascent contractomeres move against the direction of synaptopodin flow, implicating that an energy-driven process is at play at the contractomere (Fig. 3 D). The motility of a contractomere can shorten a junction while simultaneously lengthen an adjacent junction (Fig. S5 C and Video 17). Two contractomeres flanking a junction can shorten the junction by moving toward each other (Video 16). This behavior coincides with the dissolution of synaptopodin stress fibers and the assembly of contractomeres in mature monolayers (Fig. S6, A and B), a type II structure that we have described earlier in Fig. 1. In developing and mature MDCK monolayers, vinculin is absent from the apical junction (Fig. S6, C and D).

Contractomere motility in a developing monolayer

To understand the relationship between contractomere motility and cell geometry, we performed live-cell structured-illumination microscopy (Fig. 4 A). In maturing monolayers, individual cells move among each other while maintaining the same neighbors (Fig. 4 A, lower panels). By tracking individual contractomeres, we found no directional bias in the movement of the contractomeres (Fig. 4 A, top panels). Measurement of junction lengths showed that contractomere movement can result in either shortening or lengthening of a junction (Fig. 4 B). Junction shortening occurs when two contractomeres move toward each other whereas junction lengthening occurs when two contractomeres move away from each other (Fig. 4 C). These findings indicate that the lengths of individual junctions, the overall shape of the cell, and the packing geometry of the epithelium could be adjusted quickly by sliding contractomeres around the apical cell boundary in a confluent monolayer of cells. If this hypothesis is true, the junctional lengths of a given individual cell would stay constant. We assessed our hypothesis by culturing a confluent monolayer of MDCK cells on collagen I substrate to promote intercellular movement. Under this condition, MDCK cells would exchange neighbors while maintaining constant cell perimeters (Fig. 4 D). This result supports our hypothesis that contractomere motility can adjust junction proportion and plays a role in the regulation of cell geometry in a confluent epithelial monolayer.

Contractomere motility in mature monolayer

Upon epithelial maturation, the gross movement of contractomeres subsides. However, at a faster movie acquisition rate, contractomeres continue to oscillate at a smaller length-scale and a faster timescale (Videos 18, 19, and 20). This is consistent with the motor property of myosin IIB, which has the ability to step forward and backward, allowing myosin IIB to oscillate on actin filaments (Norstrom et al., 2010). These observations are consistent with a previous study showing that junction oscillation can be blocked by blebbistatin and therefore are due to myosin II activities rather than thermo-fluctuations (Kannan and Tang, 2015). Besides oscillating back-and-forth at smaller length-scales, junctional lengths and inter-contractomeric distances remain unchanged over long periods of time regardless of individual junctional lengths. Structured-illumination live-imaging showed that apical junctions have curved or wavy contours, suggesting a lack of membrane line tension (Fig. S7 and Videos 21, 22, 23, and 24).

Contractomere motility during cell extrusion

The epithelial monolayer is continuously renewed during homeostasis by balancing cell proliferation and cell death. Removal of unwanted or dying cells is carried out in part by constriction of the apical junction in a process called cell extrusion (Kuipers
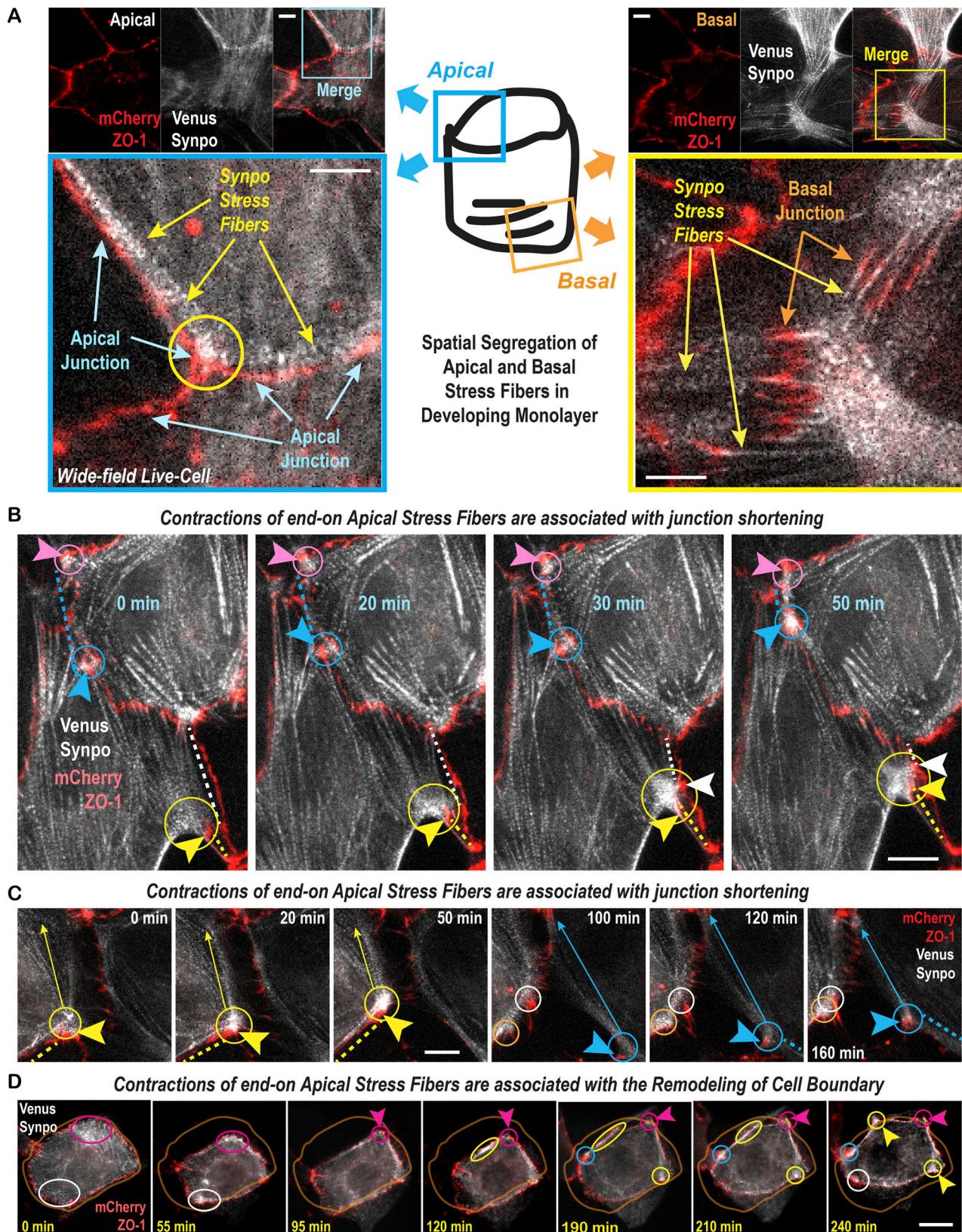
Figure 2. **Synaptopodin apical stress fibers are contractile structures distinct from basal stress fibers. (A)** Frames taken from a time-lapse of synaptopodin and ZO-1 showing apical and basal stress fibers on different focal planes. Apical and basal stress fibers are inserted at apical and basal ZO-1 junctions, respectively. Scale bars are 2 μm. **(B)** Frames taken from a time-lapse of synaptopodin and ZO-1. Arrowheads point to sites of stress fiber attachment at the apical junction. Contraction events are circled. Dotted lines represent lengths of linear junction. Scale bar is 5 μm. **(C)** Frames taken from a time-lapse of synaptopodin and ZO-1. Arrowheads point to sites of stress fiber attachment at the apical junction. Contraction events are circled. Arrows point to direction of movement of the attached junction. Scale bar is 1 μm. **(D)** Frames taken from time-lapse of synaptopodin and ZO-1. Outline of a cell at time zero is drawn in all panels. Arrowheads point to stress fiber attachment sites at the apical junction. Contraction of apical stress fiber is circled. Scale bar is 10 μm.

A *Retrograde synaptopodin flow from the junction templates parallel stress fibers*
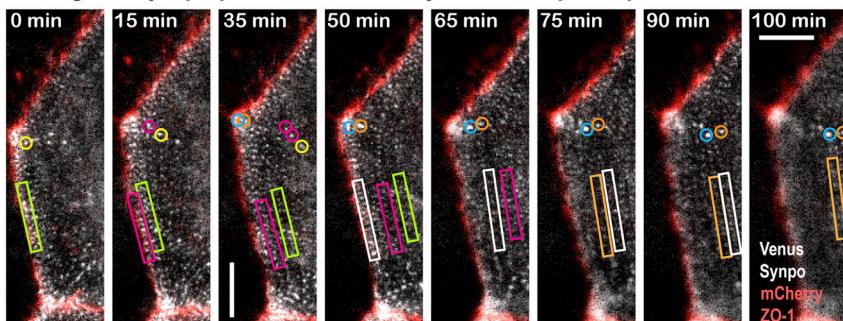
Synaptopodin puncta flow from the apical junction
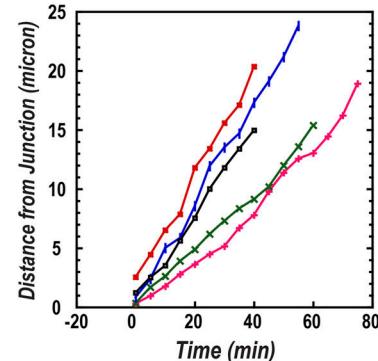
B *Contraction of parallel stress fiber is associated with clustering of junctional complexes*
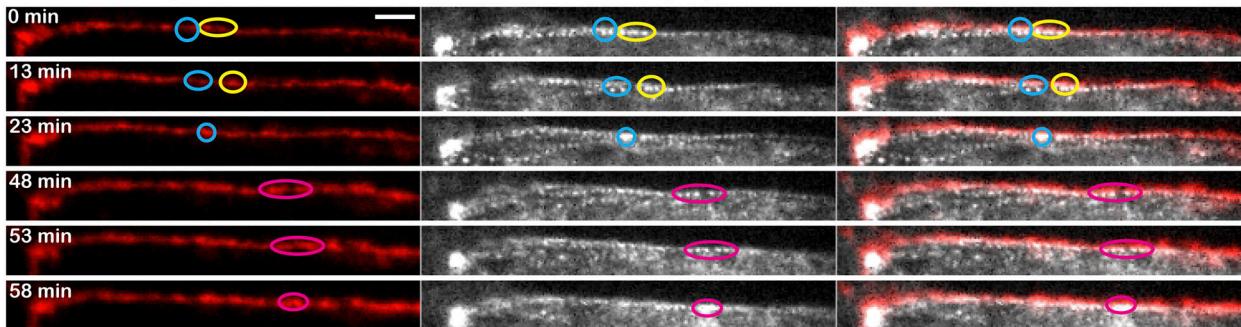
C *Synaptopodin flows along the linear junction towards the contractomere*
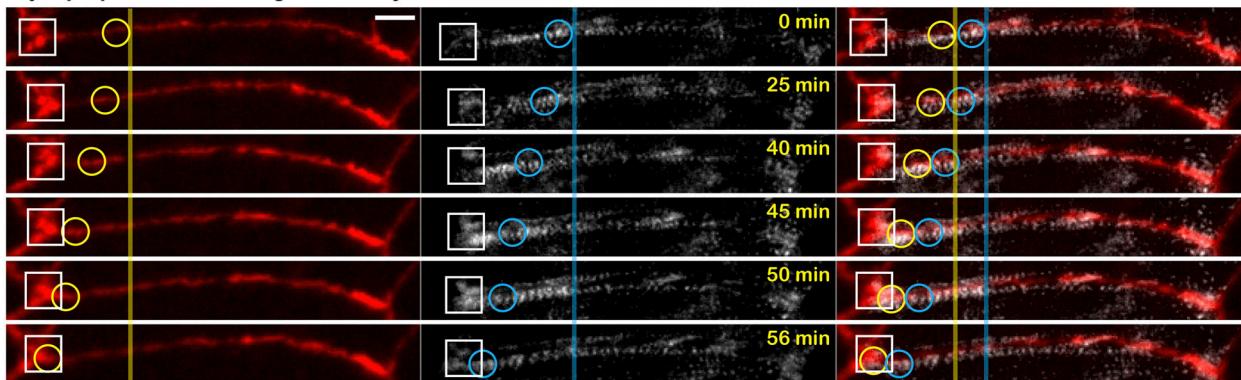
D *Synaptopodin flow towards the contractomere is concomitant with contractomere motility*
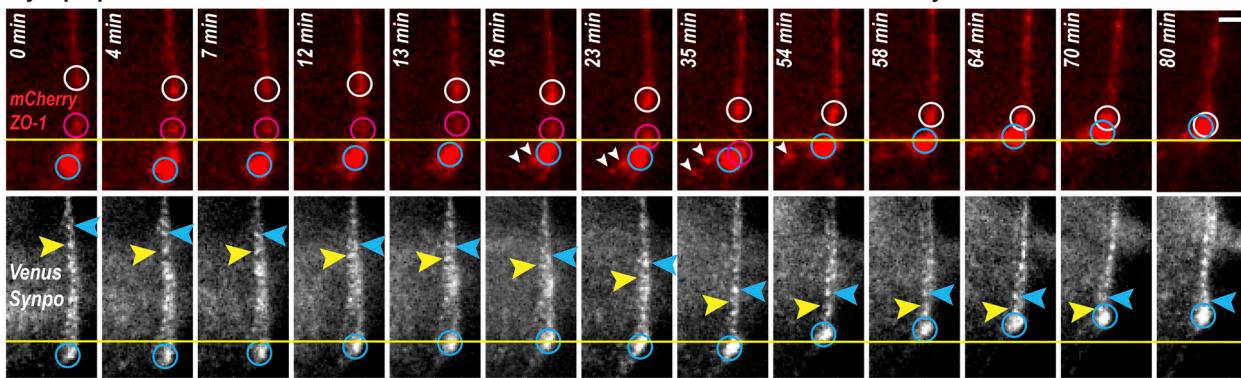
Figure 3. **Synaptopodin retrograde flow and the evolution of apical stress fibers during junction development. (A)** Frames from time-lapse of synaptopodin and ZO-1 in developing junctions. Retrograde synaptopodin flow originates from the apical junction. Rectangles track a row of synaptopodin densities as they flow inwardly away from the apical junction. Circles track single synaptopodin densities flowing from the junction inwardly from the apical junction into the medial-apical region. The graph shows the rate of synaptopodin flow by tracking individual synaptopodin densities. Scale bar is 2 μm.

(B) Frames from time-lapse of synaptopodin and ZO-1 of maturing junctions. ZO-1 densities, marked by arrowheads, are temporarily clustered when synaptopodin stress fibers contract (circled). Scale bar is 1 µm. **(C)** Frames from time-lapse of synaptopodin and ZO-1 at a late stage of junction maturation. Synaptopodin puncta flow toward the junctional vertex. Circles track synaptopodin densities flowing into the junction vertex. Squares mark the vertex. Scale bar is 1 µm. **(D)** Frames from time-lapse of synaptopodin and ZO-1 at a late stage of junction maturation. Synaptopodin puncta flow correlates with the movement of junctional vertex against the direction of synaptopodin flow. Arrowheads track synaptopodin densities flowing into the junction vertex. Blue circles track the movement of the vertex. Red and white circles track ZO-1 densities moving towards the vertex. Scale bar is 500 nm.

et al., 2014; Madara, 1990). We imaged α-actinin to assess if contractomere motility plays a role in cell geometry organization during cell extrusion. When the apical junction constricts, contractomeres surrounding the extruding cell move toward each other (Fig. S8, A and B; and Videos 25 and 26). Tracking the trajectories of individual contractomeres revealed that new cell–cell interfaces are formed between neighbors of the extruding cell (Fig. S8 C, blue and orange arrows and Video 27). At the end of junction constriction, contractomeres became very close to each other and the fluorescence signals were overwhelmed by out-of-focus light from the extruding cell. To visualize contractomeres without the interference by out-of-focus light, we imaged cell extrusion using structured-illumination live-cell microscopy (Fig. S8, D and E; and Videos 28 and 29). By tracking contractomeres during a constriction event, we found that contractomere movements can zip up the apical junction, preserving the continuity of the epithelial cell sheet during the cell extrusion process.

To image the apical junction and synaptopodin simultaneously during cell extrusion, we use occludin, a ZO-1-interacting membrane protein. We found that junctional lengths remain relatively unchanged over a long period of time in mature monolayers (Fig. 4 E). Macroscopically, cell extrusion is not accompanied by gross cell reorganization (Fig. S8 F; and Videos 30 and 31), indicating that it must be achieved through local junction rearrangements.

Live-cell imaging of synaptopodin and occludin shows that contractomeres move during cell extrusion, resulting in the elongation of the apical junction (Fig. 5 A and Video 32). By measuring the distance between a motile and an immobile contractomere, we found that contractomere motility is characterized by persistent "run" periods with intermittent "pause" periods (Fig. 5 A, graph). As we have seen earlier (Figs. 4 E and S8 F), cells in homeostatic monolayer are relatively stationary, and thus could not have contributed to contractomere motility. In homeostatic monolayer, there are two populations of contractomeres during cell extrusion, a mobile pool, and an immobile pool (Fig. 5 B and Videos 33, 34, and 35). While the contractomeres surrounding the extruding cell move to constrict the apical junction (Fig. 5 B, lower left graph), the rest of the contractomeres in the same cells are immobile (Fig. 5 B, lower middle graph). As the apical junction constricts, the perimeter of the extruding cell decreases; this is concomitant with the extension of junctions flanking the constricting contractomeres (Fig. 5 B, lower right graph). Individual contractomeres have slightly different behaviors with unique extension velocities during "run" periods and "pause" periods (Fig. 5 B, graphs). By measuring the perimeter of the extruding cell and the lengths of the extending junctions, we found that

contractomere motility alone could account for the conservation of total junctional length during the first half of cell extrusion (Fig. 5 C). This is especially striking in a mature monolayer when contractomere motility would extend the length of the junction without affecting the lengths of other junctions or the positions of other contractomeres (Fig. 5 D).

These results support our hypothesis that the contractomere is a motorized structure with actin motility function. Our observation is consistent with known motorized organelles that are with associated molecular motors such as myosin, kinesin, or dynein. The behavior of individual motorized organelle is solely dictated by its associated motor rather than the behavior of other motorized organelles in proximity. Thus, junctional contractomeres are likely to behave independently of each other as autonomous motorized structures.

Blebbistatin blocks actin accumulation at the contractomere

The existence of contractomeres underscores a new way to think about junctional processes in epithelial cell sheets. Myosin IIB, a vertebrate paralog of myosin II, has a higher duty ratio and produces greater power than the ancestrally derived myosin IIA (Kovacs et al., 2003; Melli et al., 2018; Stam et al., 2015). Incorporating any myosin II into a junctional complex would confer "motor" function, but incorporating myosin IIB would confer processive actin motility. The goal for the remainder of this study is to determine whether contractomere is a new "organelle" that possesses biochemical activities to "walk the junction."

Previously, we reported that epithelial monolayers treated with latrunculin, an actin monomer sequestration drug that promotes actin monomer dissociation from filament ends (Fujiwara et al., 2018), resulted in the disassembly of filamentous actin, except a latrunculin-resistant pool associated with α-actinin-4 at the apical junction (Tang and Brieher, 2012). We now realize that the α-actinin-4-latrunculin-resistant structures are contractomeres (Fig. 6 A). We postulate that myosin II ATPase activity plays a role in actin accumulation since myosin IIB is enriched at the contractomeres (Figs. 1 D and 6 B). To develop this idea further, we assessed junctional actin using a combination of well-characterized inhibitors of actin dynamics. We found that blebbistatin, a myosin II ATPase inhibitor (Limouze et al., 2004; Ramamurthy et al., 2004), completely prevented the formation of latrunculin-resistant actin (Fig. 6 C), indicating a role of myosin II ATPase actin motility in this process.

How does the contractomere accumulate actin in the presence of latrunculin, which creates an environment that favors depolymerization of actin filaments? One possibility is that the contractomere can polymerize actin using latrunculin-bound actin. To eliminate this highly unlikely possibility, we blocked

Morris et al.
Synaptopodin stress fiber and contractomere at the epithelial junction

Journal of Cell Biology   7 of 32
https://doi.org/10.1083/jcb.202011162
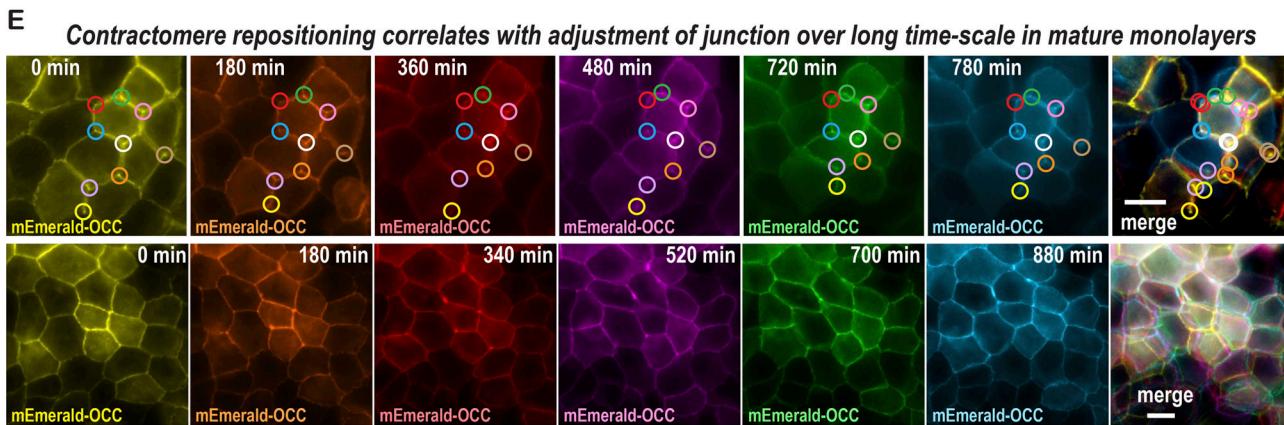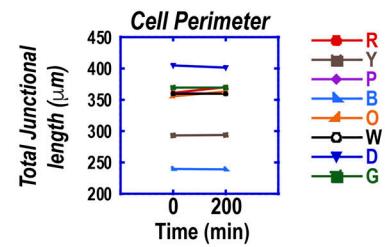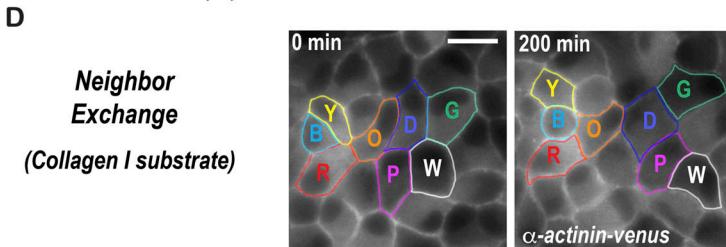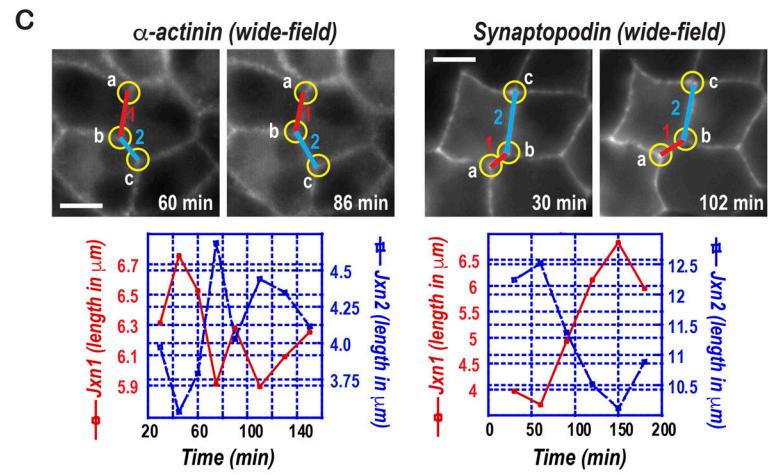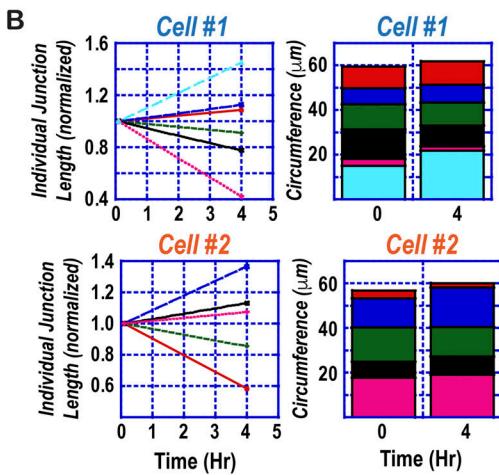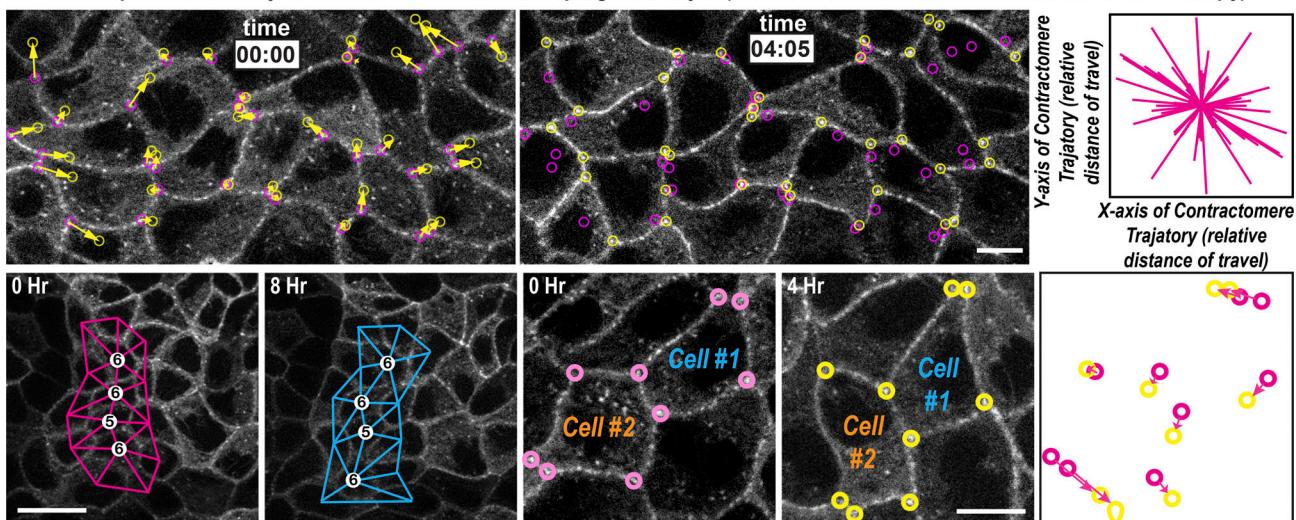
Figure 4. **Contractomere motility conserves junctional length. (A)** Frames from time-lapse structured-illumination of venus-alpha-actinin-1 showing contractomere at the beginning (pink circles) and the end (yellow circles) of a 4-h movie. During intercellular organization, junctional length can shorten when

two contractomeres move toward each other and the junctional length can extend when two contractomeres move away from each other. The distance and direction of travel for the contractomeres are shown in the upper right panel. The lower left two panels show the cells maintaining their neighbors during the 4-h movie. The lower right three panels show contractomere motility in two cells. Scale bars are 10 µm. **(B)** Measurement of junctional lengths of the two cells in A. Cells #1 and #2 are used to illustrate that some junctions increased but the others decreased their lengths, resulting in near zero net change in total junctional lengths. **(C)** Frames from time-lapse wide-field of venus-alpha-actinin-1 and synaptopodin-venus. Gliding of contractomeres to reproportion junctional lengths. In the α-actinin movie, motility of contractomeres resulted in shortening the junction between contractomeres a and b with concomitant lengthening of the junction between contractomeres b and c. In the synaptopodin movie, the motility of contractomeres resulted in lengthening of the junction between a and b with concomitant shortening of the junction between contractomeres b and c. Scale bars are 5 µm. **(D)** Plating of MDCK cells on collagen I at confluent density resulted in intercellular movement and neighbor exchange. The total junctional length of individual cells remained relatively constant. Scale bar is 10 µm. **(E)** Frames from time-lapse of occludin showing contractomere and junctional movement over 12 h. Contractomeres are circled.

actin dynamics using cytochalasin D to prevent filament elongation from the barbed-ends (Fig. 6 D, bottom 2 rows). Strikingly, barbed-end capping by cytochalasin D enhanced actin accumulation at the contractomeres under latrunculin depolymerization environment. One interpretation of this result is that myosin IIB is capable of "walking" on actin filament and "reel-in" the actin filament to form an actin ball at the contractomere. Actin "balls" associated with the apical junction and junction vertices have previously been seen using electron microscopy in cells treated with cytochalasin (Madara et al., 1986; Madara et al., 1988). Actin is a flexible polymer and readily buckles under compressive forces (De La Cruz and Gardel, 2015; Koenderink and Paluch, 2018; Mitchison, 1992; Pollard and Borisy, 2003). The compressive force required for actin filament buckling is comparable with the force exerted by a single myosin II motor (Berro et al., 2007; Murrell and Gardel, 2012). Thus, if our hypothesis is true, blocking myosin II activity should prevent actin accumulation. Indeed, blebbistatin completely abolished latrunculin-induced actin accumulation at the contractomere, either in the presence or absence of cytochalasin D (Fig. 6 D, second, fourth, and sixth rows). These observations support our hypothesis that contractomeric myosin IIB can processively "walk" along actin filaments, conferring actin motility activity to the contractomeric complex.

Actomyosin activity at ZO-1 apical junctions has previously been shown to involve in wound constriction (Tamada et al., 2007). To further explore the relationship between contractomere motility and junction constriction, we repeated the drug experiments on small wounds to determine the impact on wound closure (Fig. 6 E). Treatment of small wounds with latrunculin B resulted in the formation of actin puncta around wound edges (Fig. 6 E, first and third rows). Actin puncta translocate within an hour to constrict the wound (Fig. 6 E, right panels), which is inhibited by blebbistatin (Fig. 6 E, second and fourth rows).

These drug studies raise an important question about the orientation of actin filaments. We have previously shown that Arp2/3 is localized at the contractomere in cells and on purified membranes (Kannan and Tang, 2015). Arp2/3 interacts with actin pointed-end and promotes actin filament elongation from the barbed-end (Bailly et al., 1999; Mullins et al., 1998), which indicate that actin filaments would have barbed-ends facing out from the contractomere. This is consistent with a finding by EM showing actin pointed-ends directed at the apical junction in epithelial cells (Madara, 1987). In cells treated with latrunculin, the degree of actin ball formation would depend on the speed of the myosin IIB motor and actin filament end dynamics. At the apical junction, actin barbed-ends are capped by CD2AP; knockdown of CD2AP prevented latrunculin-resistant actin puncta formation (Tang and Brieher, 2013). Collectively, these observations support our hypothesis that contractomeric myosin IIB acts as a barbed-end-directed motor to "reel-in" actin filaments that have their barbed-ends pointing outward from the contractomere.

Contractomere couples myosin activity and actin polymerization

Contractomere was originally identified in a junction-enriched membrane fraction (Tang and Brieher, 2012). The membrane system is a classic ex vivo preparation that was developed for the identification of adherens, tight, and gap junction components by coupling negative-stain electron microscopy and biochemistry (Anderson et al., 1988; Goodenough and Revel, 1970; Tsukita and Tsukita, 1989). Using a modified protocol of the classic preparation, we had identified a junctional complex containing de novo actin assembly activity (Tang and Brieher, 2012). This activity requires Arp2/3-dependent actin nucleation and α-actinin-4-dependent actin polymerization. Using chemical crosslinking and α-actinin-4 as the bait, we had identified synaptopodin in the complex (Tang and Brieher, 2013). Subsequently, we showed that synaptopodin interacts with myosin II (Kannan and Tang, 2015), implicating a role of myosin II in contractomeric actin assembly in vitro. Here, we performed biochemical analysis to investigate the structure–function relationship between α-actinin-4, myosin IIB, and contractomeric actin assembly using this membrane system, which we had characterized extensively (Kannan and Tang, 2015; Tang and Brieher, 2012; Tang and Brieher, 2013). Briefly, actin assembly is initiated by the addition of 2 µM of fluorescently-labeled monomeric actin, a concentration substantially above the critical concentration of actin, to junction-enriched membranes in the presence of ATP (Figs. 7 A, S9, S10, and S11). Contractomeric actin assembly is enriched at membrane sites marked by bright fluorescent puncta (Fig. 7 A, left panel). Negative-staining EM of the actin assembly reaction revealed filaments coalescing on the contractomere (Figs. 7 A, middle & right panels, S9, S10, and S11). At higher magnification, each contractomere is surrounded by a ball of actin filaments rolled up into a ~300–400 nm structure (Figs. S10 and S11). As we have mentioned earlier, actin filaments are flexible and can be readily buckled by myosin II-generated force (Berro et al., 2007; Murrell and Gardel, 2012). Using optical tweezers, actin filaments can be tied into a knot

Morris et al.
Synaptopodin stress fiber and contractomere at the epithelial junction

Journal of Cell Biology   9 of 32
https://doi.org/10.1083/jcb.202011162

A *Contractomeres move during cell extrusion in maturing monolayer*

Motility of contractomere shows pause between run events

mCherry-OCCLUDIN

0 min 2 min 4 min 6 min 8 min 12 min 14 min 16 min 18 min 20 min

min 0 *

min 8
min 10
min 12
min 16

Venus-Synpo   mCherry-OCCLUDIN

Mobile Contractomeres

Immobile Contractomere

Pause

Run
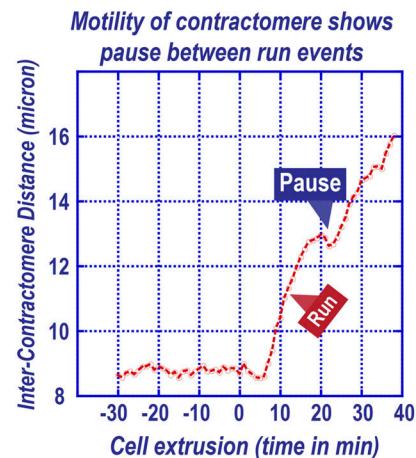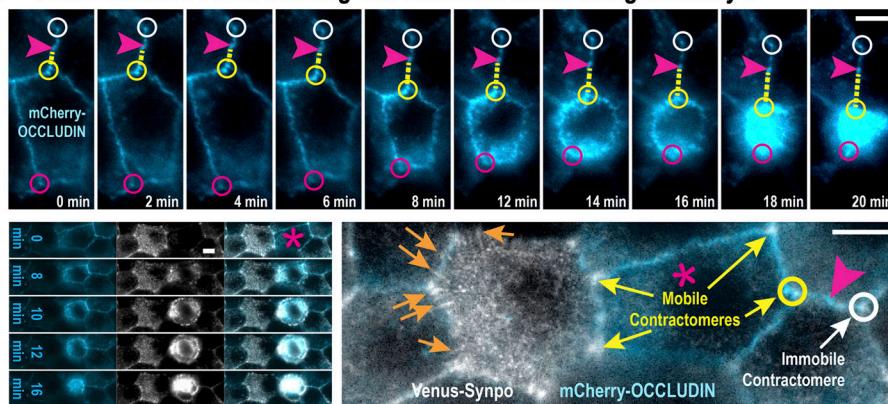
B *Immobile and Mobile contractomeres coexist in the same cells during junction constriction in mature monolayer*

0 min mEmerald-OCC   50 min mEmerald-OCC   90 min mEmerald-OCC   merge

3 Motile Contractomeres in cells next to extrusion

Pause   Run
Run
Run
Pause   Run

3 Immobile Contractomeres in cells next to extrusion

Run
Run

Junction extension during constriction to extrude

Pause
Pause

C *Contractomere motility conserves junctional lengths*

perimeter of extruding cell

0 min   60 min
Time in cell extrusion

D *Conservation of total junctional length via Contractomere Motility*

extending junctions of surrounding cells

0 min mEmerald-OCC   30 min mEmerald-OCC   50 min mEmerald-OCC   merge

Figure 5.   **Mobile and immobile contractomeres coexist in the same cell. (A)** Frames from time-lapse showing contractomere motility during cell extrusion in maturing monolayer. Arrowheads track the location of a stationary ZO-1 density. Graph shows inter-contractomere distance between a motile

Morris et al.
Synaptopodin stress fiber and contractomere at the epithelial junction

Journal of Cell Biology   10 of 32
https://doi.org/10.1083/jcb.202011162

contractomere (yellow circle) and a relatively immobile contractomere (white circle). Pink circle tracks the movement of a second motile contractomere next to the extruding cell (pink asterisk). Scale bar is 5 μm. **(B)** Frames from time-lapse showing gliding of contractomeres surrounding an extruding cell (white asterisk) in a mature homeostatic monolayer. Contractomere-pairs flanking the apical junction between neighboring cells next to the extrusion event are marked by circles and squares of the same color. During cell extrusion, one contractomere of the pair is stationary (circles) while the other contractomere (squares) move away to extend the junction. The merged image shows the absence of global junction movement. The lower left graph shows the distance traveled by the motile contractomeres of the three contractomere pairs, one is immobile and the other is motile. The lower middle graph shows the distance between two immobile contractomeres in the same cells. The lower right graph shows the distance traveled for all seven motile contractomeres surrounding the extruding cell. The perimeter of the extruding cell is plotted to show the decrease in junctional length correlates with elongation of junctions between neighboring cells. Scale bar is 5 μm. **(C)** Graph summarizing total net change in junctional lengths from the lower right graph of B. **(D)** Frames from time-lapse showing gliding of contractomeres around an extruding cell (asterisk) in a mature monolayer. During cell extrusion, contractomeres immediately surrounding the extruding cell (squares) move away from the immobile contractomeres (circles). Merge image shows the absence of global junction movement during cell extrusion. Scale bar is 5 μm.

with a diameter of ∼360 nm (Arai et al., 1999), comparable with the diameter of actin balls associated with contractomeres. Since the "ball" of actin filaments obstructed the features of the contractomere, we dissociated the membrane into smaller fragments by shearing with a 20-μl pipet tip to isolate individual contractomeric membrane fragments. We also lowered the amount of G-actin in the reaction to 0.5 μM (Fig. 7 B), which is slightly above the critical concentration of actin barbed-end, but below the critical concentration of the actin pointed-end (Fujiwara et al., 2007; Pollard, 1986; Zsolnay et al., 2020). These new actin assembly conditions limit the extent of actin filament formation by decreasing the coalescing of actin filaments from multiple contractomeres and selectively permit actin elongation at the barbed-end only. Under these conditions, we observed bright fluorescent puncta associated with small membranous organelles (Fig. 7 B, left panel). Negative-stain EM revealed multiple electron-dense globular masses interacting with single actin filaments (Fig. S12, upper panel). Some of the globular masses are pear-shaped ∼20 nm in dimension (Fig. 7 B, middle panels, and Fig. S12, lower panel), comparable with the distinctive shape and size of the myosin II motor-head (Katayama et al., 2010; Kimori et al., 2013; Nagy et al., 2013; Slayter and Lowey, 1967; Takahashi et al., 1999). At the contractomere, the coiled-coil tail of a myosin-like monomer can be clearly seen extending from the membrane (Fig. S12, lower panel, blue arrows). A myosin-like motor-head of the coiled-coil tail is interacting with an actin filament 100 nm away from the contractomere (Fig. S12, lower panel, red arrows).

One feature of the contractomere under EM is a noticeable lack of the anti-parallel myosin II minifilament (Figs. S9, S10, S11, and S12; and Fig. 7, A and B). A myosin II minifilament is ∼300 nm in length characterized by a dumb-bell shape with myosin heads spraying out at both ends and a bare mid-zone (Billington et al., 2013; Katayama et al., 2010; Liu et al., 2017; Liu et al., 2018; Shutova and Svitkina, 2018). Yet, we were unable to find a structure resembling a myosin II minifilament despite screening 10 different negative stain preparations of native junctional membranes. Purified contractomere is <250 nm in dimension (Fig. S12, upper panel, and 7 B, middle panel), which is too small to hold a myosin II minifilament. In fact, we had demonstrated that the extraction of junctional membranes with non-ionic detergent CHAPS revealed a contractomere core no bigger than 150 nm in dimension but still can interact with actin filaments at multiple sites (Kannan and Tang, 2015).

Recently, monomeric myosin II has emerged as an important player in diverse cellular functions including focal adhesion initiation, cell migration, Golgi dynamics, and exocytosis (Aoki et al., 2010; Ganguly et al., 1992; Kiboku et al., 2013; Shutova et al., 2017; Shutova et al., 2014). Here, we used a modified protocol to assess whether the myosin motor heads and the associated coiled-coil region seen in native membrane could be a monomeric myosin II molecule. By shearing with a 20 μl pipet tip and extraction with 10 mM HEPES at pH 9, we found a subcomplex containing two globular densities with the same distinct pear-shaped heads as seen in native membrane (Fig. 7 B, right panel, blue arrows). The subcomplex contains two myosin-like motorheads interacting simultaneously with a single actin filament (Fig. 7 B, right panel, yellow arrows). The coiled-coil tail of the myosin-like monomer is heavily bound to electron-dense materials (Fig. 7 B, right panel, red arrows). These observations are consistent with recently published works by the Svitkina group showing electron-dense "stuff" bound to the coiled-coil tail of monomeric myosin II inside cells (Shutova et al., 2017; Shutova et al., 2014).

Another striking feature of contractomere under EM is the lack of actin crosslinking. We only found contractomere interacting with single or parallel actin filament rather than a meshwork. Yet, actin assembly requires α-actinin-4, an actin crosslinking protein. Why wound actin assembly require an actin-crosslinking protein? Why do we not see actin networks at the contractomere? One possibility is that α-actinin-4 does not function as an actin crosslinker at the contractomere. To determine if crosslinking is necessary for contractomeric actin assembly, we performed a reconstitution assay by stripping the membranes with high salt to remove endogenous α-actinin-4 and replacing the reaction with recombinant α-actinin-4, an assay we had previously developed for the identification of α-acitnin-4 and synaptopodin (Tang and Brieher, 2012; Tang and Brieher, 2013). Using the reconstitution assay, we tested different truncations of α-actinin-4 to determine whether actin crosslinking is necessary for actin assembly.

α-actinin exists as an anti-parallel dimer ∼36 nm in length (Meyer and Aebi, 1990) containing two actin-binding calponin-homology domains flanked by four spectrin-repeats that support high-affinity anti-parallel dimer formation (Liu et al., 2004). We generated a recombinant α-actinin-4 that has one actin-binding domain (ABD) instead of two actin-binding domains, which thus cannot crosslink actin filaments into networks. For comparison,
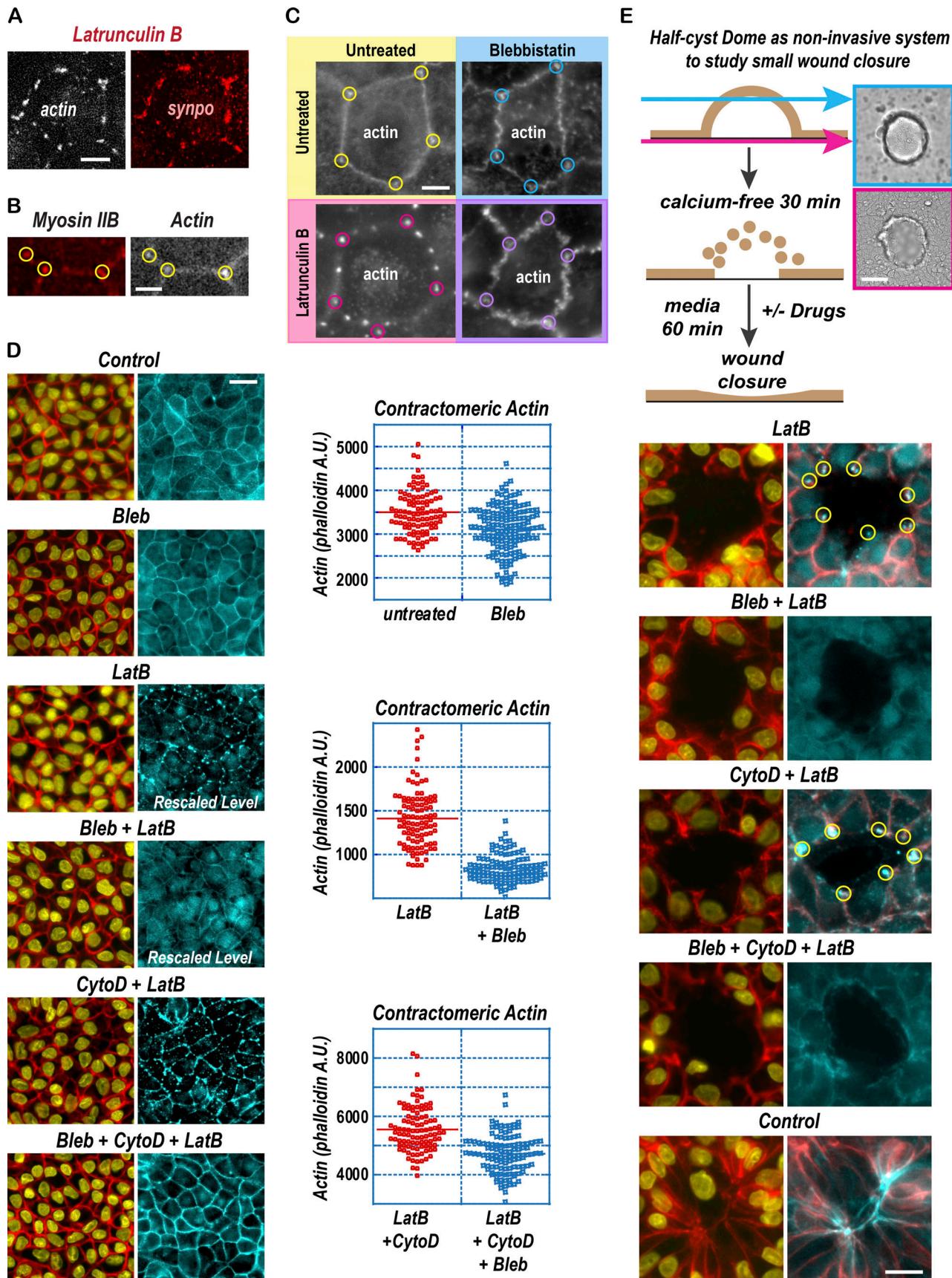
Figure 6. **Contractomeric myosin II activity is linked to actin accumulation. (A)** Immunofluorescence showing synaptopodin (synpo) colocalization with latrunculin-resistant actin puncta at the apical junction. Scale bar is 2 µm. **(B)** Immunofluorescence showing myosin IIB colocalization with actin puncta. Scale

Morris et al.
Synaptopodin stress fiber and contractomere at the epithelial junction

Journal of Cell Biology 12 of 32
https://doi.org/10.1083/jcb.202011162

bar is 1 µm. **(C)** Myosin II inhibition by blebbistatin prevents the formation of latrunculin-resistant actin at the apical junction. Scale bar is 2 µm. **(D)** Myosin II inhibition by blebbistatin (Bleb) prevents the formation of latrunculin (LatB)-resistant actin either in the presence or absence of cytochalasin D (CytoD). Graphs show intensity measurements of actin on individual contractomeres. Bars mark the means. N (untreated) = 101, n (Bleb) = 146, n (LatB) = 101, n (LatB + Bleb) = 109, n (LatB + CytoD) = 100, n (LatB + CytoD + Belb) = 114. Wilcoxon–Mann–Whitney test P < 0.0001 between untreated and blebbistatin treated groups for all three graphs. Scale bar is 10 µm. **(E)** Non-invasion wound healing assay showing the formation of latrunculin-resistant actin surrounding the wound edge (circled). Latrunculin-resistant actin puncta are formed after 1-h incubation with cytochalasin D (CytoD) and latrunculin B (Lat B), but are absent when myosin II was inhibited by blebbistatin (Bleb). In untreated cells, control wound is closed in an hour. Upper right panels show phase-contrast images of MDCK dome before wounding. Scale bars are 10 µm.

we generated α-actinin-4 that has no actin-binding domain or missing the spectrin repeats (Fig. 7 C). After we obtained recombinant α-actinin-4 proteins, we labeled them with a fluorophore so that we can track their targeting to the contractomere (Fig. 7 D). We found that targeting of α-actinin-4 to the contractomere does not require actin-binding; α-actinin-4 missing both actin-binding domains can still localize to the contractomere (Fig. 7 D). This is in sharp contrast to other actomyosin structures such as stress fiber or actin meshwork where binding to actin filaments is necessary for their assembly. Moreover, α-actinin-4 with only one actin-binding domain would support contractomeric actin assembly to the same extent as α-actinin-4 with two actin-binding domains (Fig. 7 E). By contrast, spectrin repeats or actin-binding domain alone was unable to support actin assembly, indicating that both targeting and actin-binding are necessary for α-actinin-dependent actin assembly (Fig. 7, D and E). These results demonstrated that contractomeres exhibit novel and unique biochemistry distinct from other known α-actinin structures.

We have discussed earlier the possibility that actin filament barbed-end needs to face away from the contractomere for barbed-end-directed myosin IIB motor to "reel-in" actin (Fig. 6, D and E). To test whether actin barbed-end is facing away, we used a two-color "pulse-chase" assay to determine the location of actin addition (Fig. 7 F). If actin adds next to the contractomere, the barbed end is likely to localize on the contractomere. However, if actin adds to the outside of polymerizing actin, the barbed-end is likely to face outward. We initiated the actin assembly reaction on contractomeres using a low concentration of FITC-labeled G-actin (0.5 µM) to limit actin elongation to barbed-ends only. After removing unincorporated FITC-labeled G-actin, we continue the reaction using TRITC-labeled G-actin at 0.5 µM (Fig. 7 D, upper cartoon). We imaged the reaction using wide-field microcopy and found that TRITC-labeled actin was incorporated on the outside of FITC-labeled filaments, consistent with our hypothesis that actin monomers are added to barbed-ends facing away from the contractomere (Fig. 7 D, lower panels). Both Arp2/3 and myosin IIB are localized to the sites of actin assembly at the contractomere (Fig. 7 G, lower panels). Both myosin IIB and synaptopodin colocalize with α-actinin-4, the essential factor for contractomeric actin assembly (Fig. 7 G, upper panels). Importantly, actin accumulation at the contractomere requires myosin II activities, which was blocked by blebbistatin (Fig. 7 H).

Calponin homology domains are side-binding domains, thus α-actinin-4 is likely to hold onto the side of an actin filament close to Arp2/3 and the pointed-end at the contractomere (Fig. 7

I). In this configuration, contractomeric myosin IIB can walk toward the barbed-ends, pulling actin filaments toward the contractomere. Based on our hypothesis, barbed-end-directed motor function of myosin IIB would shove actin filaments into the contractomere. We predict that shoving actin filaments toward α-actinin-4, which is located closer to the pointed-end of the filaments, would exert force on α-actinin-4 within the contractomere (Fig. 7 I). To test this hypothesis, we have designed a new FRET-based α-actinin-4 sensor to measure forces at the contractomere.

Alpha-actinin-4 experiences force at the contractomere
We had previously used a FRET-based force sensor, sstFRET, to measure E-cadherin and myosin-1c tension in epithelial cell sheets, indicating that the sensor is capable of registering cellular forces (Kannan and Tang, 2018). The sensor contains a single spectrin repeat consisting of three α-helices that can be unfolded under force (Law et al., 2003). The spectrin-repeat tension-sensing module is flanked by a venus(VFP)-cerulean(CFP) FRET-pair, which has been calibrated to report on ~6 pN of force with a 50% change in FRET (Meng and Sachs, 2011). We inserted the sstFRET cassette away from the actin-binding regions of α-actinin-4 to avoid interfering with actin binding, but at a position where we think might report on changes in force when α-actinin-4 is bound to actin filaments (Fig. 8 A). The spectrin-repeats of α-actinin can interact with many junctional proteins including α-catenin, vinculin, synaptopodin, and ArgBP2 (Asanuma et al., 2005; Bois et al., 2005; Chen et al., 2006; Knudsen et al., 1995). To avoid interfering with these interactions, we positioned the sstFRET cassette within a flexible linker region between the second and third spectrin repeats behind residue 522 (α-actinin-4-sstFRET522) such that the anti-parallel interactions and the dimer interfaces formed by the spectrin-repeats are preserved (Fig. 8 B). Using recombinant α-actinin-4-sstFRET522 expressed in bacteria, we showed that the α-actinin-4-sstFRET522 homodimer is capable of crosslinking actin filaments (Fig. 8 B, lower panels). To confirm that α-actinin-4-sstFRET522 is capable of targeting contractomere and supporting actin assembly, we performed the membrane reconstitution actin assembly assay (Fig. S13 A, left panel). We replaced endogenous α-actinin-4 with α-actinin-4-sstFRET522 by stripping the membrane with high salt, followed by purification of the membrane and binding of α-actinin-4-sstFRET522 to the stripped membrane (see Methods). Actin assembly assay was initiated by the addition of monomeric actin and ATP. Our results showed that α-actinin-4-sstFRET522 accumulates at contractomeres and support contractomeric actin assembly (Fig. S13 A, right panels).
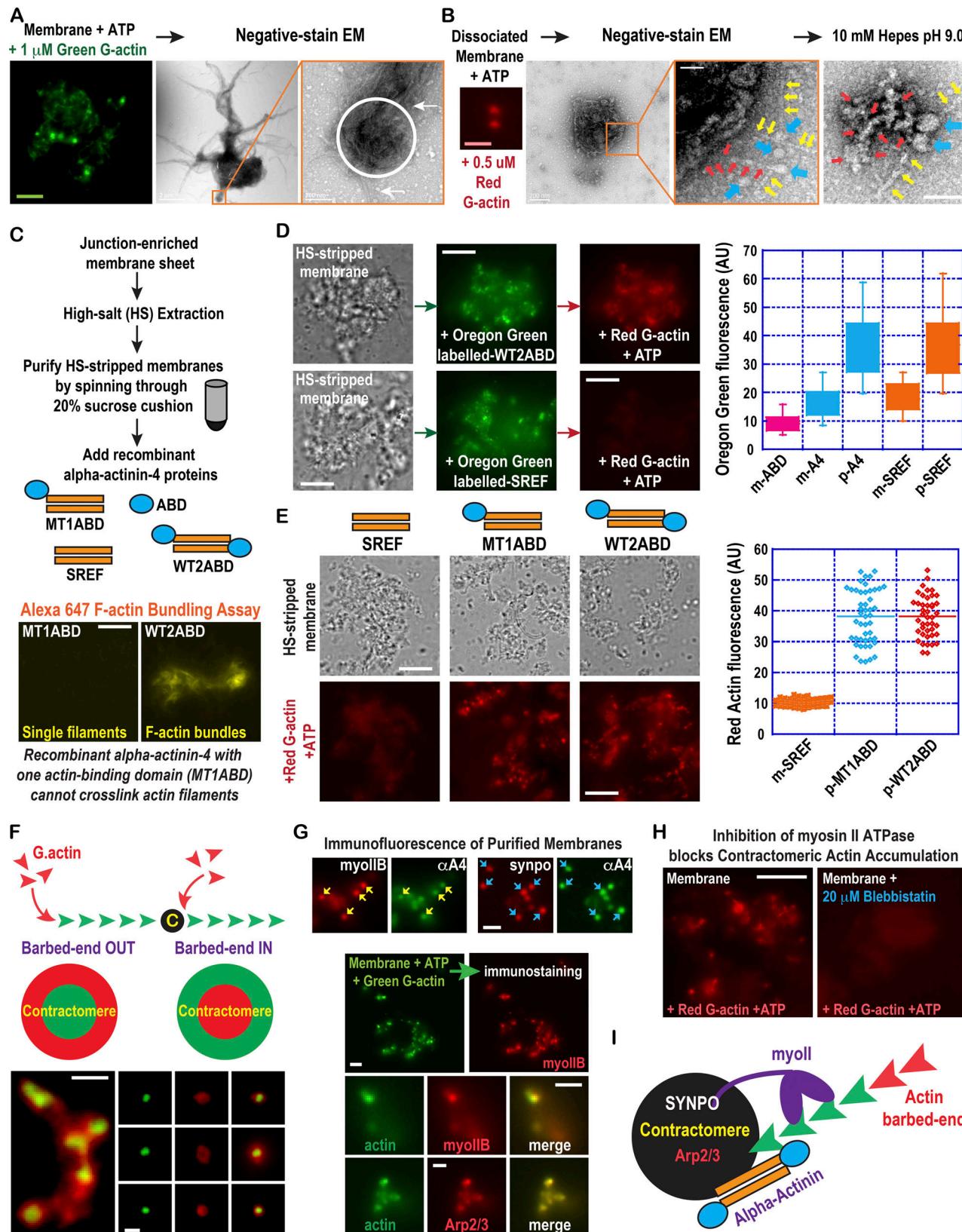
Figure 7. Contractomeric proteins interact with actin filaments. (A) Negative-stain electron microscopy showing actin filaments buckling at the contractomere to generate an actin "ball" (also see Figs. S10 and S11). Left panel shows bright green actin puncta assembled on contractomeres (see Methods). Middle and right panels show actin filaments (arrows) being rolled into a "ball" (circled). Scale bars on two left panels are 2 μm. Scale bar on the right panel is 200 nm. **(B)** Negative-stain electron microscopy shows the interaction of actin filament with contractomere via multiple densities (also see Fig. S12) including a myosin-like linker extending from the membrane (red arrows, left two panels, see Materials and methods). The right panel shows an actin filament (yellow

arrows) interacting with two motor heads of a myosin-like monomer (blue arrows). The tail region of a myosin-like monomer is interacting with electron-dense materials (red arrows, right panel), analogous to "stuff" associated with the tails of myosin II monomers in cells (see Results & Discussion). Scale bar on the left panel is 200 nm. Scale bar on middle and right panels are 20 nm. **(C)** Reconstitution actin assembly assay using stripped membranes and recombinant full-length or truncated α-actinin-4 proteins. Bottom panels show α-actinin-4 that has only one actin-binding domain cannot crosslink Alexa 647-labelled actin filaments into bundles. Scale bar is 2 µm. **(D)** Actin assembly on contractomeres requires α-actinin-4 binding to actin filaments. Reconstitution assay showing α-actinin-4 lacking the actin-binding domains was recruited to contractomeres but failed to support actin assembly. Left panels show membranes using phase contrast microscopy. Middle panels show targeting of α-actinin-4 to contractomeres. Right panels show actin assembly on α-actinin-4-decorated contractomeres. Graph shows intensity measurement of Oregon green-labelled α-actinin-4 on individual contractomeres; boxes represent 75 percentiles and error bars are standard deviations. Membrane-bound signals are m-ABD (n = 94), m-A4 (n = 105), m-SREF (n = 136) and contractomere signals are p-A4 (n = 93) and p-SREF (n = 64). Error bars represent standard errors. Wilcoxon–Mann–Whitney test P < 0.0001 between m-A4 and p-A4 and between m-SREF and p-SREF. P > 0.1 between p-A4 and p-SREF. Scale bars are 2 µm. **(E)** Contractomeric actin assembly only requires one actin-binding domain of α-actinin-4. Upper panels show membranes using phase contrast microscopy. The lower panels show actin assembly on contractomeres pre-bound with α-actinin-4. Actin assembly on contractomeres is equally robust using α-actinin-4 with one or two actin domains. Graph shows intensity measurements of rhodamine-labelled actin on individual contractomeres. Bars mark the means. m-SREF (n = 52), p-MT1ABD (n = 47) and p-MT2ABD (n = 43) refer to contractomeric signals. Wilcoxon-Mann-Whitney test P value < 0.001 between p-MT1ABD and p-SREF. P < 0.0001 between p-MT2ABD and p-SREF. P > 0.1 between p-MT1ABD and p-MT2ABD. Scale bars are 2 µm. **(F)** Pulse-chase actin assembly using 0.5 µM Oregon green-labeled G-actin followed by 0.5 µM rhodamine-labeled G-actin to selectively allow actin monomer addition to actin barbed-ends only (see Results & Methods). Barbed-end elongation of red G-actin shows that actin-barbed ends are most likely to be facing away from the contractomere. Scale bars are 500 nm. **(G)** Localization of myosin IIB, synaptopodin, α-actinin-4, and Arp2/3 at the contractomeres of native purified membranes. Upper panels show immunofluorescence of myosin IIB and synaptopodin colocalize with α-actinin-4 on contractomeres. Scale bar is 1 µm. Lower panels show myosin IIB and Arp2/3 localized to sites of actin assembly on junction membranes. Actin assembly on contractomeres is initiated by adding G-actin to purified membranes in the presence of ATP (see Materials and methods). Immunofluorescence staining for myosin IIB was performed on membranes after an actin assembly assay. Scale bar is 500 nm. **(H)** Actin assembly on purified native membrane is blocked by the addition of blebbistatin to the actin assembly mixture (see Methods). Scale bar is 5 µm. **(I)** Summary of result and working model. Contractomeric α-actinin-4 can hold onto the side of an actin filament with the filament barbed-end facing away from the contractomere. Myosin IIB can walk towards the barbed-end of the actin filament, exerting force and buckling the actin filament.

To determine whether force is exerted on α-actinin-4-sstFRET522 at the junction, we created MDCK cell lines stably expressing α-actinin-4-sstFRET522 (Fig. 8, C–F). We showed that α-actinin-4-sstFRET522 constitutes only a small fraction of total cellular α-actinin-4 using an antibody recognizing both endogenous α-actinin-4 and α-actinin-4-sstFRET522 (Fig. 8 C). Quantitation of Western blot showed that α-actinin-4-sstFRET522 constitute <5% of the total amount of α-actinin-4 expressed in cells (Fig. 8 D, left panels). Immunoprecipitation of α-actinin-4-sstFRET522 using an anti-venus antibody showed an overwhelming bias of α-actinin-4-sstFRET522 dimerizing with α-actinin-4-sstFRET522 over endogenous α-actinin-4; α-actinin-4-sstFRET522 constitutes >94% of α-actinin-4 in the venus immunoprecipitate (Fig. 8 D, left panels). Calculation of α-actinin-4-sstFRET522 heterodimer versus homodimer fractions from the measured levels of α-actinin-4 and α-actinin-4-sstFRET522 yielded a ratio of ~1:162 of heterodimer to homodimer (Fig. 8 D, left panel). By calculating the fraction of unstable heterodimer using the measured values (see Materials and methods), we found that heterodimerization between α-actinin-4-sstFRET522 and endogenous α-actinin-4 is highly unfavorable, representing only ~0.3% of heterodimer if dimerization is a random event. Over 99% of total α-actinin-4-sstFRET522 expressed in cells are in the form of homodimers. Thus, approximately >99% of FRET signals would come from α-actinin-4-sstFRET522 homodimers.

Using a dual-view beam splitter to measure CFP and FRET simultaneously, we compared α-actinin-4-sstFRET522 FRET at the junction and cell protrusions (Fig. 8 E). We found that α-actinin-4-sstFRET522 FRET was substantially higher when measured at the junction than at membrane ruffle, a protrusive structure consisting of dynamic actin meshworks (Fig. 8 E, left panels). In addition to α-actinin-4-sstFRET522, we compared two other sstFRET-based sensors (Fig. 8 E, right panels). The second sensor has sstFRET inserted at the C-terminus

(α-actinin-1-sstFRET-C), and thus cannot experience externally applied force. Measurement of α-actinin-1-sstFRET-C showed a FRET index of ~0.65, representing the background FRET in cytoplasm in the absence of externally applied force. FRET index of ~0.65 is comparable to α-actinin-4-sstFRET522 FRET measured at membrane ruffles, indicating that α-actinin-4 does not experience a measurable force at membrane protrusions (Fig. 8 E, middle panels). The third sensor was originally developed by the Sachs group (Meng and Sachs, 2011; Meng and Sachs, 2012) which has sstFRET inserted within the first spectrin repeat of α-actinin-1 (α-actinin-1-M-sstFRET). However, α-actinin-1-M-sstFRET failed to report a change in FRET between protrusive and contractile structures (Fig. 8 E, right panel), indicating that it is unable to measure force, likely due to the positioning of the force sensor within the rigid spectrin repeat of α-actinin. Thus, only the α-actinin-4-sstFRET522 sensor is capable of measuring cellular force in cells.

To determine whether the contractomere experiences force, we compared α-actinin-4-sstFRET522 FRET at different cellular locations (Fig. 8 F, left and middle panels). We found that α-actinin-4-sstFRET522 FRET was substantially higher when measured at the contractomere than at the junction, suggesting that the contractomere experiences the highest level of compressive force. It is possible that the localization of α-actinin-4-sstFRET522 to the contractomere induces a change in α-actinin-4-sstFRET522 FRET; thus we used actomyosin disrupting drugs to inhibit force generation without displacing α-actinin-4-sstFRET522 from the contractomere to assess whether the compressive force on α-actinin-4-sstFRET522 was due to actomyosin activities or simply contractomere targeting (Fig. 8 F, right panels). When we inhibited myosin II or actin dynamics with myosin light chain inhibitor ML-7, latrunculin B, or cytochalasin D, α-actinin-4-sstFRET522 FRET signal at the contractomere dropped to the background level ~0.65, the same background FRET obtained by the control sensor
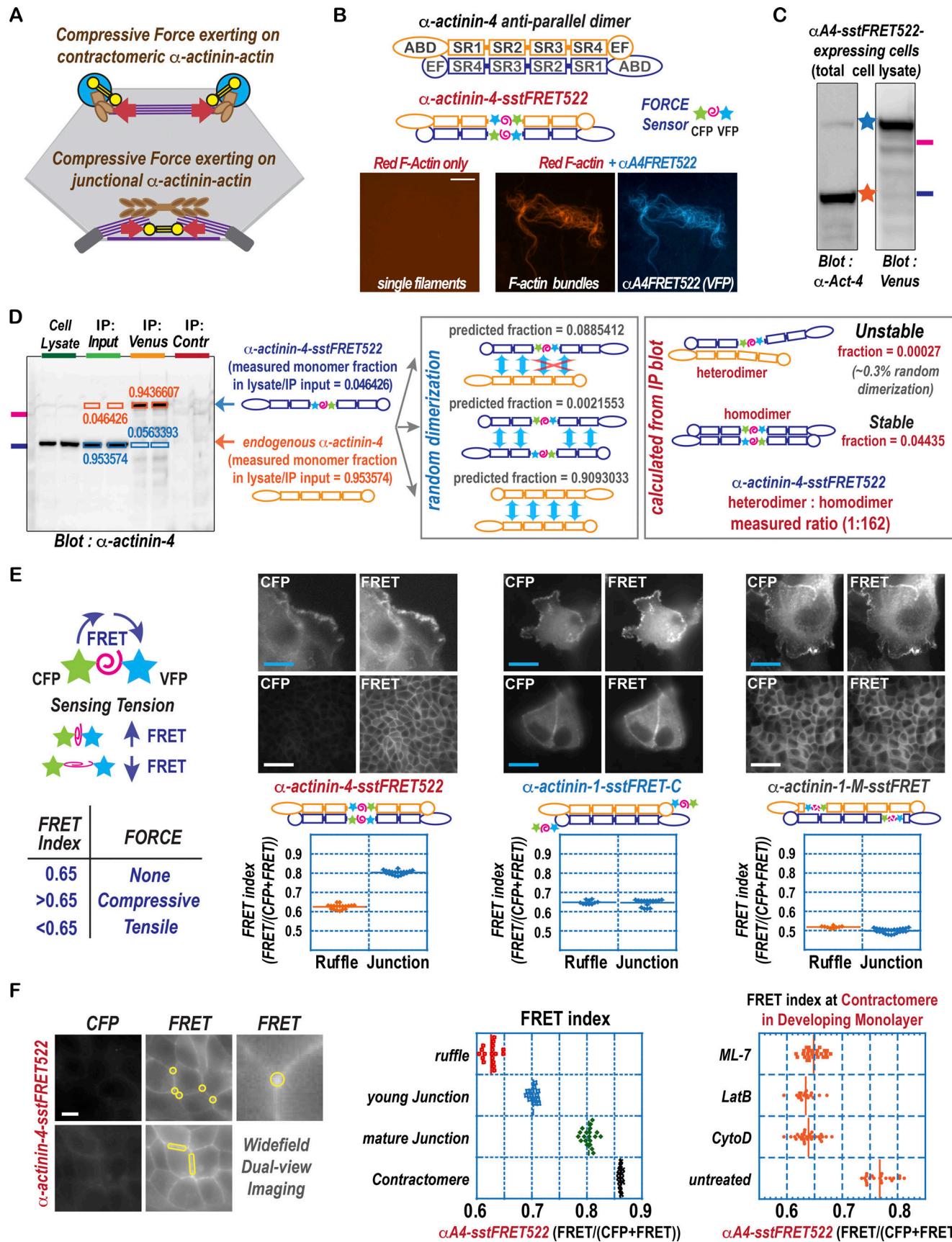
Figure 8. Contractomeric α-actinin-4 experiences actomyosin force. (A) A working hypothesis showing contractomeric α-actinin might experience actomyosin-dependent force. **(B)** Design and expression of an α-actinin-4 FRET force sensor (α-actinin-4-sstFRET522). Recombinant α-actinin-4-sstFRET522 is

able to bundle actin filaments (lower panels, see Methods). **(C)** Expression of α-actinin-4-sstFRET522 in MDCK cells. Left panel is Western blot for α-actinin-4 using an antibody recognizing both the endogenous α-actinin-4 (orange asterisk) and α-actinin-4-sstFRET522 (blue asterisk). Right panel is Western blot for venus recognizing only α-actinin-4-sstFRET522. Markers are 135 kD in pink and 100 kD in purple. **(D)** Homodimer of α-actinin-4-sstFRET522 is the predominant species containing the force sensor. Left panel shows a Western blot of an anti-venus immunoprecipitation (IP) experiment using an antibody recognizing both the endogenous α-actinin-4 (orange arrow) and α-actinin-4-sstFRET522 (blue arrow). Samples were loaded in duplicates. Markers are 135 kD in pink and 100 kD in purple. Quantitation of Western blot band intensities is used to calculate the predicted and actual fractions of α-actinin-4-sstFRET522 homodimers and hetero-dimers (see Materials and methods). Heterodimers are mostly unstable, containing <1% of total α-actinin-4-sstFRET522 expressed in cells. **(E)** FRET readings as proxies for tensile and compressive forces. FRET measurements (see Materials and methods) showing low FRET at protrusions (n = 11) and high FRET, corresponding to compressive force, at the junctions (n = 13) using α-actinin-4-sstFRET522 as the tension sensor. Control sensor with the tension-sensing module inserted at the C-terminal (α-actinin-1-sstFRET-C) is non-responsive to location changes. Control α-actinin-1-sstFRET-C at protrusions (n = 10) and at junction (n = 20) show the same background FRET measurement as α-actinin-4-sstFRET522 (n = 11) at protrusions. Another control sensor with the tension-sensing module within a rigid spectrin α-helix repeat (α-actinin-1-M-sstFRET) is also non-responsive to location changes, with FRET measurement at protrusions (n = 9) the same as at junctions (n = 24). Wilcoxon-Mann-Whitney test P < 0.0001 between ruffle and junction measurements. Scale bars are 5 μm. **(F)** FRET measurements (see Methods) showing α-actinin-4-sstFRET522 background FRET (same α-actinin-1-sstFRET-C FRET) at protrusions and higher FRET at the junctions and contractomeres (middle graph). Left panels show the areas used for contractomere and junction measurements are circled in yellow. N (young junction) = 13, n (ruffle) = 18, n (mature junction) = 20, n (contractomere) = 16. Scale bar is 10 μm. Right graph shows that inhibition of actomyosin dynamics reduces α-actinin-4-sstFRET522 FRET at the contractomere to background FRET level (same α-actinin-1-sstFRET-C FRET). N (untreated) = 22, n (ML-7) = 26, n (LatB) = 19, n (CytoD) = 30. Wilcoxon-Mann-Whitney test P < 0.0001 between untreated and drug treated groups.

α-actinin-1-sstFRET-C (Fig. 8 F, right panels). Despite α-actinin-4-sstFRET522 still being localized to the contractomere, it is not under compressive force in the absence of actomyosin activities. Thus, targeting it to the contractomere is not sufficient to induce FRET changes in the α-actinin-4-sstFRET522 force sensor. Measurement of FRET by co-expressing α-actinin-4-CFP and α-actinin-4-venus with CFP or venus inserted between aa522 and aa 523 of α-actinin-4, also did not register any difference between cytoplasm, junction, and contractomere (Fig. S13, B and C). These observations indicate that actomyosin II activities at the contractomere can generate compressive force, which is measurable by our new α-actinin-4-sstFRET522 force sensor. These observations are consistent with our observation of contractomeric actin "balls" (Figs. 7 A, S9, S10, S11, and S12), supporting our hypothesis that the generation of compression force by actomyosin II at the contractomere buckles actin filaments and rolls the filaments into a "ball".

Knockdown of synaptopodin abolishes stress fibers and contractomeres

We have identified stress fiber and contractomere as synaptopodin structures at the apical junction. To assess whether these structures require synaptopodin for assembly, we knocked down synaptopodin in MDCK cells. In the developing monolayer, stress fibers were absent in synaptopodin knockdown cells (Fig. 9 A). Moreover, synaptopodin knockdown selectively reduced myosin IIB and myosin light chain levels without affecting junctional components including α-catenin, β-catenin, p120-catenin, vinculin, and α-actinin-4, and myosin IIA (Fig. 9, B and D). Despite overall co-localization of myosin IIA and IIB in stress fibers and the contractomeres (Fig. S14 A), synaptopodin knockdown selectively downregulates myosin IIB, but not myosin IIA (Fig. 9, B and E). In mature monolayers, contractomeres were missing in synaptopodin knockdown cells and α-actinin-4 became cytoplasmic (Fig. 9 F). In contrast, myosin IIA and actin levels at the junctional cortex were not appreciably affected (Fig. 9 G). Strikingly, stress fibers on the basal cell surface are now converted into a meshwork-type actomyosin IIA organization (Fig. 9 H).

Synaptopodin is essential for the maintenance of permeability barrier in multiple systems including MDCK cells, T84 intestinal cells, mouse intestine, and kidney podocytes (Kannan and Tang, 2015; Ning et al., 2020; Ning et al., 2021; Wang et al., 2020). However, the mechanism for its protective function is not known. Now we know that synaptopodin depleted cells are missing stress fibers and contractomeres. Synaptopodin depletion decreases the rate of wound migration in endothelial cells, epithelial cells, and podocytes (Anekal et al., 2015; Ning et al., 2020; Ning et al., 2021; Rochman et al., 2017), which is consistent with the role of stress fibers in lamella formation in migrating cells (Burridge and Guilluy, 2016). Several studies have also shown that epithelial integrity is disrupted to a greater extent in synaptopodin depleted cells when challenged by chemical insult, indicating a protective role and a survival advantage provided by synaptopodin. These advantages could be due to the ability of contractomeres to quickly close wounds and preserve the epithelial permeability barrier during cell extrusion.

Synaptopodin knockout mice resulted in the downregulation of RhoA in adult animals (Asanuma et al., 2006; Ning et al., 2020). RhoA is a regulator of stress fiber assembly and contractility (Ridley and Hall, 1992), and could potentially have a role in synaptopodin function. However, in MDCK cells, synaptopodin knockdown did not affect the level or activity of RhoA despite the drastic decrease in phospho-myosin light chain levels in synaptopodin knockdown cells (Fig. S14, C and D), indicating that synaptopodin is likely to use an alternative pathway to control actomyosin structures and contractility in MDCK cells. Sequence analysis of synaptopodin indicates that it contains several putative binding sites for ArgBP2/SORB2 (Scansite, MIT), a vertebrate paralog of the conserved SORBS1/ponsin (Ichikawa et al., 2017). ArgBP2/SORB2 accumulates at the apical junction and targets stress fibers in an α-actinin-dependent fashion and binds directly to α-actinin-4 (Anekal et al., 2015; Fredriksson-Lidman et al., 2017). ArgBP2 also interacts with WAVE2 (Cestra et al., 2005), which regulates actin dynamics at the epithelial junction in an Arp2/3-dependent manner (Nakanishi et al., 2007; Verma et al., 2012). Moreover, ArgBP2/SORB2 binds to Arg (Abl-related gene), which preferentially
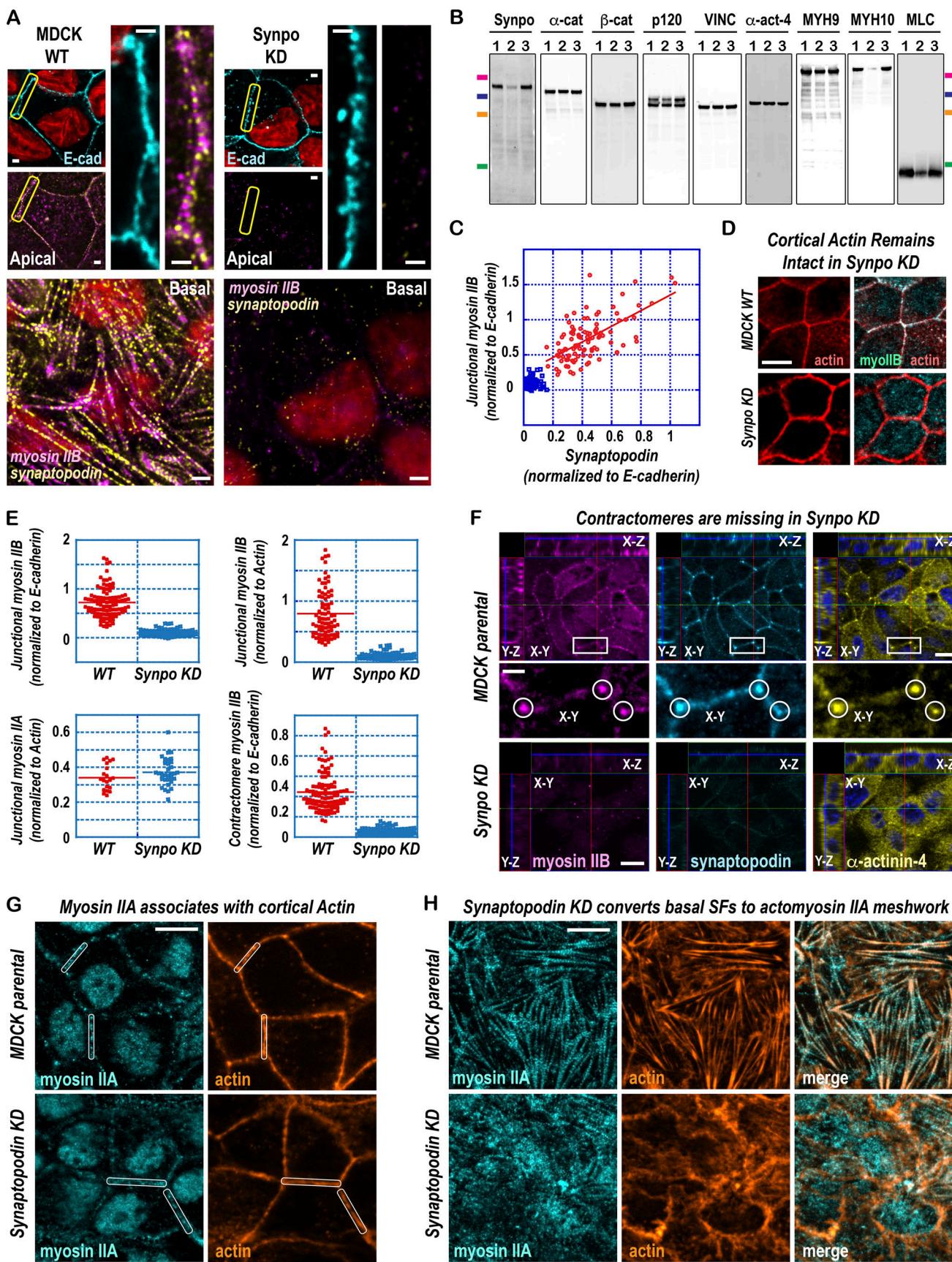
Figure 9. **Contractomeres and stress fibers are missing in synaptopodin knockdown cells. (A)** Immunofluorescence of MDCK wild type (WT) and synaptopodin knockdown (Synpo KD) cells. Apical and basal stress fibers are missing in synaptopodin knockdown cells. Scale bars are 1 μm. **(B)** Western blots

Morris et al.
Synaptopodin stress fiber and contractomere at the epithelial junction

Journal of Cell Biology 18 of 32
https://doi.org/10.1083/jcb.202011162

showing reduced cellular levels of myosin IIB and myosin light chain in synaptopodin knockdown cells. Lanes 1 and 3 are whole cell lysate of MDCK parental cells. Lane two is whole cell lysate of synaptopodin knockdown cells. Markers are 150, 100, 75, 25 kD. **(C)** Scatter plot showing the relationship between synaptopodin and myosin IIB levels in WT (red dots n = 102) and Synpo KD (blue squares n = 119) at the apical junction. Pearson correlation coefficient R is 0.63 between synaptopodin and myosin IIB at WT junction. **(D)** Myosin IIB is absent from the apical junction in synaptopodin knockdown cells despite the presence of junctional actin. Scale bar is 5 µm. **(E)** Synaptopodin knockdown (Synpo KD) reduced myosin IIB but not myosin IIA levels at the junction. Measurement of junctional and contractomeric intensities of myosin IIA and IIB immunofluorescence. For upper left and right graph, n (WT) = 102, n (SynpoKD) = 119. For lower left graph, n (WT) = 20, n (SynpoKD) = 32. For lower right graph, n (WT) = 106, n (SynpoKD) = 114. Wilcoxon-Mann-Whitney test P < 0.0001 between WT and Synpo KD for myosin IIB. Wilcoxon-Mann-Whitney test P > 0.1 between WT and Synpo KD for myosin IIA. **(F)** Contractomeres are missing from junctional vertices (circled) in synaptopodin knockdown cells. Z-stacks are shown in X-Y, Y-Z, and X-Y axes. In synaptopodin knockdown cells, myosin IIB level was lower and α-actinin-4 became cytoplasmic. Scale bars are 5 µm. **(G)** Myosin IIA and actin remain present at the apical junction in synaptopodin knockdown monolayers. Scale bar is 5 µm. **(H)** Basal myosin IIA stress fibers are converted into myosin IIA meshworks in synaptopodin knockdown cells. Scale bar is 5 µm.

phosphorylates myosin IIB over myosin IIA (Boyle and Koleske, 2007). In this study, we showed that synaptopodin depletion significantly reduced the level of ArgBP2/SORB2 (Fig. S14 D), implicating the synaptopodin/ArgBP2/MIIB pathway in actomyosin regulation in a RhoA-independent manner.

Collectively, our results underscore the roles of vertebrate-specific synaptopodin not only in the assembly of vertebrate-specific stress fibers and contractomeres, but also in the regulation of vertebrate-specific ArgBP2/SORBS2/MIIB mechanotransduction.

Discussion

In this study, we have described two novel synaptopodin-dependent actomyosin structures at the apical junction: stress fiber and contractomere (Fig. 10). The first structure, apical stress fiber, consists of alternating and periodic arrangements of myosin II, synaptopodin, and α-actinin. Unlike basal stress fibers that are inserted at vinculin-enriched cell–cell adhesions, apical stress fibers are inserted at E-cadherin and ZO-1-decorated apical junction. When an apical stress fiber is attached head-on at the junction, orthogonal pulling force can be exerted on the membrane junctional complex. By contrast, if an apical stress fiber is attached side-on to the junction, parallel force would be exerted along the linear length of the junction. Contraction of parallel stress fiber is associated with clustering and lateral movement of junctional complexes, whereas the contraction of orthogonal stress fiber shortens the junction. The second structure, contractomere, is a novel macromolecular assembly ~150–200 nm in dimension containing myosin II, synaptopodin, and α-actinin. We named this structure "contractomere" for its biochemical and structural properties; "contracto" refers to the fact that it uses myosin II motor activity for actin motility function and "mere" refers to it being a minimal macromolecular complex to support its functions. We demonstrated that contractomere uses a novel mechanism by harnessing the energy from actin and myosin ATPases to power its movement and support junction organization.

Contractomere exists as a standalone structure and can be isolated from tissues or cultured epithelial cells in the absence of actin (Tang and Brieher, 2012). This is in contrast to stress fibers or actomyosin networks where the interaction between actin filament and myosin II minifilament is required for their structural integrity and assembly. Contractomere can glide along the junction to zip-up opposing plasma membranes of

neighboring cells, creating a new cell–cell adhesion interface. The motility of contractomeres during cell extrusion allows the apical junction to constrict, while maintaining the integrity of the epithelial barrier.

We propose a model by which myosin II embedded within the contractomere can "walk" on actin filaments and "pull" actin filaments toward the center of the contractomere. Since myosin II is a barbed-end-directed motor, our model requires actin barbed-ends to face away from the contractomere so that the motor can slide actin filaments in the direction of the contractomere. Our finding is opposite of what we would expect from the paradigm of field since myosin II contractility is thought to pull on the junction from a distant location, thus requiring actin barbed-ends to face toward the junction.

To investigate our hypothesis further, we generated a novel α-actinin-4 FRET tension sensor to monitor forces at the contractomere. We showed that contractomeric α-actinin-4 experiences changes in force in an actomyosin-dependent manner. These observations are consistent with myosin II shoving the filaments toward the contractomere and exerting a compressive force on α-actinin-4 located within the contractomere. In agreement with compressive force causing buckling of actin filament (Berro et al., 2007; Murrell and Gardel, 2012), we found contractomeric actin filaments rolled into a "ball" when observed using negative stain EM.

Lastly, we showed that the formation of these two actomyosin structures requires a vertebrate-specific protein called synaptopodin. Depletion of synaptopodin prevented the assembly of apical stress fiber and contractomere. Importantly, synaptopodin depletion resulted in the conversion of stress fiber into a meshwork-type actomyosin II organization. Our results not only revealed that synaptopodin is a regulator of stress fiber assembly but that the type of actomyosin assemblies can be tuned by synaptopodin.

Redefining actomyosin structures of the epithelial junction

The prevailing models of actomyosin structures at the epithelial junction describe three different actomyosin organizations for force generation, and all of them depend on bipolar myosin II minifilaments (Fig. 10, A and B). The first model describes a submembrane cortical actomyosin II network (Fig. 10 A, upper left). The second model describes parallel actin cables bundled by actomyosin II (Fig. 10 A, upper right). The third model describes an isotropic actomyosin II meshwork on the apical cortex
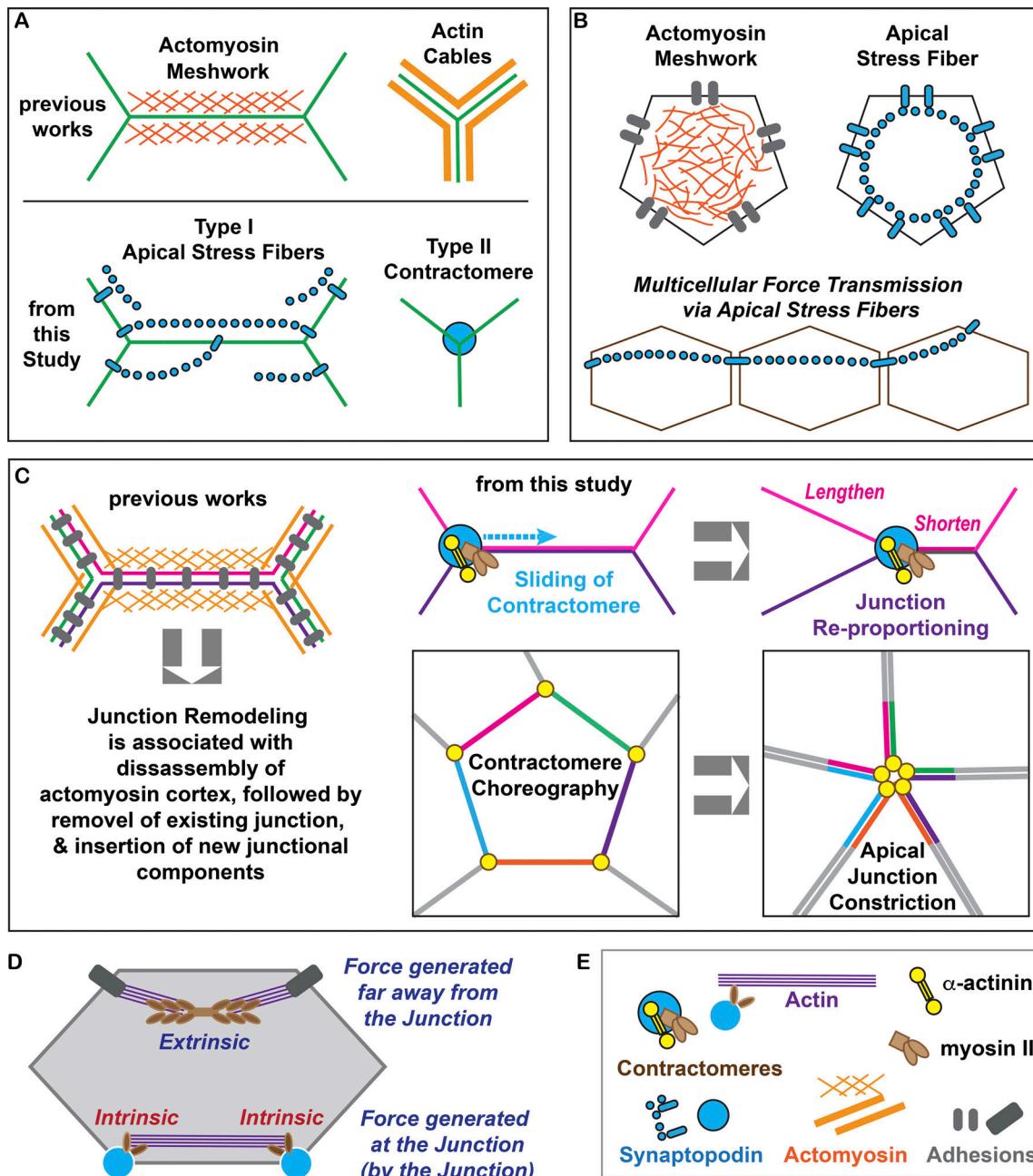
Figure 10. Actomyosin structures at the apical junction. (A) Comparison of actomyosin meshwork and cables with apical stress fiber and contractomere. Apical stress fibers can selectively link neighboring junctions as well as junctions from opposite sides of a cell. Contractomere is a unique actomyosin structure that contains non-filamentous myosin II. **(B)** Comparison between actomyosin meshwork and apical stress fiber is shown at the top panels. Apical stress fibers inserted at cell–cell adhesion can propagate force across many cells in an epithelial monolayer, the bottom panel. **(C)** Shortening and lengthening the junction by "walking" the contractomere. Motility of contractomere contributes to junction constriction during cell extrusion and pure-string wound closure. Prevailing model of junction remodeling requires disassembly of junction actomyosin cortex and endocytosis of existing junction. **(D)** Contractomere generates intrinsic force whereas apical stress fiber or actomyosin meshwork generates extrinsic force with respect to the junction. Contractomere is powered by myosin II and actin polymerization locally at the junction while apical stress fiber is powered by myosin II at a distance away from the junction. **(E)** Key to cartoon.

([Fig. 10 B](#), upper left). All the three structures are likely to exert orthogonal force on the junction. However, they fall short in explaining how the junction can shrink during wound constriction, cell extrusion, or intercellular rearrangements. The two major issues are as follows.

The first issue is the fluid mosaic problem. In the first and second models stated above, force is exerted parallel to the

junction, pulling adhesion complexes on the plane of the membrane. The parallel force would move adhesion complexes on the plane of the plasma membrane, potentially causing them to cluster. This mechanism will leave the lipids of the plasma membrane untouched rather than shrinking the junction. In the third model stated above, contraction of apical isotropic meshwork would pull on the junction

perpendicularly, producing net-zero parallel force, which has no effect on the junctional length.

The second issue is the 300 nm problem. Bipolar myosin II minifilaments are >300 nm long and geometrically cannot close the junction. If each linear junction has only one myosin II minifilament, a cell with five sides will be stuck with a hole >500 nm in diameter at the end of junction constriction. In *Drosophila*, apical constriction is arrested with a hole during wound healing, which must be closed by protrusion and cell migration (Abreu-Blanco et al., 2012; Wood et al., 2002). However, contractomere does not have the 300 nm geometric constrain of the myosin II minifilament and can constrict the junction completely without leaving a hole (Fig. 10 C, lower right panels).

A new concept that emerged from this study is the origin of force. Force production by the contractomere is an intrinsic process since actin assembly and myosin II ATPase occur directly at the junctional complex (Fig. 10 D). By contrast, apical stress fibers or cortical actin meshworks are cytoplasmic structures. The force generated by these structures is extrinsic to the junctional complex and must be relayed via other protein assemblies. The existence of two independent force-production regimes increases the complexity of vertebrate mechanoregulation and the ability of epithelial cells to differentially regulate junction processes.

Regulation of actomyosin structures at the epithelial junction

Apical stress fiber, contractomere, and actomyosin meshwork are three different force-generating structures, contributing to distinct force-dependent processes at the junction. The three regimes allow independent regulations and force transmission pathways that are structurally and functionally segregated. Previous studies have shown that myosin IIA structures are primarily controlled by Rho/Rock/MLC, whereas myosin IIB structures are mainly regulated by Ca^{++}/calmodulin/MLCK (Chang and Kumar, 2015; Kassianidou et al., 2017; Kuragano et al., 2018; Morin et al., 2014; Totsukawa et al., 2004). Phosphorylation studies using purified myosin II indicate that MLCK phosphorylates myosin IIB more efficiently than ROCK, whereas the reverse is true for myosin IIA (Amano et al., 1996; Sandquist et al., 2006). Furthermore, MLCK is >50 times more efficient in phosphorylating MLC than ROCK (Bresnick, 1999). Here, we show that ArgBP2/SORB2 may be another player in regulating actomyosin structures. A future goal is to determine the relative contribution of these pathways in the regulation and assembly of apical stress fiber and contractomere.

Myosin II bipolar minifilament has a characteristic dumbbell structure ~300 nm in length and consisting of a bare midzone and myosin heads spraying out from two ends. In purified junctional membranes, myosin II filamentous structure had not been observed. Instead, we found a compact macromolecular complex ~150–250 nm in dimension (Kannan and Tang, 2015). Dissociation of the contractomeric complex using mechanical and biochemically perturbations showed that the coiled-coil tail of myosin II monomer was bound to proteins. These findings are consistent with previous reports by the Svitkina group

describing the existence of electron-dense material surrounding the coiled-coil region of unfolded monomeric myosin II (Shutova et al., 2017; Shutova et al., 2014). The coiled-coil region has also been shown to play a role in targeting myosin IIB to secretory granules independent of actin (Milberg et al., 2017). These previous observations and our current results add to the growing number of studies showing that myosin IIB localization to different structures does not require binding to actin (Badirou et al., 2014; Beach and Egelhoff, 2009; Fanning et al., 2012; Liu et al., 2016; Rosenberg et al., 2008; Roy et al., 2016). Thus, the interaction between synaptopodin and myosin IIB could potentially recruit myosin IIB and/or myosin IIA to the contractomere. One future goal is to determine whether synaptopodin binds to the coiled-coil region of myosin IIB and/or myosin IIA, and whether the interaction is responsible for myosin II recruitment to the contractomere.

The Svitkina group has demonstrated that myosin II monomers are phosphorylated inside cells (Shutova et al., 2017; Shutova et al., 2014). Myosin II phosphorylation activates myosin II, converting myosin II from an inactive autoinhibited state into a constitutively active motor. Consistent with their observations, the Korn group has shown that recombinant myosin II monomers that are in the unfolded state can be phosphorylated in vitro (Liu et al., 2017; Liu et al., 2016; Liu et al., 2018). Collectively, these studies show that the motor function of unfolded monomers can be controlled by phosphorylation similar to filamentous myosin II. Importantly, phosphorylated unfolded monomeric myosin II is likely to be constitutively active with actin motility activity. Multiple phosphorylation sites have been identified on the coiled-coil region of myosin IIB, and phosphorylation of these sites by PKC-ζ and CK-2 promotes the disassembly of myosin II minifilaments and the formation of myosin II monomers (Dulyaninova and Bresnick, 2013; Even-Faitelson and Ravid, 2006; Juanes-Garcia et al., 2015; Murakami et al., 1998; Murakami et al., 1984; Vicente-Manzanares et al., 2009). PKC-ζ and CK-2 are kinases that regulate the development, stability, and maintenance of the epithelial junction (Dorfel et al., 2013; Eckert et al., 2005; Helfrich et al., 2007; Raleigh et al., 2011). Synaptopodin has previously been shown to co-immunoprecipitate with PKC-ζ in a membrane complex (Tang, 2006). Thus, myosin IIB regulation by PKC-ζ and CK-2 might contribute to junction maturation by converting myosin II filaments into monomers at the apical junction. Our results show that apical stress fiber, which is formed by bipolar myosin II filaments, dissolves during junction maturation with concomitant formation of contractomere. The dissolution of apical stress fiber is specific at the apical junction because the basal stress fiber remains intact, indicating that the apical junction contains regulator(s) for the conversion process. Local regulation at the apical junction would provide an immediate pool of monomeric myosin II for contractomere assembly. This is in contrast to the current paradigm that the primary role of monomeric myosin II is to serve as a reserve pool for myosin II minifilament assembly. A future goal is to determine the mechanism responsible for converting bipolar filaments into contractomeric myosin II at the apical junction.

Materials and methods
Antibodies and reagents

Primary antibodies were purchased from commercial sources and custom-generated. Rabbit and goat polyclonal antibodies to synaptopodin were raised against synthetic peptides corresponding to four regions of human synaptopodin ×1 (NCBI Reference Sequence: XP_016864497.1): aa164-180 (PSSNSRGVQLFNRRRQR), aa675-684 (QQESAPRDRA), aa899-918 (SPRAKQAPRPSFSTRNA-GIE), and aa1123-1143 (CPRGWNGSLRLKRGSLPAEAS). The peptides were synthesized and coupled to KLH before injection into the animals (Pacific immunology). Serum reactivity to the peptides was assessed by ELISA (Pacific immunology). Rabbit polyclonal antibodies to α-actinin-4 were raised in-house against a synthetic peptide corresponding to aa8-24 of human α-actinin-4, NQSYQYGPSSAGNGAGC, which has been coupled to KLH. Antibodies to α-actinin-4 (sc-3933495, mouse), β-catenin (sc-7963, mouse), synaptopodin (sc-515842, mouse; sc-21537, goat), α-catenin (sc-9988, mouse), p120 (sc-13957, rabbit), vinculin (sc-5573, rabbit), myosin IIA (sc-47201, rabbit), myosin IIB (sc-376942, mouse), RhoA (sc-418, mouse), MRIP (sc-135494, goat), ArgBP2 (sc-514671, mouse), Arp2 (sc-10125, goat), and Arp3 (sc-10132, goat and sc-136279, mouse) were purchased from Santa Cruz Biotechnology. Rabbit polyclonal antibodies to myosin IIA (19098) and myosin IIB (19099) were purchased from Biolegend. Antibodies to phospho-myosin light chain 2 (Thr18/Ser19) were purchased from Cell Signaling Technology (#3674, rabbit). Mouse monoclonal antibodies to Venus were purchased from Sigma-Aldrich, EMD-millipore (MAB131890, mouse clone 10 and MABE1906, mouse clone 5). Secondary antibodies were purchased from Bio-Rad Laboratories (HRP goat anti–rabbit), Santa Cruz Biotechnology (HRP rabbit anti-goat and goat- anti-mouse), Life Technologies/Invitrogen Alexa 488 donkey anti-mouse, Alexa 568 donkey anti-rabbit, and Alexa 647 donkey anti-goat. Protease inhibitors used for cell extraction and membrane preparation, leupeptin, Pefabloc, E-64, antipain, aprotinin, bestatin, and calpain inhibitors I and II were purchased from A.G. Scientific, Inc. Rhodamine, rhodamine green, Latrunculin B, cytochalasin D, FITC-phalloidin, TRITC-phalloidin, and blebbistatin were purchased from Sigma. MLCK inhibitor ML-7 (4310) was purchased from Tocris. Alexa 647-phalloidin and Alexa 350-phalloidin were purchased from ThermoFisher/LifeTechnologies. Stock solutions of latrunculin B (5 mM), cytochalasin D (2 mM), blebbistatin (5 mM), ML-7 (10 mM), and phalloidin were prepared in dimethylsulfoxide (Sigma-Aldrich).

DNA constructs

Synaptopodin A was synthesized by Genscript using the coding sequence of human synaptopodin (NCBI Reference Sequence: NP_009217.3) and was subcloned by Genscript into HINDIII and Xho1 sites of the blasticidin-selectable mammalian expression vector pcDNA6 myc-HisA (Invitrogen) containing an N-terminal sstFRET (Meng and Sachs, 2011) and C-terminal myc and His tags. shRNAs for canine synaptopodin (5′-GAGGTGAGATCCAGC ACACTTCTGATTGA-3′) were synthesized and subcloned into puromycin-selectable pRS vectors by OriGene.

sstFRET consists of a single spectrin repeat flanked by cerulean and Venus fluorescent proteins (TCCGTGAGCAAGGGC

GAGGAGCTGTTCACCGGGGTGGTGCCCATCCTGGTCGAGCTG GACGGCGACGTAAACGGCCACAAGTTCAGCGTGTCCGGCGAG GGCGAGGGCGATGCCACCTACGGCAAGCTGACCCTGAAGCTG ATCTGCACCACCGGCAAGCTGCCCGTGCCCTGGCCCACCCTC GTGACCACCCTGGGCTACGGCCTGCAGTGCTTCGCCCGCTAC CCCGACCACATGAAGCAGCACGACTTCTTCAAGTCCGCCATG CCCGAAGGCTACGTCCAGGAGCGCACCATCTTCTTCAAGGAC GACGGCAACTACAAGACCCGCGCCGAGGTGAAGTTCGAGGGC GACACCCTGGTGAACCGCATCGAGCTGAAGGGCATCGACTTC AAGGAGGACGGCAACATCCTGGGGCACAAGCTGGAGTACAAC TACAACAGCCACAACGTCTATATCACCGCCGACAAGCAGAAG AACGGCATCAAGGCCAACTTCAAGATCCGCCACAACATCGAG GACGGCGGCGTGCAGCTCGCCGACCACTACCAGCAGAACACC CCCATCGGCGACGGCCCCGTGCTGCTGCCCGACAACCACTAC CTGAGCTACCAGTCCAAACTGAGCAAAGACCCCAACGAGAAG CGCGATCACATGGTCCTGCTGGAGTTCGTGACCGCCGCCGGG ATCACTCTCGGCATGGACGAGCTGTACAAGTCCGGACTCAGA TCTGGAGGCTTCCACAGAGATGCTGATGAAACCAAAGAATGG ATTGAAGAGAAGAATCAAGCTCTAAACACAGACAATTATGGA CATGATCTCGCCAGTGTCCAGGCCCTGCAACGCAAGCATGAG GGCTTCGAGAGGGACCTTGCGGCTCTCGGTGACAAGGTAAAC TCCCTTGGTGAAACAGCAGAGCGCCTGATCCAGTCCCATCCC GAGTCAGCAGAAGACCTGCAGGAAAAGTGCACAGAGTTAAAC CAGGCCTGGAGCAGCCTGGGGAAACGTGCAGATCAGCGCAAG GCAAAGGGAGGCGTGAATTCCATGGTGAGCAAGGGCGAGGAG CTGTTCACCGGGGTGGTGCCCATCCTGGTCGAGCTGGACGGC GACGTAAACGGCCACAAGTTCAGCGTGTCCGGCGAGGGCGAG GGCGATGCCACCTACGGCAAGCTGACCCTGAAGTTCATCTGC ACCACCGGCAAGCTGCCCGTGCCCTGGCCCACCCTCGTGACC ACCCTGACCTGGGGCGTGCAGTGCTTCGCCCGCTACCCCGAC CACATGAAGCAGCACGACTTCTTCAAGTCCGCCATGCCCGAA GGCTACGTCCAGGAGCGCACCATCTTCTTCAAGGACGACGGC AACTACAAGACCCGCGCCGAGGTGAAGTTCGAGGGCGACACC CTGGTGAACCGCATCGAGCTGAAGGGCATCGACTTCAAGGAG GACGGCAACATCCTGGGGCACAAGCTGGAGTACAACGCCATC AGCGACAACGTCTATATCACCGCCGACAAGCAGAAGAACGGC ATCAAGGCCAACTTCAAGATCCGCCACAACATCGAGGACGGC AGCGTGCAGCTCGCCGACCACTACCAGCAGAACACCCCCATC GGCGACGGCCCCGTGCTGCTGCCCGACAACCACTACCTGAGC ACCCAGTCCAAGCTGAGCAAAGACCCCAACGAGAAGCGCGAT CACATGGTCCTGCTGGAGTTCGTGACCGCCGCCGGGATCACT CTCGGCATGGACGAGCTGTACAAG).

All plasmids for α-actinin-4 FRET-based tension sensors were synthesized and sequenced by Genscript. α-actinin-4-sstFRET522 was constructed by inserting the sstFRET module between 522aa and 523aa of human α-actinin-4 (XP_016882820.1), between the second and third spectrin repeats, and cloned into the blasticidin-selectable pUNO expression vector (Invivogen). The sstFRET is located at 523-1110aa of the α-actinin-4-sstFRET522 open reading frame. α-actinin-4-venus in pUNO was generated by deleting aa523-871 from α-actinin-4 sstFRET522 in pUNO by Genscript. α-actinin-4-CFP in pUNO was generated by deleting aa763-1110 from α-actinin-4-sstFRET522 in pUNO by Genscript. Plasmids for α-actinin-1 FRET-based tension sensors were kindly provided by Fanjie Meng and Frederick Sachs, Physiology and Biophysics Department, SUNY at Buffalo (Meng and Sachs, 2011). α-actinin-1-M-sstFRET containing the sstFRET module inserted between

Morris et al.
Synaptopodin stress fiber and contractomere at the epithelial junction

Journal of Cell Biology 22 of 32
https://doi.org/10.1083/jcb.202011162

300aa and 301aa within the first spectrin repeat of human α-actinin-1 (P12814.2) was in the neomyocin-selectable pcDNA3.1 expression vector (Invitrogen/Thermo Fisher Scientific). Actinin-C-sstFRET containing the sstFRET module added to the C-terminus of human α-actinin-1 (P12814.2) was in pcDNA3.1. Plasmids for mEmerald-occludin (54211), mCherry-ZO-1 (55165), and mCherry-vinculin (55159) were purchased from Addgene. Plasmids for bacterial expression of recombinant α-actinin-4 were generated from PCR products using the coding sequence of human α-actinin-4 (NP_004915.2), kindly provided by Martin Pollak. α-actinin-4 full length (1-911aa), actin-binding domain (1-270aa), and spectrin repeats/EF hands (271-911aa) were subcloned into EcoR1 and Xho1 sites in the kanamycin-selectable bacterial expression vector pET30a+ containing an N-terminal 6His tag (EMD4Biosciences) and the ampicillin-selectable bacterial expression vector pMAL4cx with N-terminal maltose-binding protein. For bacterial expression of recombinant α-actinin-4 sstFRET522, the open reading frame of α-actinin-4 sstFRET522 in pUNO was cloned into Nde1 and XhoI of the bacterial expression vector Pet30a+ in frame with the N-terminal 6His tag by Genscript. ShRNA for canine synaptopodin cloned into puromycin-selectable pRS mammalian expression vector (Origene) has previously been described (Kannan and Tang, 2015).

Cell culture and transfection
HUVEC (OCS-100-013), C2bbE1 (CRL-2102), and T84 (CCL-248) cells were purchased from ATTC. Madin-Darby canine kidney (MDCK) cells were originally from Kai Simons lab (EMBL) and a gift from Barry Gumbiner (University of Washington). The cells have been authenticated by the staining of E-cadherin and ZO-1 using antibodies that only recognize the canine proteins, RR1 for E-cadherin and R40.76 for ZO-1. The cells are free from mycoplasma contamination as determined by the original source. MDCK cells were maintained in MEM/Earle's balanced salt solution supplemented with 25 mM HEPES and 5% fetal bovine serum (FBS) in a 37° incubator in the presence of 5% CO₂. The media was changed every 2–3 days. Cell stocks for parental and transfected cells were stored in a freezing media (normal growth media, 20% FBS, 10% DMSO) in liquid nitrogen. MDCK cells were grown on tissue culture plastic dishes. For live-cell imaging, wound healing, and immunofluorescence, cells were plated on No. 2 VistaVision cover glasses (VWR). For hydraulic chamber experiments and immunofluorescence, cells were plated on 12-mm polyester Transwell-clear with 0.4 μm pores (Corning). A confluent monolayer of MDCK epithelial cells polarized on semi-permeable Transwell support for >2 weeks reaches a steady-state that generates junctions with strong cell–cell adhesion.

For transfection, cells were incubated in a 1:1 mixture of DNA/Polyjet DNA transfection reagent for 5–18 h according to the manufacturer's protocol (SignaGen Laboratories). The expression of plasmid DNA was selected using G418, puromycin, or blasticidin for 10–14 days. Stable expressing clonal cell lines were obtained as published (Kannan and Tang, 2015). Briefly, antibiotic-resistant clonal cell lines were expanded and assessed for knockdown efficiency and protein expression by Western blot and immunofluorescence, respectively. Clonal cell lines

with homogeneous knockdown phenotype were used for a second round of transfection with ShRNA. Secondary clonal cell lines were expanded and assessed for knockdown efficiency by Western blot and immunofluorescence. Clonal cell lines with knockdown efficiency of >80% were used in this study.

For live-cell imaging of α-actinin-4 sstFRET522, α-actinin-1-M-sstFRET, and α-actinin-1-C-sstFRET, synaptopodin-venus cell lines were expanded and assessed for expression using live-cell microscopy.

Drug treatment and wound closure assay
Warmed normal growth media with or without cytochalasin D (at a final concentration of 0.2 μM), latrunculin (at a final concentration of 5 μM), or blebbistatin (at a final concentration of 60 μM) was added to MDCK confluent monolayers 1 h before fixation for immunofluorescence staining. For wound studies, MDCK confluent monolayers were grown on non-permeable glass coverslips for >3–4 weeks. After dome formation, monolayers were rinsed three times with calcium-free phosphate-buffered saline and incubated with calcium-free serum-free MEM media at 37° for 10–15 min until the cells forming the domes were detached from the monolayers. Immediately after that, the calcium-free media was removed and fresh prewarmed normal growth media with or without cytochalasin D (at a final concentration of 0.2 μM), latrunculin (at a final concentration of 5 μM), or blebbistatin (at a final concentration of 60 μM) was gently added to the dishes containing the coverslips with attached MDCK monolayers that now have holes. Cell monolayers were incubated in a 37° incubator for wound closure to proceed. At 1 h after initiation of wound healing, cell monolayers on coverslips were processed immediately for immunofluorescence.

Staining and immunofluorescence of cell
Cells grown on Transwell-Clear (Corning) were used in localization studies. For immunofluorescence, cells were rinsed twice in 150 mM NaCl/2 mM CaCl₂/2 mM MgCl₂/20 mM HEPES, pH 7.8 and fixed in 1% formaldehyde/150 mM NaCl/2 mM CaCl₂/2 mM MgCl₂/20 mM HEPES, pH 7.8 at 4°C for 1 h. The reaction was quenched with Tris in quenching buffer (0.05% Triton X-100/50 mM Tris/100 mM NaCl/20 mM HEPES, pH 8.0) for 3 h. The Transwell with fixed cells was rinsed in immunofluorescence staining buffer (0.05% Triton X-100/100 mM NaCl/20 mM HEPES, pH 7.5) and the cells were incubated with primary antibodies (1 μg/ml) in staining buffer overnight. After rinsing in staining buffer three times, the cells were incubated with secondary antibodies (labeled with Alexa 488, 568, or 647, see antibodies section above) in staining buffer for 90 min. Then, the cells were rinsed three times in staining buffer and incubated with fluorescently labeled (FITC, TRITC, or Alexa 647) phalloidin or Hoechst 33528 for 60 min. Finally, the cells were rinsed three times in staining buffer and post-stain fixed with 1% formaldehyde in staining buffer for 3 h. Transwell filters were excised using a razor blade and mounted with No. 1 glass coverslips on glass slides with ProLong Glass antifade (Invitrogen). Stained cells with antifade were allowed to cure for 48 h before being used for imaging.

Morris et al.
Synaptopodin stress fiber and contractomere at the epithelial junction

Journal of Cell Biology   23 of 32
https://doi.org/10.1083/jcb.202011162

Image acquisition of fixed cell

Fixed cells were imaged at room temperature. Images were collected in 200-nm steps using Axio Imager.Z2m microscope equipped with Apotome.2 (Carl Zeiss) and X-cite 120 LED (Lumen Dynamics) using Zen2 Zeiss Software. For Optical Sectioning Structured Illumination Microscopy (OS-SIM), seven phases/images were collected per each constructed image using either α Plan-Apochromat 100×/NA1.46 Oil DIC M27 or Plan-Apochromat 40×/NA1.3 Oil DIC M27 objectives (Carl Zeiss) and a 4K ORCA-Flash4.0 V2 digital CMOS camera with 6.5 µm × 6.5 µm pixel size (Hamamatsu Photonics). Wide-field optical z images were deconvolved (constrained iterative) using the Zen2 pro deconvolution module. 3D reconstitutions of 200-nm z-stacks were performed using Zeiss Zen2 software. Low magnification wide-field images were collected using Plan Apochromat 20×/0.8 objectives (Zeiss). Images for Figs. S1 B; and S2, A and B were collected using a 2K Optimos CMOS camera with 6.5 µm × 6.5 µm pixel size (Qimaging; Photometrics). Figs. 4 A, S3 A, S4 B, S6 A, S6, C and D, S7, A–C; and S8, D and E were generated by collecting six phases per image using Apotome2 (Zeiss) with Plan-Apochromat 40×/NA1.3 Oil DIC M27 objectives (Carl Zeiss) and a 4K ORCA-Flash4.0 V2 digital CMOS camera with 6.5 µm × 6.5 µm pixel size (Hamamatsu Photonics). Figs. 1, D and E; 9 D, 9, F–H, S1 B, S2, A and B, and S14, A and B were generated by collecting six phases per image using Apotome2 (Zeiss) with α Plan-Apochromat 100×/NA1.46 Oil DIC M27 and a 4K ORCA-Flash4.0 V2 digital CMOS camera with 6.5 µm × 6.5 µm pixel size (Hamamatsu Photonics). Figs. 1, A–C and 9 A were single z-image slice deconvolved using Zeiss constrained iterative deconvolution (Zen2) from 200 nm z-stacks collected with α Plan-Apochromat 100×/NA1.46 Oil DIC M27 and a 4K ORCA-Flash4.0 V2 digital CMOS camera with 6.5 µm × 6.5 µm pixel size (Hamamatsu Photonics).

Composite images were generated using ImageJ (National Institutes of Health) and Zen (Carl Zeiss) software. For figure generation, images were cropped, contrasted (no gamma adjustments), and scaled using Photoshop software (Adobe) before importing into Illustrator (Adobe).

Live-cell imaging setup

For live-cell imaging, glass coverslips were soaked in 100% ethanol and sterilized under UV for 60 min. Sterilized coverslips were coated with 20 µg/ml collagen IV in phosphate-buffered saline for 60 min and used immediately for plating of cells. Cells grown on collagen-coated or uncoated glass coverslips were mounted up-side-down on an in-house fabricated polycarbonate chamber with a deep well for media for long-term imaging. Live-imaging was performed in FluoroBrite/DMEM (Gibco) media containing 10% fetal bovine serum and 10 mM HEPES, pH 7.5. The sample temperature was maintained at 35°C on a heated stage and an objective heater (PeCon). For drug treatments, cells were treated for 1 h before imaging in pre-warmed normal growth media with or without cytochalasin D (at a final concentration of 0.2 µM), ML-7 (at a final concentration of 10 µM), or Latrunculin B (at a final concentration of 5 µM). Images were collected using ORCA-Flash4.0 (Hamamatsu Photonics) or

Optimos (Qimaging) mounted onto Axio Imager.Z2m (Zeiss) with X-cite 120 LED (Lumen Dynamics).

For movie generation, individual images of cropped cells were imported into Image J to generate avi files, and the avi files were imported into Media Encoder (Adobe) to generate mpeg files. Composite images were generated using ImageJ or Photoshop . Individual cell diameter and junction for each image were measured using ImageJ or Zen (Carl Zeiss).

Live-cell imaging of α-actinin FRET and synaptopodin

α-Actinin tension sensors were imaged using the Gemini dual-view system (Hamamatsu Photonics) equipped with an excitation filter for Cerulean fluorescence protein (CeFP) and emission filters for Cerulean fluorescence protein (CeFP) and Venus fluorescence protein (VFP). Simultaneous acquisition of images for CeFP and VFP emission were obtained using a Plan-Apochromat 40×/NA1.3 Oil DIC M27 objective (Zeiss). Junctional intensities of CeFP and VFP were used to calculate the FRET index (EmVFP)/(EmCeFP + EmVFP), which is shown as FRET/(CeFP + FRET). Briefly, the CeFP and VFP channels were overlaid on top of each other using a macro written using the Zen2 software (Carl Zeiss). Each junctional region is outlined manually with a rectangle drawing tool in the Zen2 imaging tool (Zeiss). Contractomeres were circled with 9-pixel diameter and 160 nm per pixel resolution. The intensities of the junctional signal were measured and subtracted from the background signal (an area with no cells or within the cytoplasm) before being used for the calculation of the FRET index. For α-actinin-4-venus and α-actinin-4-CFP imaging controls, areas were circled with 9-pixel diameter at 160 nm per pixel resolution. CFP (excitation filter for CeFP and emission filter for CeFP) and FRET (excitation filter for CeFP and emission filter for YFP) signals at the linear junction, contractomere, and cytoplasm were subtracted from background measurements (area with no α-actinin). The ratio of FRET to CFP was used for excited emission.

Image analysis

All images were corrected for chromatic shift on the X, Y, and Z-axes for each fluorescence channel before were being used for analysis. Quantitation of actin (phalloidin) and junction proteins (immunofluorescence intensity) was performed in ImageJ or Zen (Carl Zeiss) using unprocessed original single optical z-slice images. A defined area was used to compare the signal intensity of actin (phalloidin) and immunofluorescence of junctional proteins. All measured intensities were subtracted from the background signal (an area with no cells or within the cytoplasm) before being used for statistical analyses and calculation of intensity ratios. For analyses of intensities, each junctional region is outlined using a rectangle box tool and each contractomere is outlined using a circle tool using ImageJ or Zen2. The mean pixel intensity of each defined junctional region is used for comparison of junction localization of the individual protein. Line intensity graphs were generated in Excel (Microsoft) using pixel intensities from original images. For the measurement of junctional length, distance between cell vertices, and perimeter, a free-drawing tool and a line tool were used to trace outlines and draw straight lines (ImageJ). All experiments

had been repeated at least three times. At least six data sets from each experiment were collected.

Statistical analysis

KaleidaGraph software (synergy) was used for graphing all scatter plots and performing all statistical analyses, including the non-parametric Wilcoxon-Mann-Whitney test (unpaired), standard errors, and least squares curve fit (Pearson's R). For calculation of Pearson's correlation coefficient R and P value of non-parametric Wilcoxon-Mann-Whitney test, intensities of the individual pixel within the defined junctional region were used, and each pixel corresponds to 45 nm × 45 nm of the imaged sample.

Immunoprecipitation

Stable clonal cell lines expressing α-actinin-4-sstFRET522 were plated at ~70% confluent density and allowed to grow for 2 d. Cell were homogenized using a 25G needle and extracted with 1% TX-100, 0.5% deoxycholate, 0.2% SDS, 2 mM EDTA, 150 mM NaCl, 20 mM HEPES, and pH 8 with protease inhibitors (10 µg/ml Leupeptin, 1 mg/ml Pefabloc, 10 µg/ml E-64, 2 µg/ml antipain, 2 µg/ml aprotinin, 50 µg/ml bestatin, 20 µg/ml calpain inhibitors I, and 10 µg/ml calpain inhibitor II) at 4°C for 2 h. Insoluble materials were pelleted by spinning the cell extract for 30 min at 16,000 g. Supernatants were incubated with anti-Venus antibodies for 6 h. The antibodies–cell lysates were then incubated overnight with Protein G Agarose (P-430, GoldBio). The beads were washed four times in extraction buffer, followed by once with 500 mM NaCl, 10 mM Hepes, pH 8 and then twice with 5 mM HEPES, pH 8. The bound fractions were solubilized in SDS-PAGE sample buffer for Western blots as described below.

Western blots and quantitative analysis

For comparison of young and mature monolayers, confluent monolayers of the cells were trypsinized and replated at a high confluent density (10^7 cells per 10 cm). Cells were allowed to form cell–cell interactions for 2 d (young) or 7 d (mature). Total cell lysates were obtained by solubilizing the cells in SDS-PAGE sample buffer containing 25 mM dithiothreitol, 2% SDS, 50 mM Tris-Cl, 5% glycerol, pH 8.8, and protease inhibitors (10 µg/ml Leupeptin, 1 mg/ml Pefabloc, 10 µg/ml E-64, 2 µg/ml antipain, 2 µg/ml aprotinin, 50 µg/ml bestatin, 20 µg/ml calpain inhibitors I, and 10 µg/ml calpain inhibitor II). For Western blot of phosphorylated myosin light chain, cell extraction was carried out as above with the addition of a phosphatase inhibitor cocktail (Simple Stop 1 #GB-450) purchased from Gold Biotechnology. Biorad DC detergent compatible protein assay was used to determine total protein concentration in cell lysates. Equal protein amounts of cell lysates were used for the comparison of junctional protein. SDS-PAGE was performed using 8–16% gradient gel (Criterion; BioRad) and transferred to nitrocellulose paper using Transblot (BioRad). Western blots were carried out using iBind with 1 µg/ml primary antibodies and 1 µg/ml secondary antibodies by following the iBind protocol (Invitrogen/Thermo Fisher Scientific). Western blots were developed using Clarity Max ECL substrate (BioRad),

and the images were captured using ChemiDoc Imaging system (BioRad).

Western blot images were analyzed using Image J. Band intensities were subtracted from the background (empty lane) before calculation of fractional intensities. Two samples were loaded for each condition and the average of band intensities were used for the following calculations. For probability calculation of randomized dimerization, the band intensities of endogenous α-actinin-4 (=0.953574) and α-actinin-4-sstFRET522 (=0.046426) of α-actinin-4 Western blot were used.

For calculations of fractions of homodimers and heterodimers of endogenous α-actinin-4 and α-actinin-4-sstFRET522, a probability equation based on random dimerization was used; the fractions are represented in square [ ] brackets. For random dimerization, the predicted fraction of homodimers formed between endogenous α-actinin-4 is (endogenous α-actinin-4) × (endogenous α-actinin-4) = (0.953574)(0.953574) = 0.9093033. For random dimerization, the predicted fraction of homodimers formed between α-actinin-4sstFRET522 is (α-actinin-4sstFRET522) × (α-actinin-4sstFRET522) = (0.046426)(0.046426) = 0.0021553. For random dimerization, the predicted fraction of heterodimers formed between endogenous α-actinin-4 and α-actinin-4-sstFRET522 is 2 × (endogenous α-actinin-4) × (α-actinin-4sstFRET522) = 2(0.953574)(0.046426) = 0.0885412.

The actual fraction of unstable heterodimer formed between endogenous α-actinin-4 and α-actinin-4-sstFRET522 (= the unstable fraction) was calculated using the measured band intensities of endogenous α-actinin-4 (= 0.0563393) and α-actinin-4-sstFRET522 (= 0.9436607) in Western blot of anti-venus immunoprecipitation (venus-IP): (2 × [predicted fraction of α-actinin-4-sstFRET522 in homodimer] + [predicted fraction of α-actinin-4-sstFRET522 in heterodimer] – [unstable fraction])/([predicted fraction of endogenous α-actinin-4 in heterodimer] – [unstable fraction]) = measure band intensity of α-actinin-4 sstFRET522/measure band intensity of endogenous α-actinin-4. Solving the unstable fraction by substituting the modified equation with measured and calculated values: (2[0.0021553] + 0.0885412-unstable fraction)/(0.0885412-unstable fraction) = (0.9436607/0.0563393), the unstable fraction was computed to be 0.0882675. The actual fraction of α-actinin-4sstFRET522 in the heterodimer formed between endogenous α-actinin-4 and α-actinin-4-sstFRET522 is the (predicted heterodimer fraction) – (unstable heterodimer fraction) = 0.0885412 – 0.0882675 = 0.0002737. The actual fraction of α-actinin-4-sstFRET522 homodimer is the (predicted fraction of α-actinin-4-sstFRET522 homodimer) + (unstable fraction of α-actinin-4-sstFRET522 heterodimer)/2 = 0.00021553 + (0.0882675/2) = 0.04434928. The ratio of actual α-actinin-4-sstFRET522 heterodimer to homodimer is 0.0002737–0.04434928 = 1:164. Thus, α-actinin-4sstFRET522 homodimer would be responsible for 1 – (0.0002737/0.04434928) = 0.9938 = 99.4% of the FRET signal.

Active rho detection

Rho activity was assayed using the Active Rho Detection Kit (#8820; Cell Signaling Technology). Briefly, confluent monolayers of MDCK and synaptopodin knockdown cells were lyzed and the supernatants were used for immunoprecipitation using

Morris et al.
Synaptopodin stress fiber and contractomere at the epithelial junction

Journal of Cell Biology 25 of 32
https://doi.org/10.1083/jcb.202011162

GST–Rhotekin–Rho-binding domain. The immunoprecipitated protein complexes were eluted in SDS sample buffer and ran on an SDS-PAGE gel. Rho levels in Rhotekin immunoprecipitations were detected by performing a Western blot using anti-Rho antibodies.

Recombinant protein expression, purification, and fluorophore labeling

For expression of recombinant proteins, cDNA plasmids were transformed into Rosetta DE3 E. coli cells containing tRNAs for "universal" "translation" (Novagen) maintained under chloramphenicol. For recombinant 6-His tagged α-actinin-4, actin-binding domains, and spectrin repeats/EF hands, the protein expressions were induced with 500 µM isopropyl β-D-1-thio-galactopyranoside for 8 h at 25°C in LB containing chloramphenicol. Cells were centrifuged at 6,000 g for 15 min and resuspended in 20 mM NaCl, 20 mM HEPES, pH 7.8 in the presence of 5 mg/ml lysozyme. After one freeze–thaw cycle, lysed cells were centrifuged at 100,000 g for 30 min. The supernatant was loaded onto a nickel column (Qiagen). The column was washed with 20 bed volumes of 500 mM NaCl, 25 mM imidazole, and 20 mM HEPES, pH 7.8. The recombinant proteins were eluted with 10 bed volumes of 500 mM NaCl, 500 mM Imidazole, 20 mM HEPES, and pH 7.8. Eluted proteins were concentrated using Centricon filters (Millipore, Inc) and purified by gel filtration using Superdex 200 in 150 NaCl, 20 mM HEPES, 10 mM β-mercaptoethanol. Proteins were either frozen or used immediately for labeling. Recombinant α-actinin-4 proteins were labeled on cysteine using maleimide-activated Oregon Green at a ratio of five fluorophores for every α-actinin at room temperature for 1 h. Labeled proteins were separated from free dyes by gel filtration using Superdex 200 in 150 NaCl, 20 mM HEPES, 10 mM β-mercaptoethanol.

For the expression of heterodimeric α-actinin-4 that consists of one monomer of full-length and one monomer of spectrin-repeats/EF hands, plasmid pet30a+ with full-length α-actinin-4 and plasmid pMAL-4cx with spectrin repeats/EF hands were transformed together into Rosetta DE3 cells. Cells expressing both constructs were selected with ampicillin, chloramphenicol, and kanamycin and maintained in LB containing 10 mM glucose to suppress the expression of MBP-fusion protein. To induce protein expression, 200 µmp isopropyl β-D-1-thiogalactopyr-anoside was added to the LB growth media for 8 h at 25°. Cells were centrifuged at 6,000 g for 15 min and resuspended in 20 mM NaCl, 20 mM HEPES, pH 7.8 in the presence of 5 mg/ml lysozyme. After one freeze–thaw cycle, lysed cells were centrifuged at 100,000 g for 30 min. The supernatant was loaded onto an amylose column three times (NED), washed with 20 bed volumes of 100 mM NaCl, 20 mM HEPES, pH 7.8, and eluted with 10 mM maltose in 100 mM NaCl, 20 mM HEPES, pH 7.8. The eluted fraction was loaded onto a nickel column (Qiagen). The column was washed with 20 bed volumes of 500 mM NaCl, 25 mM Imidazole, and 20 mM HEPES, pH 7.8. The recombinant proteins were eluted with 10 bed volumes of 500 mM NaCl, 500 mM Imidazole, 20 mM HEPES, pH 7.8. Eluted proteins were concentrated using Centricon filters (Millipore, Inc) and purified by gel filtration using Superdex 200 in 150 NaCl, 20 mM HEPES, and 10 mM β-mercaptoethanol.

For the expression of recombinant α-actinin-4 sstFRET522, plasmid pet30a+ with α-actinin-4-sstFRET522 was transformed into Rosetta DE3 cells. Cells expressing the construct were selected with kanamycin and chloramphenicol. To induce protein expression, 200 µM isopropyl β-D-1-thiogalactopyranoside was added to the LB growth media for 8 h at 25°. Cells were centrifuged at 6,000 g for 15 min and resuspended in 20 mM NaCl, 20 mM HEPES, pH 7.8 in the presence of 5 mg/ml lysozyme. After one freeze–thaw cycle, lysed cells were centrifuged at 100,000 g for 30 min. The supernatant was loaded onto a nickel column (Qiagen). The column was washed with 20 bed volumes of 500 mM NaCl, 25 mM Imidazole, and 20 mM HEPES, pH 7.8. The recombinant α-actinin-4 sstFRET522 was eluted with 10 bed volumes of 500 mM NaCl, 500 mM imidazole, 20 mM HEPES, pH 7.8. The eluted proteins were concentrated using Centricon filters (Millipore, Inc) and dialyzed in 100 NaCl, 10 mM HEPES, pH 7.8, 5 mM β-mercaptoethanol.

Actin was purified from rabbit skeletal muscle acetone powder (Pelfrez). Actin is extracted from acetone powder in 2 mM Tris (pH 8), 0.2 mM ATP, 0.5 mM DTT, 0.1 mM CaCl2 on ice for 30 min. Insoluble materials were removed by pelleting at 20,000 g for 30 min at 4°C. The supernatant was then passed through a cheesecloth. Actin monomers in the supernatant were allowed to polymerize at room temperature by the addition to a final concentration of 50 mM KCl and 2 mM MgCl2. Actin polymers were stripped with actin-binding proteins by the addition to a final concentration of 800 mM KCl in the cold room while stirring. Actin filaments were pelleted at 100,000 g for 30 min at 4°C. Actin was depolymerized by resuspending the pellet in 2 mM Tris (pH 8), 0.2 mM ATP, 0.5 mM DTT, 0.1 mM CaCl2 using a Dounce homogenizer. Monomeric actin was cleared of precipitation by centrifugation at 100,000 g for 30 min at 4°C. Actin polymerization and depolymerization cycles were carried out two additional times to get rid of actin-binding proteins. Monomeric actin was snap-frozen in liquid nitrogen and stored at –80°C until use.

Monomeric actin was labeled on lysine residues using NHS activated rhodamine, Alexa 647, or Oregon green for 1 h at room temperature. After labeling, actin filaments were pelleted at 100,000 g for 30 min, resuspended in G buffer, and dialyzed exhaustively against G buffer (0.2 mM ATP, 0.2 mM CaCl$_2$, 5 mM Tris-HCl, pH 8, 1 mM β-mercaptoethanol). This procedure typically labeled actin to 50–80%. Aliquots of proteins were snap-frozen in liquid nitrogen and stored at –80°C until use. Protein concentrations were determined by Bradford assay (BioRad).

Purification of junction-enriched membrane

Junction-enriched membranes were prepared from rat livers (Pelfrez). The frozen livers were thawed in two volumes of 10 mM HEPES, pH 8.5, and 10 mM DTT in a cold room. Protease inhibitors (see above) were added to the thawed livers and the livers were blended in a Waring blender (5 × 15 s) in the cold room. The liver slush was filtered through four layers of cheesecloth to obtain the total liver homogenate. The total liver

Morris et al.
Synaptopodin stress fiber and contractomere at the epithelial junction

Journal of Cell Biology   26 of 32
https://doi.org/10.1083/jcb.202011162

homogenate was centrifuged at 1,000 g for 30 min at 4°C. The pellet was homogenized in 10 mM HEPES, pH 8.5/10 mM DTT in a Dounce homogenizer and centrifuged at 100 g for 30 min. The supernatant was collected and centrifuged at 1,000 g for 30 min at 4°C. The membrane pellet was homogenized again in 10 mM HEPES, pH 8.5/10 mM DTT, and the homogenate was centrifuged at 1,000 g for 30 min at 4°C. The washed membrane pellet contains the majority of junction actin assembly activity and was frozen at –80° before further purification immediately before use in assays. On the day of the experiment, membranes were thawed on ice, diluted 1:1 with 10 mM HEPES, pH 8.5, supplemented with 10 mM DTT, and homogenized through a 25G needle. The homogenates were spun through a 20% sucrose pad for 10 min at 16,000 g. The supernatant was discarded and the pellet was resuspended with 10 mM HEPES, pH 8.5 supplemented with 10 mM DTT. The homogenate was spun through a 20% sucrose pad for 15 min at 1,000 g. The pellet was discarded and the supernatant was spun through a 20% sucrose pad for 15 min at 16,000 g. The membrane pellet contains junction-enriched plasma membrane fragments as determined by Western blots and immunostaining (Tang and Brieher, 2012).

Actin bundling assay

Actin bundling assays were performed by adding 1 µM of recombinant α-actinin-4 to 3 µM of fluorescently-labeled G-actin in actin polymerization buffer (50 mM KCl, 2 mM EGTA, 2 mM MgCl₂, and 100 mM HEPES, pH 7.8) supplemented with 2 mM buffered ATP, pH 8. The reactions were allowed to proceed at room temperature for 2 h. Actin bundling reactions were mounted on a glass slide using a No. 1.5 coverslip and imaged using an Apochromat 40×/NA1.3 Oil DIC M27 objective (Carl Zeiss) on an Axio Imager.Z2m microscope equipped with ORCA-ER CCD camera with 6.45 µm × 6.45 µm pixel size (Hamamatsu Photonics) and X-cite 120 LED illumination (Lumen Dynamics). For figure generation, the images were cropped, contrasted, and scaled using Photoshop software (Adobe) before importing into Illustrator (Adobe).

Actin membrane assembly reaction and membrane immunofluorescence

Membrane actin assembly reactions were performed in actin polymerization buffer (50 mM KCl, 2 mM EGTA, 2 mM MgCl₂, and 100 mM HEPES, pH 7.8) supplemented with 2 mM buffered ATP, pH 8. A standard 20-µl reaction consists of ~15 µg of total proteins from the purified junctional membrane fraction and 0.5–2 µM rhodamine or Oregon green-labeled monomeric actin. Actin polymerization was carried out at room temperature for 30–120 min.

For reconstitution assays, purified membranes were stripped with high salt (500 mM NaCl, 2 mM MgCl₂, 2 mM EGTA, 20 mM HEPES, pH 7.8, and 10 mM DTT), TX-100, or CHAPS (in 50 mM NaCl, 2 mM MgCl₂, 2 mM EGTA, 20 mM HEPES, pH 7.8, and 10 mM DTT) on ice for 1 h. Stripped membranes were collected by centrifugation through a 20% sucrose cushion at 10,000 g for 5 min and resuspended in actin polymerization buffer (50 mM KCl, 2 mM EGTA, 2 mM MgCl₂, and 100 mM HEPES, pH 7.8). Purified proteins (labeled and unlabeled α-actinin-4) were added to resuspended stripped membranes and allowed to bind to the membranes for 1 h at room temperature. Unbound proteins were removed by spinning the membranes through a 20% w/w sucrose cushion at 10,000 g for 5 min and resuspended in actin polymerization buffer. The final reconstituted reaction consisted of ~8 µg of total protein from stripped membranes, 0.5 µM fluorescently labeled monomeric actin, and recombinant proteins (α-actinin-4) and was carried out at room temperature for 30–60 min.

For the two-color actin assembly assay, the first half of the actin assembly reaction was carried out at room temperature for 30–60 min using 0.3–0.5 µM green fluorescence-labeled monomeric actin, followed by the removal of monomeric actin by spinning the membrane through a 20% w/w sucrose cushion at 10,000 g for 5 min. The membrane–actin pellet was resuspended in actin polymerization buffer with fresh ATP and allowed to form compact actin puncta over the next few hours. The membrane–actin reaction was then purified again by spinning the membrane through a 20% w/w sucrose cushion at 10,000 g for 5 min. The second half of the actin assembly reaction was carried out at room temperature for 30–60 min by the addition of 0.3–0.5 µM of rhodamine-labeled monomeric actin.

For immunofluorescence of membranes, the actin assembly assay was performed and membranes were collected by centrifugation through a 20% sucrose cushion at 10,000 g for 5 min. The purified membranes with incorporated actin were incubated with primary antibodies in the presence of 0.1% TX-100 in actin assay buffer for 2 h. The membranes were spun through a 20% sucrose cushion and resuspended in 0.1% TX-100 in assay buffer. The membranes were incubated with secondary antibodies for 2 h, spun through a 20% sucrose cushion, and resuspended in 0.1% TX-100 in assay buffer. The membranes were mounted on a glass slide and covered with a No. 1.5 glass coverslip before imaging. Images were obtained using a Plan-Apochromat 63×/NA 1.4 Oil DIC M27 objective (Carl Zeiss) attached to an Axio Imager (Carl Zeiss) equipped with ORCA-ER CCD camera with 6.45 µm × 6.45 µm pixel size (Hamamatsu Photonics) and the Colibri Illumination System (Carl Zeiss). For figure generation, images were cropped, contrasted, and scaled using Photoshop software (Adobe) before importing into the Illustrator (Adobe).

Electron microscopy

For visualization of actin with the junctional complex on a purified native membrane sheet, the actin assembly reaction was performed using Oregon green-labeled monomeric actin at a final concentration of 1 µM. Actin polymerization was carried out at room temperature for 30–90 min. The reaction was purified by spinning through a 20% w/w sucrose cushion at 10,000 g for 5 min. Purified native membranes with incorporated actin were resuspended in 10 µl of actin polymerization buffer. A total of 4 µl of the resuspended membranes was used for wide-field light microscopy as described above and 5 µl of the resuspended membranes was processed for electron microscopy analysis. Experiments were repeated at least six times.

To dissociate membrane sheets into smaller fragments, native membranes were purified by spinning through a 20% w/w

Morris et al.
Synaptopodin stress fiber and contractomere at the epithelial junction

Journal of Cell Biology   27 of 32
https://doi.org/10.1083/jcb.202011162

sucrose cushion at 10,000 g for 5 min, followed by gentle shearing of the membrane pellet in 10 mM Hepes, pH 7.8 using a 20 µl pipette tip. Dissociated smaller membrane fragments were purified again by spinning through a 20% w/w sucrose cushion at 10,000 g for 10 min. Actin assembly reaction was performed using rhodamine-labeled monomeric actin at a final concentration of 0.5 µM. Actin polymerization was carried out at room temperature for 30–90 min. The reaction was purified by spinning through a 20% w/w sucrose cushion at 10,000 g for 10 min. The membrane with incorporated actin was resuspended in 10 µl of actin polymerization buffer. A total of 4 µl of the resuspended membranes was used for wide-field light microscopy as described above and 5 µl of the resuspended membranes was processed for electron microscopy analysis. Experiments were repeated at least three times.

To dissociate the contractomeric-actin into smaller complexes, membrane fragments from the above 10 mM Hepes, pH 7.8 dissociation were used for the actin assembly reaction. The actin assembly reaction was carried out at room temperature for 60 min using rhodamine-labeled monomeric actin at a final concentration of 0.5 µM. The membrane reaction was purified by spinning through a 20% w/w sucrose cushion at 10,000 g for 10 min. The membrane–actin pellet was resuspended in 10 mM Hepes, pH 9, and sheared using a 20 µl pipet tip. The mechanically dissociated membranes were purified again by spinning through a 20% w/w sucrose cushion at 10,000 g for 10 min. The membrane–actin pellet was resuspended in 10 µl of actin polymerization buffer. A total of 4 µl of the resuspended membranes was used for wide-field light microscopy to confirm the presence of contractomeric actin complexes and 5 µl of the resuspended membranes was processed for electron microscopy analysis.

The resuspended membrane reactions were allowed to attach onto glow-discharged carbon-coated grids for 10 min. The unbound membranes were removed by washing the EM grids three times with assembly buffer. The membranes were negatively stained with 2% uranyl acetate and the excess stain was removed immediately. The grids were allowed to air dry for 10 min and stored until viewing the image under an electron microscope. Images were collected with a JEOL 2100EX at 120 kV using a 2K × 2K CCD camera (UltraScan; Gatan, Inc.). For figure generation, images were cropped, contrasted, and scaled using Photoshop software (Adobe) before importing into the Illustrator (Adobe).

Online supplemental material
A total of 14 supplementary figures and 35 movies are described in the main text. Fig. S1 shows synaptopodin localization at junctions and stress fibers of epithelial and endothelial cells. Fig. S2 shows apical stress fibers inserted at the apical junctions of epithelial cells. Fig. S3 shows vinculin at basal junctions and ZO-1 at both apical and basal junctions. Fig. S4 shows retrograde synaptopodin flow from basal junctions. Fig. S5 shows synaptopodin retrograde flow during early development, contraction during maturation, and anterograde flow toward junction vertex during the late stage of maturation. Fig. S6 shows

contractomeres formed at a late stage of junction maturation. Fig. S7 shows that contractomeres are stationary in the mature monolayer. Fig. S8 shows that contractomeres move during cell extrusion in the mature monolayer. Figs. S9, S10, S11, and S12 shows Negative stain EM of actin assembled at the contractomere. Fig. S13 shows that a new α-actinin-4 force sensor targets contractomeres and supports actin assembly. Fig. S14 shows that synaptopodin knockdown does not affect RhoA. Videos 1, 2, 3, 4, 6, 7, 8, 9, 10, 11, 12, 13, 14, 15, 16, 17, 32, and 33 are live-cell time-lapse of Venus-synaptopodin and mCherry-ZO-1. Video 5 is live-cell time-lapse of Venus-synaptopodin and mCherry-vinculin. Videos 18, 19, and 20 are live-cell time-lapse of Venus-synaptopodin. Videos 21, 22, and 23 are structured-illumination live-cell time-lapse of Venus-synaptopodin and mCherry-ZO-1. Video 24 is live-cell time-lapse of mCherry-ZO-1. Videos 25, 26, and 27 is live-cell time-lapse of venus-α-actinin-1. Videos 28 and 29 are structured-illumination live-cell time-lapse of Venus-α-actinin-1. Videos 30 and 31, 33, 34, and 35 are live-cell time-lapse of mEmerald-occludin.

Acknowledgments

References
Abreu-Blanco, M.T., J.M. Verboon, R. Liu, J.J. Watts, and S.M. Parkhurst. 2012. Drosophila embryos close epithelial wounds using a combination of cellular protrusions and an actomyosin purse string. *J. Cell Sci.* 125: 5984–5997. https://doi.org/10.1242/jcs.109066

Amano, M., M. Ito, K. Kimura, Y. Fukata, K. Chihara, T. Nakano, Y. Matsuura, and K. Kaibuchi. 1996. Phosphorylation and activation of myosin by rho-associated kinase (Rho-kinase). *J. Biol. Chem.* 271:20246–20249. https://doi.org/10.1074/jbc.271.34.20246

Anderson, J.M., B.R. Stevenson, L.A. Jesaitis, D.A. Goodenough, and M.S. Mooseker. 1988. Characterization of ZO-1, a protein component of the tight junction from mouse liver and Madin-Darby canine kidney cells. *J. Cell Biol.* 106:1141–1149. https://doi.org/10.1083/jcb.106.4.1141

Anekal, P.V., J. Yong, and E. Manser. 2015. Arg kinase-binding protein 2 (ArgBP2) interaction with alpha-actinin and actin stress fibers

inhibits cell migration. *J. Biol. Chem.* 290:2112–2125. https://doi.org/10.1074/jbc.M114.610725

Aoki, R., T. Kitaguchi, M. Oya, Y. Yanagihara, M. Sato, A. Miyawaki, and T. Tsuboi. 2010. Duration of fusion pore opening and the amount of hormone released are regulated by myosin II during kiss-and-run exocytosis. *Biochem. J.* 429:497–504. https://doi.org/10.1042/BJ20091839

Arai, Y., R. Yasuda, K. Akashi, Y. Harada, H. Miyata, K. Kinosita Jr., and H. Itoh. 1999. Tying a molecular knot with optical tweezers. *Nature.* 399:446–448. https://doi.org/10.1038/20894

Asanuma, K., K. Kim, J. Oh, L. Giardino, S. Chabanis, C. Faul, J. Reiser, and P. Mundel. 2005. Synaptopodin regulates the actin-bundling activity of alpha-actinin in an isoform-specific manner. *J. Clin. Invest.* 115:1188–1198. https://doi.org/10.1172/jci200523371

Asanuma, K., E. Yanagida-Asanuma, C. Faul, Y. Tomino, K. Kim, and P. Mundel. 2006. Synaptopodin orchestrates actin organization and cell motility via regulation of RhoA signalling. *Nat. Cell Biol.* 8:485–491. https://doi.org/10.1038/ncb1400

Badirou, I., J. Pan, C. Legrand, A. Wang, L. Lordier, S. Boukour, A. Roy, W. Vainchenker, and Y. Chang. 2014. Carboxyl-terminal-dependent recruitment of nonmuscle myosin II to megakaryocyte contractile ring during polyploidization. *Blood.* 124:2564–2568. https://doi.org/10.1182/blood-2014b06-584995

Bailly, M., F. Macaluso, M. Cammer, A. Chan, J.E. Segall, and J.S. Condeelis. 1999. Relationship between Arp2/3 complex and the barbed ends of actin filaments at the leading edge of carcinoma cells after epidermal growth factor stimulation. *J. Cell Biol.* 145:331–345. https://doi.org/10.1083/jcb.145.2.331

Beach, J.R., and T.T. Egelhoff. 2009. Myosin II recruitment during cytokinesis independent of centralspindlin-mediated phosphorylation. *J. Biol. Chem.* 284:27377–27383. https://doi.org/10.1074/jbc.M109.028316

Beach, J.R., L. Shao, K. Remmert, D. Li, E. Betzig, J. Hammer, and J.A. Hammer 3rd. 2014. Nonmuscle myosin II isoforms coassemble in living cells. *Curr. Biol.* 24:1160–1166. https://doi.org/10.1016/j.cub.2014.03.071

Bement, W.M., P. Forscher, and M.S. Mooseker. 1993. A novel cytoskeletal structure involved in purse string wound closure and cell polarity maintenance. *J. Cell Biol.* 121:565–578. https://doi.org/10.1083/jcb.121.3.565

Berro, J., A. Michelot, L. Blanchoin, D.R. Kovar, and J.L. Martiel. 2007. Attachment conditions control actin filament buckling and the production of forces. *Biophys. J.* 92:2546–2558. https://doi.org/10.1529/biophysj.106.094672

Billington, N., A. Wang, J. Mao, R.S. Adelstein, and J.R. Sellers. 2013. Characterization of three full-length human nonmuscle myosin II paralogs. *J. Biol. Chem.* 288:33398–33410. https://doi.org/10.1074/jbc.M113.499848

Bois, P.R.J., R.A. Borgon, C. Vonrhein, and T. Izard. 2005. Structural dynamics of alpha-actinin-vinculin interactions. *Mol. Cell Biol.* 25:6112–6122. https://doi.org/10.1128/MCB.25.14.6112-6122.2005

Boyle, S.N., and A.J. Koleske. 2007. Use of a chemical genetic technique to identify myosin IIb as a substrate of the Abl-related gene (Arg) tyrosine kinase. *Biochemistry.* 46:11614–11620. https://doi.org/10.1021/bi701119s

Bresnick, A.R. 1999. Molecular mechanisms of myosin-II regulation. *Curr. Opin. Cell Biol.* 11:26–33. https://doi.org/10.1016/s0955-0674(99)80004-0

Burridge, K., and C. Guilluy. 2016. Focal adhesions, stress fibers and mechanical tension. *Exp. Cell Res.* 343:14–20. https://doi.org/10.1016/j.yexcr.2015.10.029

Cavanaugh, K.E., M.F. Staddon, E. Munro, S. Banerjee, and M.L. Gardel. 2020. RhoA mediates epithelial cell shape changes via mechanosensitive endocytosis. *Dev. Cell.* 52:152–166.e5. https://doi.org/10.1016/j.devcel.2019.12.002

Cestra, G., D. Toomre, S. Chang, and P. De Camilli. 2005. The Abl/Arg substrate ArgBP2/nArgBP2 coordinates the function of multiple regulatory mechanisms converging on the actin cytoskeleton. *Proc. Natl. Acad. Sci. USA.* 102:1731–1736. https://doi.org/10.1073/pnas.0409376102

Chang, C.W., and S. Kumar. 2015. Differential contributions of nonmuscle myosin II isoforms and functional domains to stress fiber mechanics. *Sci. Rep.* 5:13736. https://doi.org/10.1038/srep13736

Chen, V.C., X. Li, H. Perreault, and J.I. Nagy. 2006. Interaction of zonula occludens-1 (ZO-1) with alpha-actinin-4: Application of functional proteomics for identification of PDZ domain-associated proteins. *J. Proteome Res.* 5:2123–2134. https://doi.org/10.1021/pr060216l

Clark, A.G., A.L. Miller, E. Vaughan, H.Y. Yu, R. Penkert, and W.M. Bement. 2009. Integration of single and multicellular wound responses. *Curr. Biol.* 19:1389–1395. https://doi.org/10.1016/j.cub.2009.06.044

Danjo, Y., and I.K. Gipson. 1998. Actin "purse string" filaments are anchored by E-cadherin-mediated adherens junctions at the leading edge of the epithelial wound, providing coordinated cell movement. *J. Cell Sci.* 111:3323–3332. https://doi.org/10.1242/jcs.111.22.3323

De La Cruz, E.M., and M.L. Gardel. 2015. Actin mechanics and fragmentation. *J. Biol. Chem.* 290:17137–17144. https://doi.org/10.1074/jbc.R115.636472

Dorfel, M.J., J.K. Westphal, C. Bellmann, S.M. Krug, J. Cording, S. Mittag, R. Tauber, M. Fromm, I.E. Blasig, and O. Huber. 2013. CK2-dependent phosphorylation of occludin regulates the interaction with ZO-proteins and tight junction integrity. *Cell Commun. Signal.* 11:40. https://doi.org/10.1186/1478-811X

Dulyaninova, N.G., and A.R. Bresnick. 2013. The heavy chain has its day: Regulation of myosin-II assembly. *Bioarchitecture.* 3:77–85. https://doi.org/10.4161/bioa.26133

Eckert, J.J., A. McCallum, A. Mears, M.G. Rumsby, I.T. Cameron, and T.P. Fleming. 2005. Relative contribution of cell contact pattern, specific PKC isoforms and gap junctional communication in tight junction assembly in the mouse early embryo. *Dev. Biol.* 288:234–247. https://doi.org/10.1016/j.ydbio.2005.09.037

Ecsedi, P., N. Billington, G. Palfy, G. Gogl, B. Kiss, E. Bulyaki, A. Bodor, J.R. Sellers, and L. Nyitray. 2018. Multiple S100 protein isoforms and C-terminal phosphorylation contribute to the paralog-selective regulation of nonmuscle myosin 2 filaments. *J. Biol. Chem.* 293:14850–14867. https://doi.org/10.1074/jbc.ra118.004277

Efimova, N., and T.M. Svitkina. 2018. Branched actin networks push against each other at adherens junctions to maintain cell–cell adhesion. *J. Cell Biol.* 217:1827–1845. https://doi.org/10.1083/jcb.201708103

Even-Faitelson, L., and S. Ravid. 2006. PAK1 and aPKCzeta regulate myosin II-B phosphorylation: A novel signaling pathway regulating filament assembly. *Mol. Biol. Cell.* 17:2869–2881. https://doi.org/10.1091/mbc.e05-11-1001

Fanning, A.S., C.M. Van Itallie, and J.M. Anderson. 2012. Zonula occludens-1 and -2 regulate apical cell structure and the zonula adherens cytoskeleton in polarized epithelia. *Mol. Biol. Cell.* 23:577–590. https://doi.org/10.1091/mbc.E11-09-0791

Florian, P., T. Schoneberg, J.D. Schulzke, M. Fromm, and A.H. Gitter. 2002. Single-cell epithelial defects close rapidly by an actinomyosin purse string mechanism with functional tight junctions. *J. Physiol.* 545:485–499. https://doi.org/10.1113/jphysiol.2002.031161

Fredriksson-Lidman, K., C.M. Van Itallie, A.J. Tietgens, and J.M. Anderson. 2017. Sorbin and SH3 domain-containing protein 2 (SORBS2) is a component of the acto-myosin ring at the apical junctional complex in epithelial cells. *PLoS One.* 12:e0185448. https://doi.org/10.1371/journal.pone.0185448

Fujiwara, I., D. Vavylonis, and T.D. Pollard. 2007. Polymerization kinetics of ADP- and ADP-Pi-actin determined by fluorescence microscopy. *Proc. Natl. Acad. Sci. USA.* 104:8827–8832. https://doi.org/10.1073/pnas.0702510104

Fujiwara, I., M.E. Zweifel, N. Courtemanche, and T.D. Pollard. 2018. Latrunculin A accelerates actin filament depolymerization in addition to sequestering actin monomers. *Curr. Biol.* 28:3183–3192.e2. https://doi.org/10.1016/j.cub.2018.07.082

Ganguly, C., I.C. Baines, E.D. Korn, and J. Sellers. 1992. Regulation of the actin-activated ATPase and in vitro motility activities of monomeric and filamentous Acanthamoeba myosin II. *J. Biol. Chem.* 267:20900–20904

Gomez, G.A., R.W. McLachlan, and A.S. Yap. 2011. Productive tension: Force-sensing and homeostasis of cell–cell junctions. *Trends Cell Biol.* 21:499–505. https://doi.org/10.1016/j.tcb.2011.05.006

Goodenough, D.A., and J.P. Revel. 1970. A fine structural analysis of intercellular junctions in the mouse liver. *J. Cell Biol.* 45:272–290. https://doi.org/10.1083/jcb.45.2.272

Helfrich, I., A. Schmitz, P. Zigrino, C. Michels, I. Haase, A. le Bivic, M. Leitges, and C.M. Niessen. 2007. Role of aPKC isoforms and their binding partners Par3 and Par6 in epidermal barrier formation. *J. Invest. Dermatol.* 127:782–791. https://doi.org/10.1038/sj.jid.5700621

Heuze, M.L., G.H.N. Sankara Narayana, J. D'Alessandro, V. Cellerin, T. Dang, D.S. Williams, J.C. Van Hest, P. Marcq, R.M. Mege, and B. Ladoux. 2019. Myosin II isoforms play distinct roles in adherens junction biogenesis. *Elife.* 8:e46599. https://doi.org/10.7554/eLife.46599

Hotulainen, P., and P. Lappalainen. 2006. Stress fibers are generated by two distinct actin assembly mechanisms in motile cells. *J. Cell Biol.* 173:383–394. https://doi.org/10.1083/jcb.200511093

Huveneers, S., J. Oldenburg, E. Spanjaard, G. van der Krogt, I. Grigoriev, A. Akhmanova, H. Rehmann, and J. de Rooij. 2012. Vinculin associates with endothelial VE-cadherin junctions to control force-dependent

remodeling. *J. Cell Biol.* 196:641–652. https://doi.org/10.1083/jcb.201108120

Ichikawa, T., M. Kita, T.S. Matsui, A.I. Nagasato, T. Araki, S.H. Chiang, T. Sezaki, Y. Kimura, K. Ueda, S. Deguchi, et al. 2017. Vinexin family (SORBS) proteins play different roles in stiffness-sensing and contractile force generation. *J. Cell Sci.* 130:3517–3531. https://doi.org/10.1242/jcs.200691

Juanes-Garcia, A., J.R. Chapman, R. Aguilar-Cuenca, C. Delgado-Arevalo, J. Hodges, L.A. Whitmore, J. Shabanowitz, D.F. Hunt, A.R. Horwitz, and M. Vicente-Manzanares. 2015. A regulatory motif in nonmuscle myosin II-B regulates its role in migratory front-back polarity. *J. Cell Biol.* 209: 23–32. https://doi.org/10.1083/jcb.201407059

Kannan, N., and V.W. Tang. 2015. Synaptopodin couples epithelial contractility to alpha-actinin-4-dependent junction maturation. *J. Cell Biol.* 211: 407–434. https://doi.org/10.1083/jcb.201412003

Kannan, N., and V.W. Tang. 2018. Myosin-1c promotes E-cadherin tension and force-dependent recruitment of alpha-actinin to the epithelial cell junction. *J. Cell Sci.* 131:jcs211334. https://doi.org/10.1242/jcs.211334

Kassianidou, E., J.H. Hughes, and S. Kumar. 2017. Activation of ROCK and MLCK tunes regional stress fiber formation and mechanics via preferential myosin light chain phosphorylation. *Mol. Biol. Cell.* 28: 3832–3843. https://doi.org/10.1091/mbc.E17-06-0401

Katayama, T., M. Watanabe, H. Tanaka, M. Hino, T. Miyakawa, T. Ohki, L.H. Ye, C. Xie, S. Yoshiyama, A. Nakamura, et al. 2010. Stimulatory effects of arachidonic acid on myosin ATPase activity and contraction of smooth muscle via myosin motor domain. *Am. J. Physiol. Heart Circ. Physiol.* 298:H505–H514. https://doi.org/10.1152/ajpheart.00577.2009

Kiboku, T., T. Katoh, A. Nakamura, A. Kitamura, M. Kinjo, Y. Murakami, and M. Takahashi. 2013. Nonmuscle myosin II folds into a 10S form via two portions of tail for dynamic subcellular localization. *Gene Cell.* 18: 90–109. https://doi.org/10.1111/gtc.12021

Kimori, Y., N. Baba, and E. Katayama. 2013. Novel configuration of a myosin II transient intermediate analogue revealed by quick-freeze deep-etch replica electron microscopy. *Biochem. J.* 450:23–35. https://doi.org/10.1042/BJ20120412

Knudsen, K.A., A.P. Soler, K.R. Johnson, and M.J. Wheelock. 1995. Interaction of alpha-actinin with the cadherin/catenin cell–cell adhesion complex via alpha-catenin. *J. Cell Biol.* 130:67–77. https://doi.org/10.1083/jcb.130.1.67

Kobielak, A., H.A. Pasolli, and E. Fuchs. 2004. Mammalian formin-1 participates in adherens junctions and polymerization of linear actin cables. *Nat. Cell Biol.* 6:21–30. https://doi.org/10.1038/ncb1075

Koenderink, G.H., and E.K. Paluch. 2018. Architecture shapes contractility in actomyosin networks. *Curr. Opin. Cell Biol.* 50:79–85. https://doi.org/10.1016/j.ceb.2018.01.015

Kovacs, M., F. Wang, A. Hu, Y. Zhang, and J.R. Sellers. 2003. Functional divergence of human cytoplasmic myosin II: Kinetic characterization of the non-muscle IIA isoform. *J. Biol. Chem.* 278:38132–38140. https://doi.org/10.1074/jbc.M305453200

Kuipers, D., A. Mehonic, M. Kajita, L. Peter, Y. Fujita, T. Duke, G. Charras, and J.E. Gale. 2014. Epithelial repair is a two-stage process driven first by dying cells and then by their neighbours. *J. Cell Sci.* 127:1229–1241. https://doi.org/10.1242/jcs.138289

Kuragano, M., T.Q.P. Uyeda, K. Kamijo, Y. Murakami, and M. Takahashi. 2018. Different contributions of nonmuscle myosin IIA and IIB to the organization of stress fiber subtypes in fibroblasts. *Mol. Biol. Cell.* 29: 911–922. https://doi.org/10.1091/mbc.e17-04-0215

Law, R., P. Carl, S. Harper, P. Dalhaimer, D.W. Speicher, and D.E. Discher. 2003. Cooperativity in forced unfolding of tandem spectrin repeats. *Biophys. J.* 84:533–544. https://doi.org/10.1016/S0006-3495(03)74872-3

Limouze, J., A.F. Straight, T. Mitchison, and J.R. Sellers. 2004. Specificity of blebbistatin, an inhibitor of myosin II. *J. Muscle Res. Cell Motil.* 25: 337–341. https://doi.org/10.1007/s10974-004-6060-7

Liu, J., D.W. Taylor, and K.A. Taylor. 2004. A 3-D reconstruction of smooth muscle alpha-actinin by CryoEm reveals two different conformations at the actin-binding region. *J. Mol. Biol.* 338:115–125. https://doi.org/10.1016/j.jmb.2004.02.034

Liu, X., N. Billington, S. Shu, S.H. Yu, G. Piszczek, J.R. Sellers, and E.D. Korn. 2017. Effect of ATP and regulatory light-chain phosphorylation on the polymerization of mammalian nonmuscle myosin II. *Proc. Natl. Acad. Sci. USA.* 114:E6516–E6525. https://doi.org/10.1073/pnas.1702375114

Liu, X., S. Shu, N. Billington, C.D. Williamson, S. Yu, H. Brzeska, J.G. Donaldson, J.R. Sellers, and E.D. Korn. 2016. Mammalian nonmuscle myosin II binds to anionic phospholipids with concomitant dissociation of the regulatory light chain. *J. Biol. Chem.* 291:24828–24837. https://doi.org/10.1074/jbc.M116.739185

Liu, X., S. Shu, and E.D. Korn. 2018. Polymerization pathway of mammalian nonmuscle myosin 2s. *Proc. Natl. Acad. Sci. USA.* 115:E7101–E7108. https://doi.org/10.1073/pnas.1808800115

Madara, J.L. 1987. Intestinal absorptive cell tight junctions are linked to cytoskeleton. *Am. J. Physiol.* 253:C171–C175. https://doi.org/10.1152/ajpcell.1987.253.1.C171

Madara, J.L. 1990. Maintenance of the macromolecular barrier at cell extrusion sites in intestinal epithelium: Physiological rearrangement of tight junctions. *J. Membr. Biol.* 116:177–184. https://doi.org/10.1007/BF01868675

Madara, J.L., D. Barenberg, and S. Carlson. 1986. Effects of cytochalasin D on occluding junctions of intestinal absorptive cells: Further evidence that the cytoskeleton may influence paracellular permeability and junctional charge selectivity. *J. Cell Biol.* 102:2125–2136. https://doi.org/10.1083/jcb.102.6.2125

Madara, J.L., J. Stafford, D. Barenberg, and S. Carlson. 1988. Functional coupling of tight junctions and microfilaments in T84 monolayers. *Am. J. Physiol.* 254:G416–G423. https://doi.org/10.1152/ajpgi.1988.254.3.G416

Melli, L., N. Billington, S.A. Sun, J.E. Bird, A. Nagy, T.B. Friedman, Y. Takagi, and J.R. Sellers. 2018. Bipolar filaments of human nonmuscle myosin 2-A and 2-B have distinct motile and mechanical properties. *Elife.* 7: e32871. https://doi.org/10.7554/eLife.32871

Meng, F., and F. Sachs. 2011. Visualizing dynamic cytoplasmic forces with a compliance-matched FRET sensor. *J. Cell Sci.* 124:261–269. https://doi.org/10.1242/jcs.071928

Meng, F., and F. Sachs. 2012. Orientation-based FRET sensor for real-time imaging of cellular forces. *J. Cell Sci.* 125:743–750. https://doi.org/10.1242/jcs.093104

Meyer, R.K., and U. Aebi. 1990. Bundling of actin filaments by alpha-actinin depends on its molecular length. *J. Cell Biol.* 110:2013–2024. https://doi.org/10.1083/jcb.110.6.2013

Milberg, O., A. Shitara, S. Ebrahim, A. Masedunskas, M. Tora, D.T. Tran, Y. Chen, M.A. Conti, R.S. Adelstein, K.G. Ten Hagen, and R. Weigert. 2017. Concerted actions of distinct nonmuscle myosin II isoforms drive intracellular membrane remodeling in live animals. *J. Cell Biol.* 216: 1925–1936. https://doi.org/10.1083/jcb.201612126

Millan, J., R.J. Cain, N. Reglero-Real, C. Bigarella, B. Marcos-Ramiro, L. Fernandez-Martin, I. Correas, and A.J. Ridley. 2010. Adherens junctions connect stress fibres between adjacent endothelial cells. *BMC Biol.* 8:11. https://doi.org/10.1186/1741-7007

Mitchison, T.J. 1992. Compare and contrast actin filaments and microtubules. *Mol. Biol. Cell.* 3:1309–1315. https://doi.org/10.1091/mbc.3.12.1309

Morin, T.R. Jr., S.A. Ghassem-Zadeh, and J. Lee. 2014. Traction force microscopy in rapidly moving cells reveals separate roles for ROCK and MLCK in the mechanics of retraction. *Exp. Cell Res.* 326:280–294. https://doi.org/10.1016/j.yexcr.2014.04.015

Mullins, R.D., J.A. Heuser, and T.D. Pollard. 1998. The interaction of Arp2/3 complex with actin: Nucleation, high affinity pointed end capping, and formation of branching networks of filaments. *Proc. Natl. Acad. Sci. USA.* 95:6181–6186. https://doi.org/10.1073/pnas.95.11.6181

Mundel, P., H.W. Heid, T.M. Mundel, M. Kruger, J. Reiser, and W. Kriz. 1997. Synaptopodin: An actin-associated protein in telencephalic dendrites and renal podocytes. *J. Cell Biol.* 139:193–204. https://doi.org/10.1083/jcb.139.1.193

Murakami, N., V.P. Chauhan, and M. Elzinga. 1998. Two nonmuscle myosin II heavy chain isoforms expressed in rabbit brains: Filament forming properties, the effects of phosphorylation by protein kinase C and casein kinase II, and location of the phosphorylation sites. *Biochemistry.* 37: 1989–2003. https://doi.org/10.1021/bi971959a

Murakami, N., S. Matsumura, and A. Kumon. 1984. Purification and identification of myosin heavy chain kinase from bovine brain. *J. Biochem.* 95: 651–660. https://doi.org/10.1093/oxfordjournals.jbchem.a134654

Murrell, M.P., and M.L. Gardel. 2012. F-actin buckling coordinates contractility and severing in a biomimetic actomyosin cortex. *Proc. Natl. Acad. Sci. USA.* 109:20820–20825. https://doi.org/10.1073/pnas.1214753109

Nagy, A., Y. Takagi, N. Billington, S.A. Sun, D.K. Hong, E. Homsher, A. Wang, and J.R. Sellers. 2013. Kinetic characterization of nonmuscle myosin IIb at the single molecule level. *J. Biol. Chem.* 288:709–722. https://doi.org/10.1074/jbc.M112.424671

Nakanishi, O., S. Suetsugu, D. Yamazaki, and T. Takenawa. 2007. Effect of WAVE2 phosphorylation on activation of the Arp2/3 complex. *J. Biochem.* 141:319–325. https://doi.org/10.1093/jb/mvm034

Naumanen, P., P. Lappalainen, and P. Hotulainen. 2008. Mechanisms of actin stress fibre assembly. *J. Microsc.* 231:446–454. https://doi.org/10.1111/j .1365-2818.2008.02057.x

Ning, L., H.Y. Suleiman, and J.H. Miner. 2020. Synaptopodin is dispensable for normal podocyte homeostasis but is protective in the context of acute podocyte injury. *J. Am. Soc. Nephrol.* 31:2815–2832. https://doi.org/ 10.1681/ASN.2020050572

Ning, L., H.Y. Suleiman, and J.H. Miner. 2021. Synaptopodin deficiency exacerbates kidney disease in a mouse model of Alport syndrome. *Am. J. Physiol. Ren. Physiol.* 321:F12–F25. https://doi.org/10.1152/ajprenal .00035.2021

Norstrom, M.F., P.A. Smithback, and R.S. Rock. 2010. Unconventional processive mechanics of non-muscle myosin IIB. *J. Biol. Chem.* 285: 26326–26334. https://doi.org/10.1074/jbc.M110.123851

Pellegrin, S., and H. Mellor. 2007. Actin stress fibres. *J. Cell Sci.* 120: 3491–3499. https://doi.org/10.1242/jcs.018473

Pinheiro, D., and Y. Bellaïche. 2018. Mechanical force-driven adherens junction remodeling and epithelial dynamics. *Dev. Cell.* 47:3–19. https:// doi.org/10.1016/j.devcel.2018.10.021

Pollard, T.D. 1986. Rate constants for the reactions of ATP- and ADP-actin with the ends of actin filaments. *J. Cell Biol.* 103:2747–2754. https://doi .org/10.1083/jcb.103.6.2747

Pollard, T.D., and G.G. Borisy. 2003. Cellular motility driven by assembly and disassembly of actin filaments. *Cell.* 112:453–465. https://doi.org/10 .1016/s0092-8674(03)00357-x

Raleigh, D.R., D.M. Boe, D. Yu, C.R. Weber, A.M. Marchiando, E.M. Bradford, Y. Wang, L. Wu, E.E. Schneeberger, L. Shen, and J.R. Turner. 2011. Occludin S408 phosphorylation regulates tight junction protein interactions and barrier function. *J. Cell Biol.* 193:565–582. https://doi.org/10 .1083/jcb.201010065

Ramamurthy, B., C.M. Yengo, A.F. Straight, T.J. Mitchison, and H.L. Sweeney. 2004. Kinetic mechanism of blebbistatin inhibition of nonmuscle myosin IIb. *Biochemistry.* 43:14832–14839. https://doi.org/10.1021/ bi0490284

Ridley, A.J., and A. Hall. 1992. The small GTP-binding protein rho regulates the assembly of focal adhesions and actin stress fibers in response to growth factors. *Cell.* 70:389–399. https://doi.org/10.1016/0092-8674(92) 90163-7

Rochman, M., J. Travers, J.P. Abonia, J.M. Caldwell, and M.E. Rothenberg. 2017. Synaptopodin is upregulated by IL-13 in eosinophilic esophagitis and regulates esophageal epithelial cell motility and barrier integrity. *JCI Insight.* 2:96789. https://doi.org/10.1172/jci.insight.96789

Roper, K. 2015. Integration of cell–cell adhesion and contractile actomyosin activity during morphogenesis. *Curr. Top Dev. Biol.* 112:103–127. https:// doi.org/10.1016/bs.ctdb.2014.11.017

Rosenberg, M., R. Straussman, A. Ben-Ya'acov, D. Ronen, and S. Ravid. 2008. MHC-IIB filament assembly and cellular localization are governed by the rod net charge. *PLoS One.* 3:e1496. https://doi.org/10.1371/journal .pone.0001496

Rosenfeld, S.S., J. Xing, L.Q. Chen, and H.L. Sweeney. 2003. Myosin IIb is unconventionally conventional. *J. Biol. Chem.* 278:27449–27455. https:// doi.org/10.1074/jbc.M302555200

Roy, A., L. Lordier, S. Mazzi, Y. Chang, V. Lapierre, J. Larghero, N. Debili, H. Raslova, and W. Vainchenker. 2016. Activity of nonmuscle myosin II isoforms determines localization at the cleavage furrow of megakaryocytes. *Blood.* 128:3137–3145. https://doi.org/10.1182/blood -2016b04-711630

Sandquist, J.C., K.I. Swenson, K.A. Demali, K. Burridge, and A.R. Means. 2006. Rho kinase differentially regulates phosphorylation of nonmuscle myosin II isoforms A and B during cell rounding and migration. *J. Biol. Chem.* 281:35873–35883. https://doi.org/10.1074/jbc.m605343200

Sato, M.K., M. Takahashi, and M. Yazawa. 2007. Two regions of the tail are necessary for the isoform-specific functions of nonmuscle myosin IIB. *Mol. Biol. Cell.* 18:1009–1017. https://doi.org/10.1091/mbc.e06 -08-0706

Schnabel, E., J.M. Anderson, and M.G. Farquhar. 1990. The tight junction protein ZO-1 is concentrated along slit diaphragms of the glomerular epithelium. *J. Cell Biol.* 111:1255–1263. https://doi.org/10.1083/jcb.111.3 .1255

Shutova, M.S., S.B. Asokan, S. Talwar, R.K. Assoian, J.E. Bear, and T.M. Svitkina. 2017. Self-sorting of nonmuscle myosins IIA and IIB polarizes the cytoskeleton and modulates cell motility. *J. Cell Biol.* 216:2877–2889. https://doi.org/10.1083/jcb.201705167

Shutova, M.S., W.A. Spessott, C.G. Giraudo, and T. Svitkina. 2014. Endogenous species of mammalian nonmuscle myosin IIA and IIB include

activated monomers and heteropolymers. *Curr. Biol.* 24:1958–1968. https://doi.org/10.1016/j.cub.2014.07.070

Shutova, M.S., and T.M. Svitkina. 2018. Mammalian nonmuscle myosin II comes in three flavors. *Biochem. Biophys. Res. Commun.* 506:394–402. https://doi.org/10.1016/j.bbrc.2018.03.103

Slayter, H.S., and S. Lowey. 1967. Substructure of the myosin molecule as visualized by electron microscopy. *Proc. Natl. Acad. Sci. USA.* 58: 1611–1618. https://doi.org/10.1073/pnas.58.4.1611

Smutny, M., H.L. Cox, J.M. Leerberg, E.M. Kovacs, M.A. Conti, C. Ferguson, N.A. Hamilton, R.G. Parton, R.S. Adelstein, and A.S. Yap. 2010. Myosin II isoforms identify distinct functional modules that support integrity of the epithelial zonula adherens. *Nat. Cell Biol.* 12:696–702. https://doi .org/10.1038/ncb2072

Solinet, S., and M.L. Vitale. 2008. Isoform B of myosin II heavy chain mediates actomyosin contractility during TNFalpha-induced apoptosis. *J. Cell Sci.* 121:1681–1692. https://doi.org/10.1242/jcs.022640

Stam, S., J. Alberts, M.L. Gardel, and E. Munro. 2015. Isoforms confer characteristic force generation and mechanosensation by myosin II filaments. *Biophys. J.* 108:1997–2006. https://doi.org/10.1016/j.bpj.2015.03 .030

Takahashi, T., C. Fukukawa, C. Naraoka, T. Katoh, and M. Yazawa. 1999. Conformations of vertebrate striated muscle myosin monomers in equilibrium with filaments. *J. Biochem.* 126:34–40. https://doi.org/10 .1093/oxfordjournals.jbchem.a022433

Tamada, M., T.D. Perez, W.J. Nelson, and M.P. Sheetz. 2007. Two distinct modes of myosin assembly and dynamics during epithelial wound closure. *J. Cell Biol.* 176:27–33. https://doi.org/10.1083/jcb.200609116

Tang, V.W.. 2006. Proteomic and bioinformatic analysis of epithelial tight junction reveals an unexpected cluster of synaptic molecules. *Biol. Direct.* 1:37. https://doi.org/10.1186/1745-6150

Tang, V.W., and W.M. Brieher. 2012. α-Actinin-4/FSGS1 is required for Arp2/ 3-dependent actin assembly at the adherens junction.. *J. Cell Biol.* 196: 115–130. https://doi.org/10.1083/jcb.201103116

Tang, V.W., and W.M. Brieher. 2013. FSGS3/CD2AP is a barbed-end capping protein that stabilizes actin and strengthens adherens junctions. *J. Cell Biol.* 203:815–833. https://doi.org/10.1083/jcb.201304044

Tornavaca, O., M. Chia, N. Dufton, L.O. Almagro, D.E. Conway, A.M. Randi, M.A. Schwartz, K. Matter, and M.S. Balda. 2015. ZO-1 controls endothelial adherens junctions, cell–cell tension, angiogenesis, and barrier formation. *J. Cell Biol.* 208:821–838. https://doi.org/10.1083/jcb .201404140

Totsukawa, G., Y. Wu, Y. Sasaki, D.J. Hartshorne, Y. Yamakita, S. Yamashiro, and F. Matsumura. 2004. Distinct roles of MLCK and ROCK in the regulation of membrane protrusions and focal adhesion dynamics during cell migration of fibroblasts. *J. Cell Biol.* 164:427–439. https://doi .org/10.1083/jcb.200306172

Tsukita, S., and S. Tsukita. 1989. Isolation of cell-to-cell adherens junctions from rat liver. *J. Cell Biol.* 108:31–41. https://doi.org/10 .1083/jcb.108.1.31

Twiss, F., Q. Le Duc, S. Van Der Horst, H. Tabdili, G. Van Der Krogt, N. Wang, H. Rehmann, S. Huveneers, D.E. Leckband, and J. De Rooij. 2012. Vinculin-dependent cadherin mechanosensing regulates efficient epithelial barrier formation. *Biol. Open.* 1:1128–1140. https://doi.org/10 .1242/bio.20122428

Uhlen, M., L. Fagerberg, B.M. Hallstrom, C. Lindskog, P. Oksvold, A. Mardinoglu, A. Sivertsson, C. Kampf, E. Sjostedt, A. Asplund, et al. 2015. Proteomics. Tissue-based map of the human proteome. *Science.* 347: 1260419. https://doi.org/10.1126/science.1260419

Van Itallie, C.M., A. Aponte, A.J. Tietgens, M. Gucek, K. Fredriksson, and J.M. Anderson. 2013. The N and C termini of ZO-1 are surrounded by distinct proteins and functional protein networks. *J. Biol. Chem.* 288: 13775–13788. https://doi.org/10.1074/jbc.m113.466193

Verma, S., S.P. Han, M. Michael, G.A. Gomez, Z. Yang, R.D. Teasdale, A. Ratheesh, E.M. Kovacs, R.G. Ali, and A.S. Yap. 2012. A WAVE2-Arp2/3 actin nucleator apparatus supports junctional tension at the epithelial zonula adherens. *Mol. Biol. Cell.* 23:4601–4610. https://doi.org/10.1091/ mbc.e12-08-0574

Vicente-Manzanares, M., X. Ma, R.S. Adelstein, and A.R. Horwitz. 2009. Nonmuscle myosin II takes centre stage in cell adhesion and migration. *Nat. Rev. Mol. Cell Biol.* 10:778–790. https://doi.org/10.1038/nrm2786

Wang, R.X., J.S. Lee, E.L. Campbell, and S.P. Colgan. 2020. Microbiotaderived butyrate dynamically regulates intestinal homeostasis through regulation of actin-associated protein synaptopodin. *Proc. Natl. Acad. Sci. USA.* 117:11648–11657. https://doi.org/10.1073/pnas .1917597117

Morris et al.
Synaptopodin stress fiber and contractomere at the epithelial junction

Journal of Cell Biology
31 of 32
https://doi.org/10.1083/jcb.202011162

Wood, W., A. Jacinto, R. Grose, S. Woolner, J. Gale, C. Wilson, and P. Martin. 2002. Wound healing recapitulates morphogenesis in Drosophila embryos. *Nat. Cell Biol.* 4:907–912. https://doi.org/10.1038/ncb875

Wu, S.K., S. Budnar, A.S. Yap, and G.A. Gomez. 2014. Pulsatile contractility of actomyosin networks organizes the cellular cortex at lateral cadherin junctions. *Eur. J. Cell Biol.* 93:396–404. https://doi.org/10.1016/j.ejcb.2014.09.001

Zhang, J., M. Betson, J. Erasmus, K. Zeikos, M. Bailly, L.P. Cramer, and V.M. Braga. 2005. Actin at cell–cell junctions is composed of two dynamic and functional populations. *J. Cell Sci.* 118:5549–5562. https://doi.org/10.1242/jcs.02639

Zsolnay, V., H.H. Katkar, S.Z. Chou, T.D. Pollard, and G.A. Voth. 2020. Structural basis for polarized elongation of actin filaments. *Proc. Natl. Acad. Sci. USA.* 117:30458–30464. https://doi.org/10.1073/pnas.2011128117

Supplemental material

A

ISOFORM	Protein EXPRESSION
X1	T84, Podocyte
A	MDCK, HUVEC, Podocyte, C2bbE1
B	Brain membrane, kidney extract
C	Kidney extract
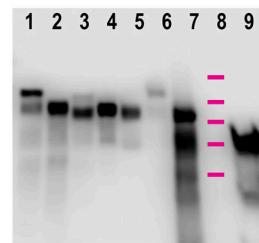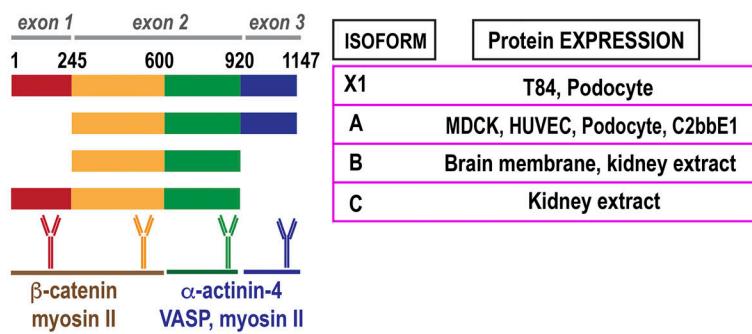
(1) MDCK expressing isoform X1,
(2) MDCK,(3) Podocyte, (4) HUVEC,
(5) C2bbE1, (6) T84, (7) rat kidney,
(8) MW 250, 150, 100, 75, 50 kD,
(9) bovine brain membranes.

B
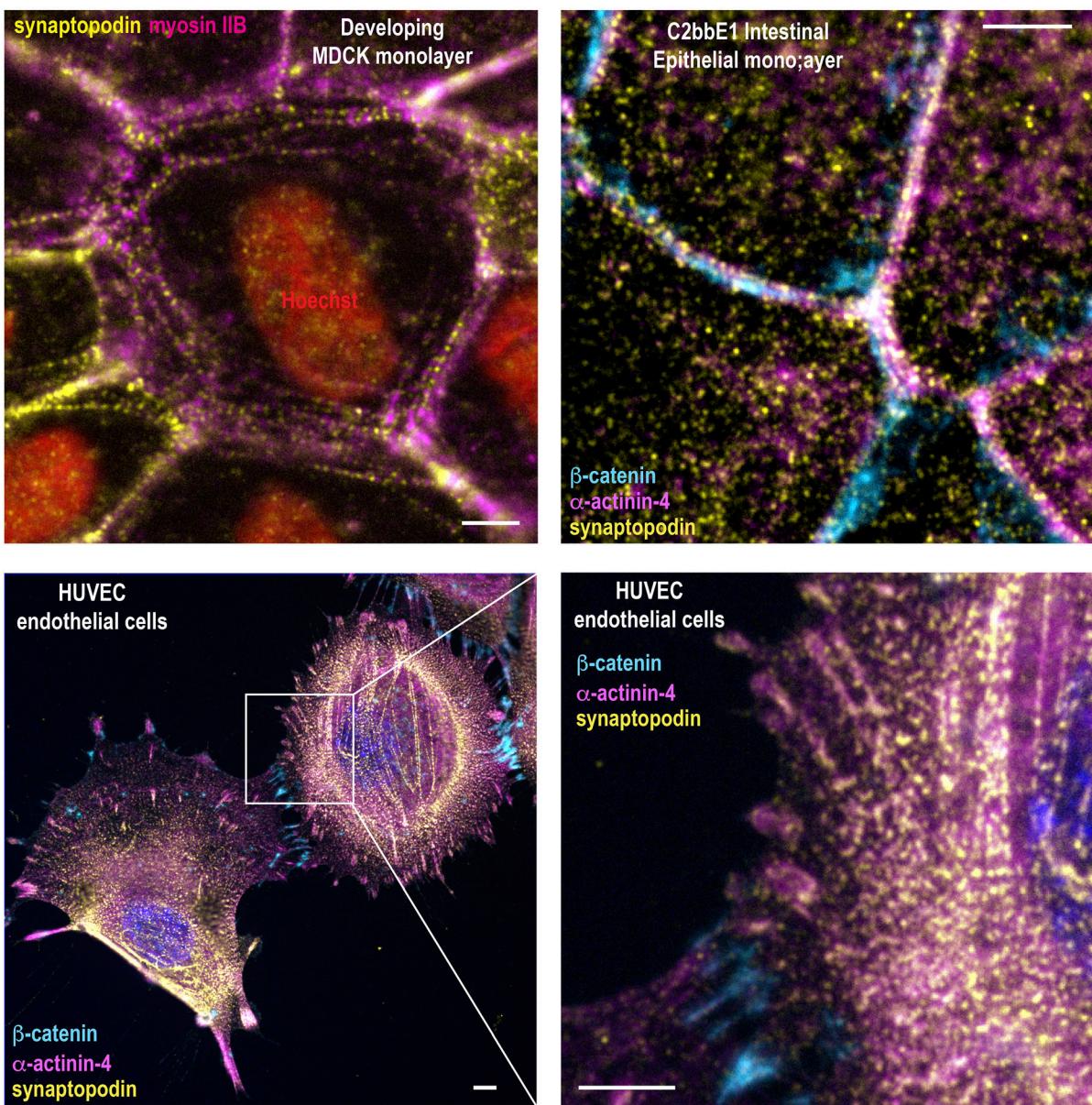
Figure S1.   **Synaptopodin is localized to junctions and stress fibers of epithelial and endothelial cells. (A)** Synaptopodin is encoded by three exons, resulting in four splice variants. We have raised antibodies to each spliced region to characterize the expression of synaptopodin isoforms in mammalian tissues and cells. Western blot of cell lysates using antibodies against region encoded by exon 2, thus recognizing all synaptopodin isoforms. Table summarizes result from Western blot using our newly generated antibodies (see Materials and methods). **(B)** Immunofluorescence of MDCK kidney tubule epithelial cells, C2bbE2 intestinal epithelial cells, HUVEC endothelial cells. Scale bars are 2 μm.
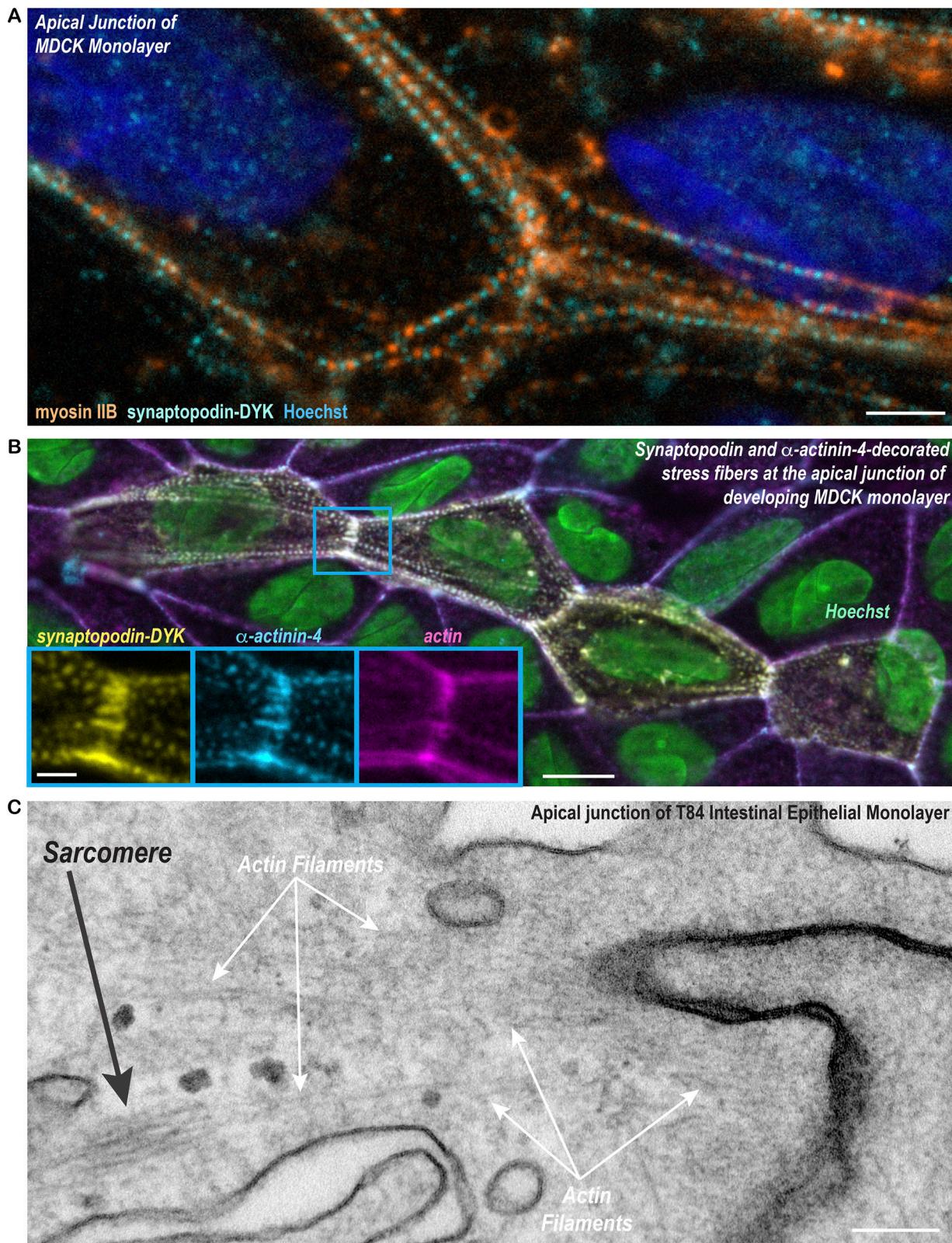
Figure S2. **Apical stress fibers insert at the apical junctions of epithelial cells. (A)** Immunofluorescence showing alternating arrangement of synaptopodin and myosin IIB forming sarcomere-like repeats. Scale bar is 2 µm. **(B)** Immunofluorescence showing apical stress fibers inserted at cell–cell adhesions to connect multiple cells. Insets show colocalization of synaptopodin and α-actinin-4 on apical stress fibers. Scale bar is 5 µm. Inset scale bar is 1 µm. **(C)** Thin-section transmission electron microscopy showing actin bundle connected to the apical junction on one end and a sarcomere-like structure on the opposite end. Scale bar is 200 nm.

Morris et al.
Synaptopodin stress fiber and contractomere at the epithelial junction

Journal of Cell Biology   S3
https://doi.org/10.1083/jcb.202011162
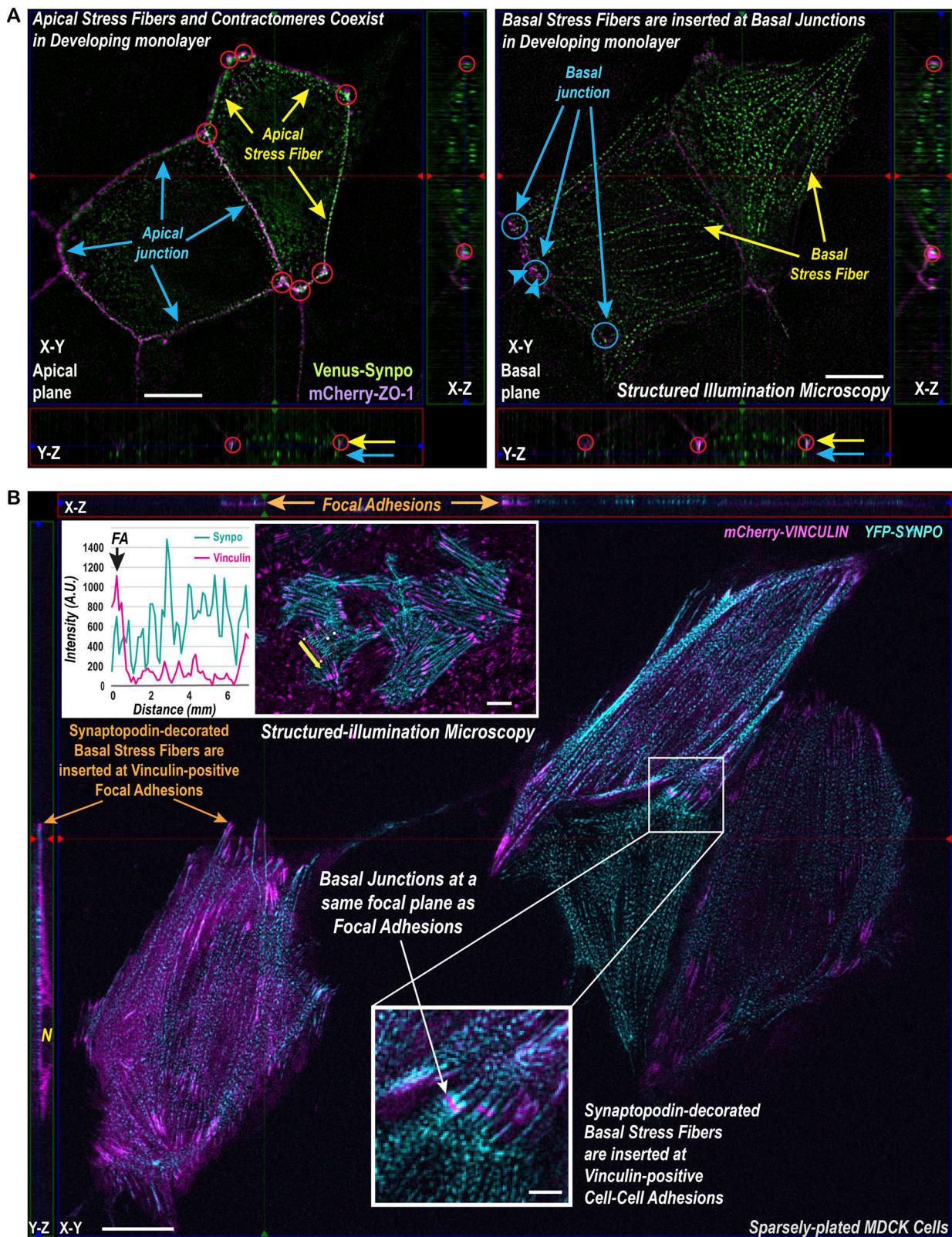
Figure S3. **Vinculin marks basal junctions whereas ZO-1 marks both apical and basal junctions. (A)** Structured-illumination microscopy of synaptopodin and ZO-1. A z-stack is shown in X-Y, Y-Z, and X-Y axes. Left panel shows apical stress fibers and contractomeres on the apical plane. Right panel shows basal stress fibers inserted at basal junctions. Attachment sites for synaptopodin apical stress fibers are circled. Arrows on Y-Z axis point to apical and basal planes. Scale bar is 5 µm. **(B)** Live-cell structured-illumination microscopy of synaptopodin and vinculin. Vinculin marks the basal junction where basal stress fibers are inserted. Inset shows synaptopodin stress fibers inserted at vinculin-decorated focal adhesions. Graph shows a line scan of the yellow arrow along a basal stress fiber (inset). Synaptopodin has periodic organization at the stress fiber. Scale bar is 5 µm. Inset scale bar is 1 µm.
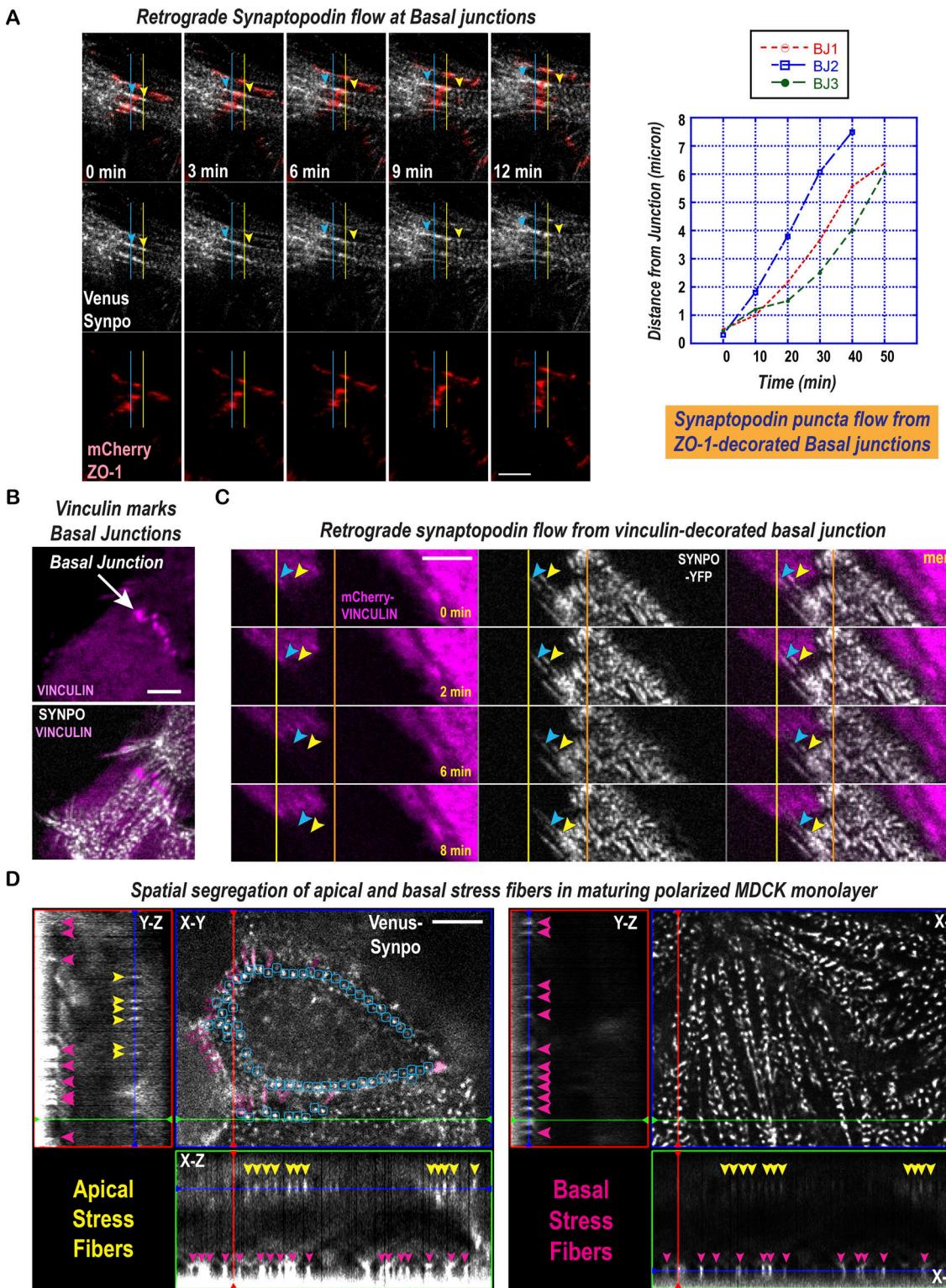
Figure S4. **Retrograde synaptopodin flow from basal junctions. (A)** Frames taken from a time-lapse of synaptopodin and ZO-1. Synaptopodin retrograde flow on opposite sides of basal junctions. Arrowheads track the flow of synaptopodin puncta in two cells. Graph shows rate of retrograde flow by tracking synaptopodin puncta. Scale bar is 1 µm. **(B)** Structured-illumination live-microscopy of synaptopodin and vinculin showing insertion of stress fibers from two cells at basal junctions. Scale bar is 2 µm. **(C)** Frames taken from time-lapse of synaptopodin and vinculin. One cell is expressing synaptopodin, showing retrograde synaptopodin flow from basal junctions marked by the neighboring cell. Arrowheads track the flow of synaptopodin puncta. Scale bar is 1 µm. **(D)** Live imaging of synaptopodin. Left panel shows the apical plane and right panel shows the basal plane of the cell; X-Y, Y-Z, and X-Z views are shown. Synaptopodin linkers at the apical junction is highlighted in purple. The repeated and aligned synaptopodin densities are circled in blue. Yellow arrowheads mark synaptopodin at apical stress fibers in X-Z and Y-Z views. Pink arrowheads mark synaptopodin at basal stress fibers in Y-Z view. The periodic spacing of synaptopodin densities are seen in both apical and basal stress fibers. Scale bar is 2 µm.

A

Retrograde flow of synaptopodin originates from the apical junction in developing monolayer
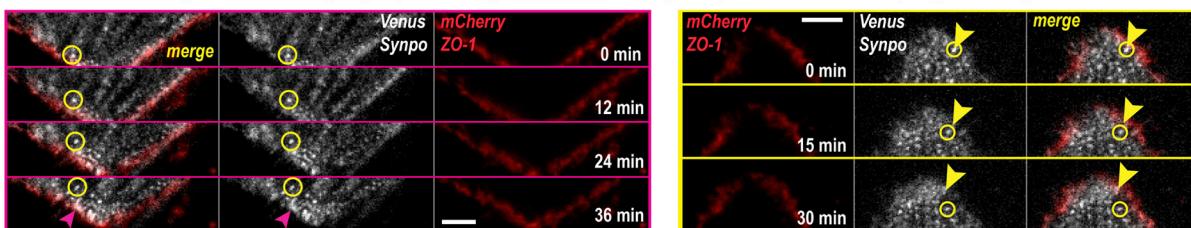
B

Clustering of junctional complexes during contractions of stress fibers
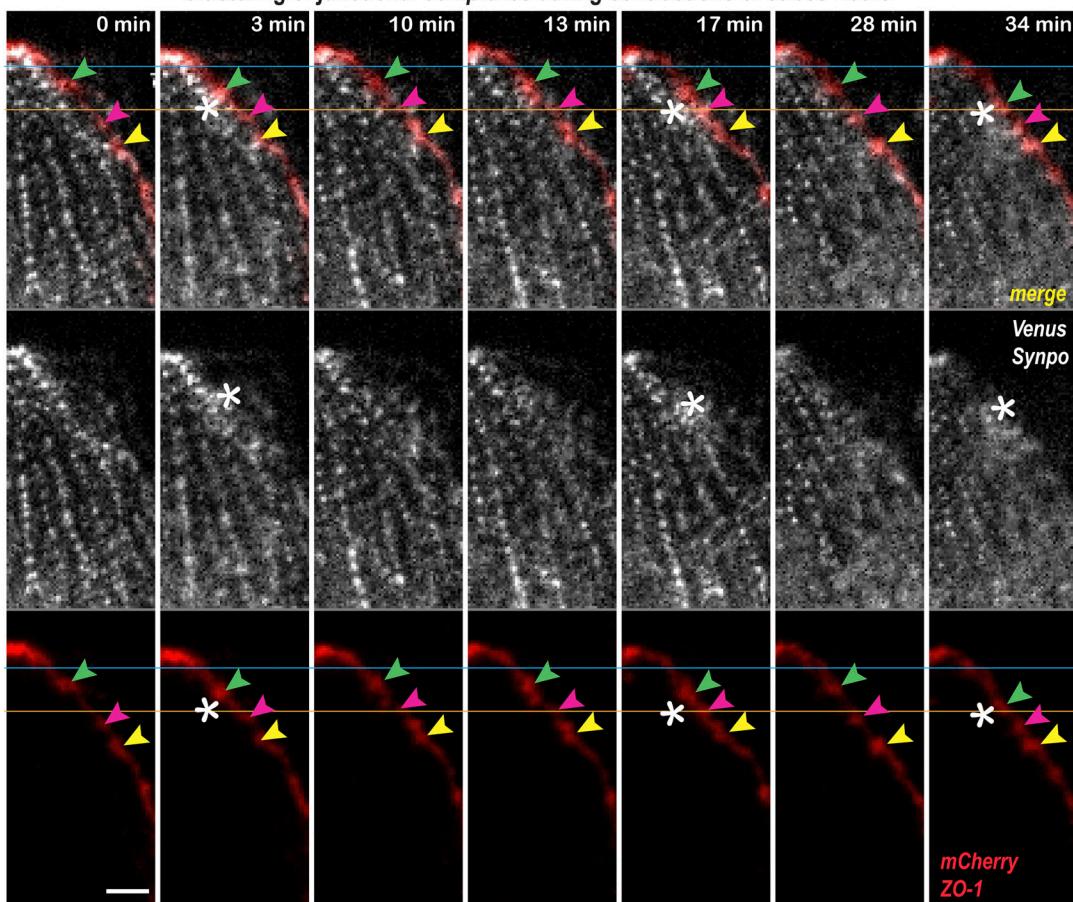
C

Anterograde synaptopodin flow of apical stress fiber translocates junction vertex in maturing monolayer
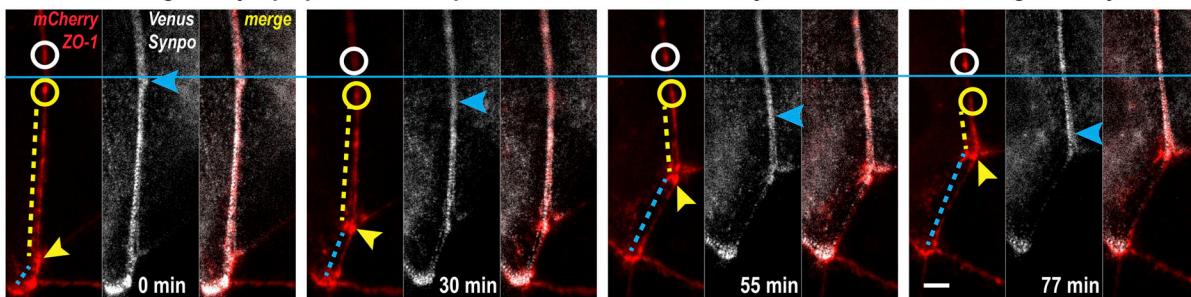
Figure S5.   **Live imaging of synaptopodin showing retrograde flow during early development, contraction during maturation, and anterograde flow towards junctional vertex during late stage of maturation. (A)** Frames from time-lapse of synaptopodin and ZO-1 in cells with developing junctions. Retrograde synaptopodin flow originated from the apical junction. Circles track single synaptopodin densities as they flow inwardly from the apical junction into the medial-apical region. Arrowhead marks the site of synaptopodin puncta origin at the junction. Scale bars are 1 µm. **(B)** Frames from time-lapse of synaptopodin and ZO-1 in cells with maturing junctions. ZO-1 densities, marked by arrowheads, are temporarily clustered when synaptopodin stress fiber contract (asterisk). Scale bar is 1 µm. **(C)** Frames from time-lapse of synaptopodin and ZO-1. Anterograde synaptopodin flow towards junctional vertex is associated with the movement of vertex into the synaptopodin flow. Circles track synaptopodin densities flowing into the junctional vertex. Arrowheads track the movement of the vertex. Scale bar is 2 µm.
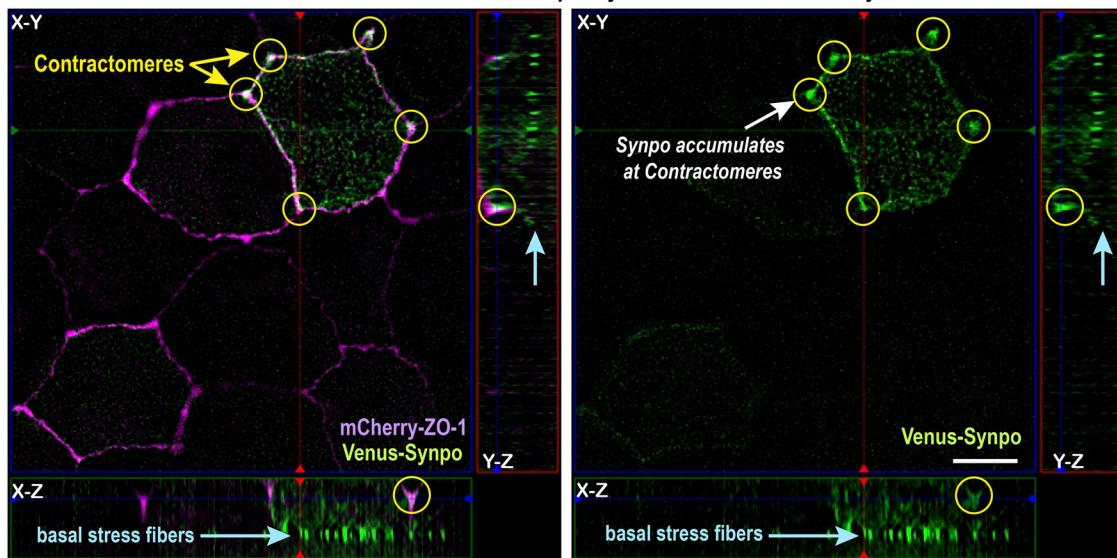
Morris et al.
Synaptopodin stress fiber and contractomere at the epithelial junction

Journal of Cell Biology   S6
https://doi.org/10.1083/jcb.202011162
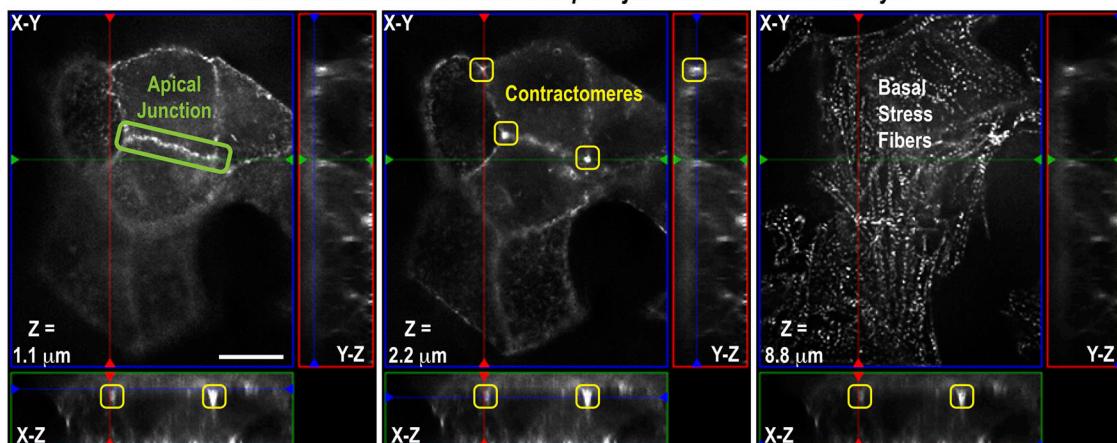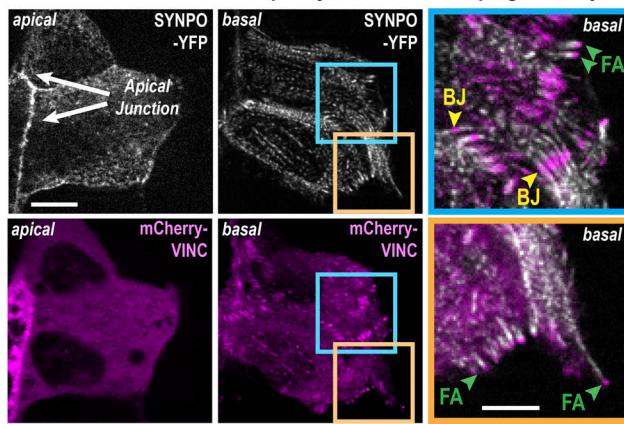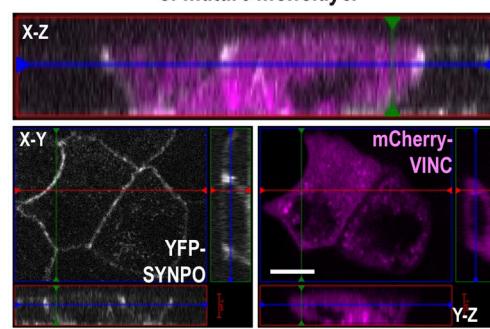
Figure S6. **Contractomere formation at a late stage of junction maturation. (A)** Structured-illumination microscopy of synaptopodin and ZO-1. A z-stack is shown in X-Y, Y-Z, and X-Y axes. Left panel shows contractomeres on the apical plane. Right panel shows basal stress fibers. Arrows on Y-Z axis point to the basal plane. Scale bar is 5 µm. **(B)** Disintegration of periodic synaptopodin organization and the formation of contractomeres at the apical junction in mature monolayer. Left panels show the apical junction and contractomeres on the apical planes. Right panel shows basal stress fibers on the basal plane. X-Y, Y-Z, and X-Z views are shown. Basal stress fibers remain intact despite disassembly of apical stress fibers. Contractomeres are squared in yellow. Scale bar is 5 µm. **(C)** Live-cell structured-illuminated microscopy of synaptopodin and vinculin. Vinculin is absent from the apical junction in developing monolayer. Blue and orange boxes are higher magnification showing basal junctions and focal adhesions on the same basal focal plane. Scale bars are 2 µm. **(D)** Vinculin is absent from the apical junction in mature monolayer. A z-stack is shown in X-Y, X-Z, and Y-Z views. Scale bar is 5 µm.

Morris et al.
Synaptopodin stress fiber and contractomere at the epithelial junction

Journal of Cell Biology   S7
https://doi.org/10.1083/jcb.202011162
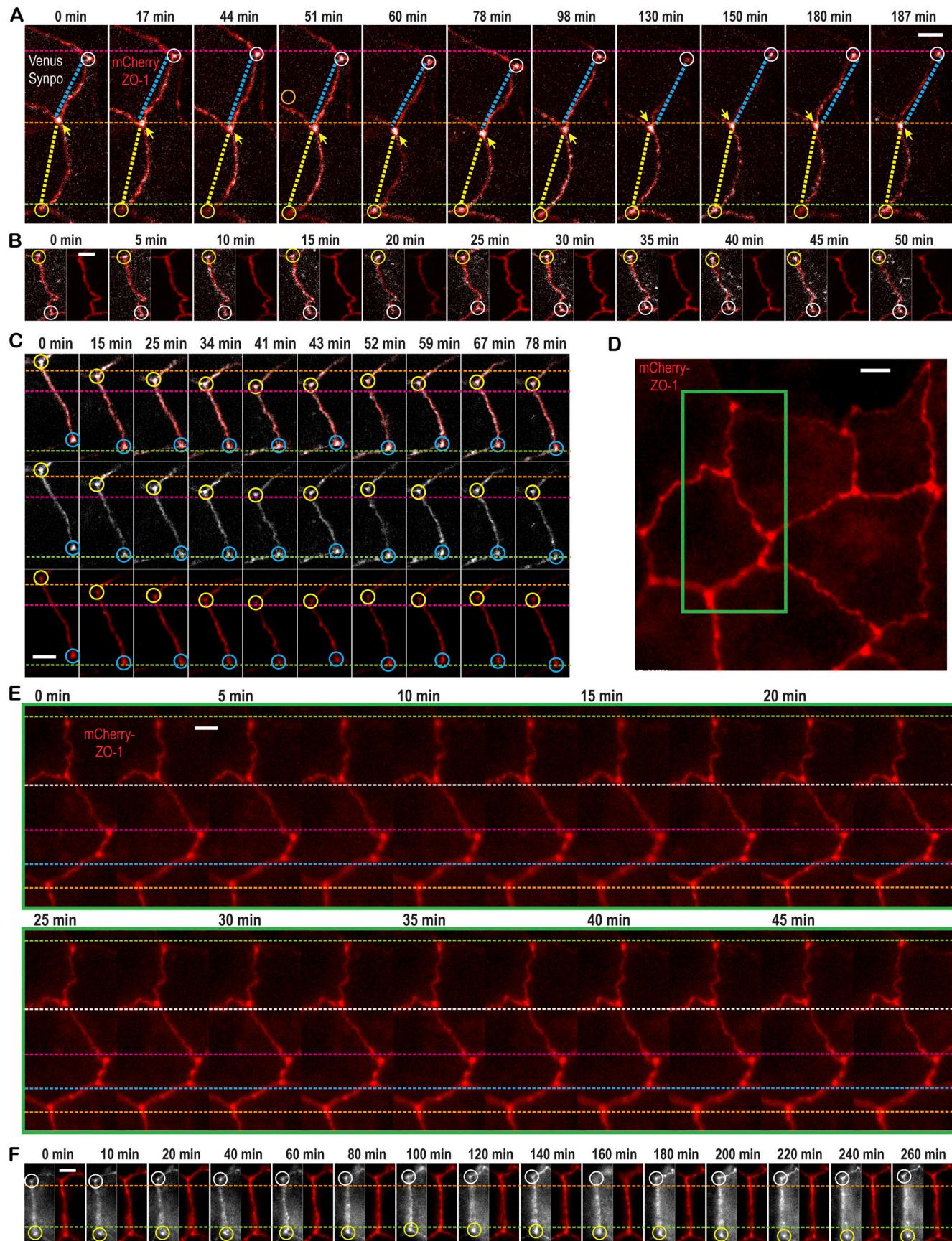
Figure S7. **Contractomeres are stationary in mature monolayer. (A–F)** Frames from time-lapse of synaptopodin and ZO-1 showing oscillation of contractomeres with no net motility or change in junctional lengths. Scale bars are 1 μm.

Morris et al.
Synaptopodin stress fiber and contractomere at the epithelial junction

Journal of Cell Biology   S8
https://doi.org/10.1083/jcb.202011162
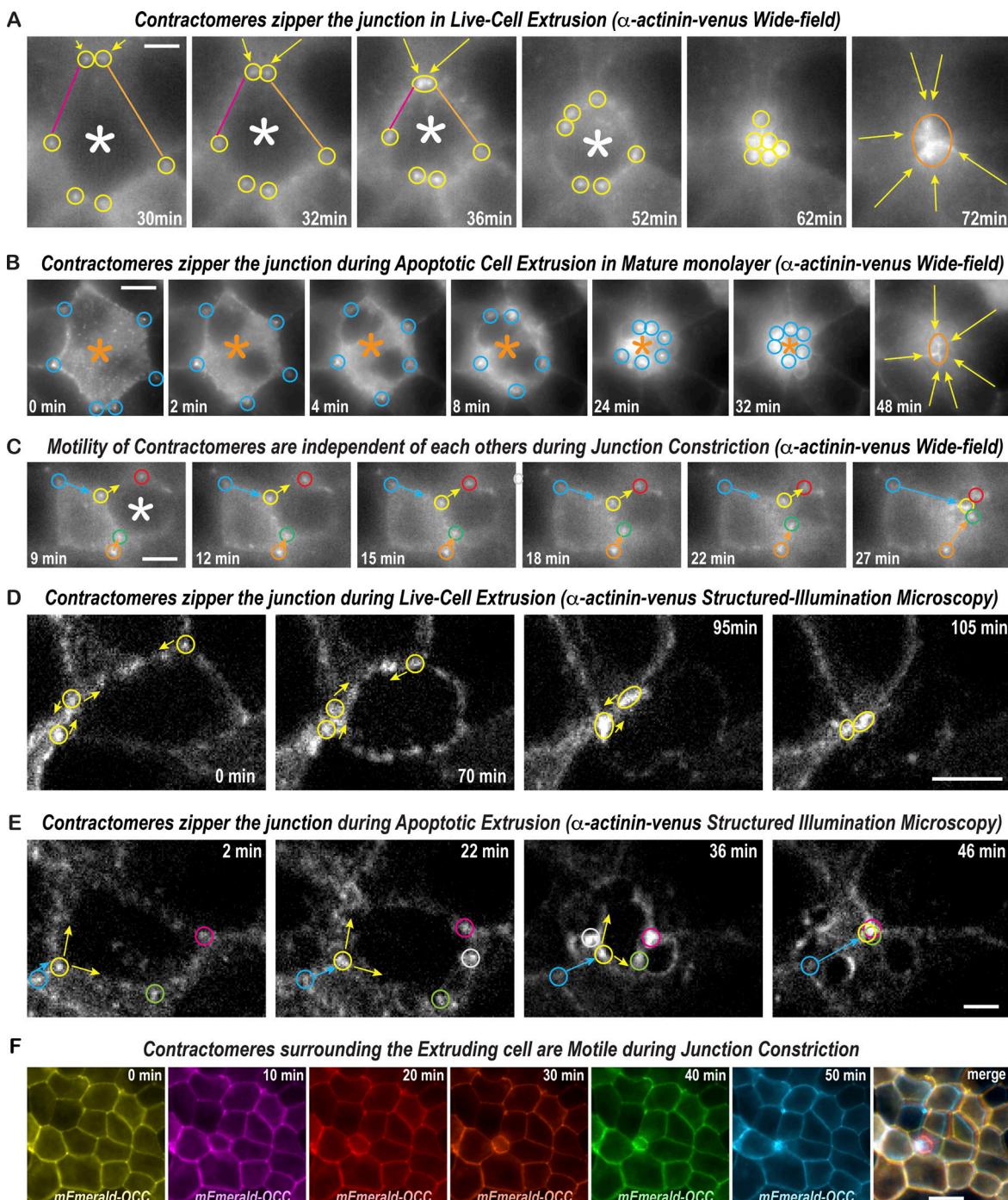
Figure S8. **Contractomeres move during cell extrusion in mature monolayer. (A)** Frames from time-lapse of α-actinin-venus showing contractomeres (yellow circles) glide towards each other to constrict the apical junction during live-cell extrusion (white asterisk). Yellow arrows mark the paths of contractomere movements. Pink and orange lines show shortening of junctions surrounding the extruding cell. Orange circle shows the location of contractomeres after junction constriction is completed. Scale bar is 2 μm. **(B)** Frames from time-lapse of α-actinin-venus showing contractomeres (blue circles) glide towards each other to constrict the apical junction during apoptotic cell extrusion (orange asterisk). Yellow arrows mark the paths of contractomere movements. Orange circle shows the location of contractomeres after constrictions is completed. Scale bar is 10 μm. **(C)** Frames from time-lapse of α-actinin-venus showing contractomeres gliding around the extruding cell (white asterisk). Contractomeres circled in blue and orange are immobile while contractomeres next to the extruding cell (circled in yellow, green, and red) are mobile. Movements of contractomeres next to the extruding cell (yellow, red, green circled) shorten the apical junction surrounding the extruding cell (white asterisk) and lengthen the apical junction in the neighboring cells (blue and orange arrows). Scale bar is 5 μm. **(D)** Frames from time-lapse structured-illumination microscopy of α-actinin-venus showing gliding of contractomeres (circles) to constrict the apical junction (white asterisk). Scale bar is 5 μm. **(E)** Frames from structured-illumination microscopy of α-actinin-venus showing gliding of contractomeres (circles) to shorten the junction next to the extruding cell (yellow arrows) while lengthen the junction in a neighboring cell (blue arrow). Scale bar is 2 μm. **(F)** Frames from time-lapse movie of α-actinin-venus showing a cell extrusion event. Merge image shows overlapping junctions except the ones immediately surrounding the extruding cells. Scale bar is 10 μm.
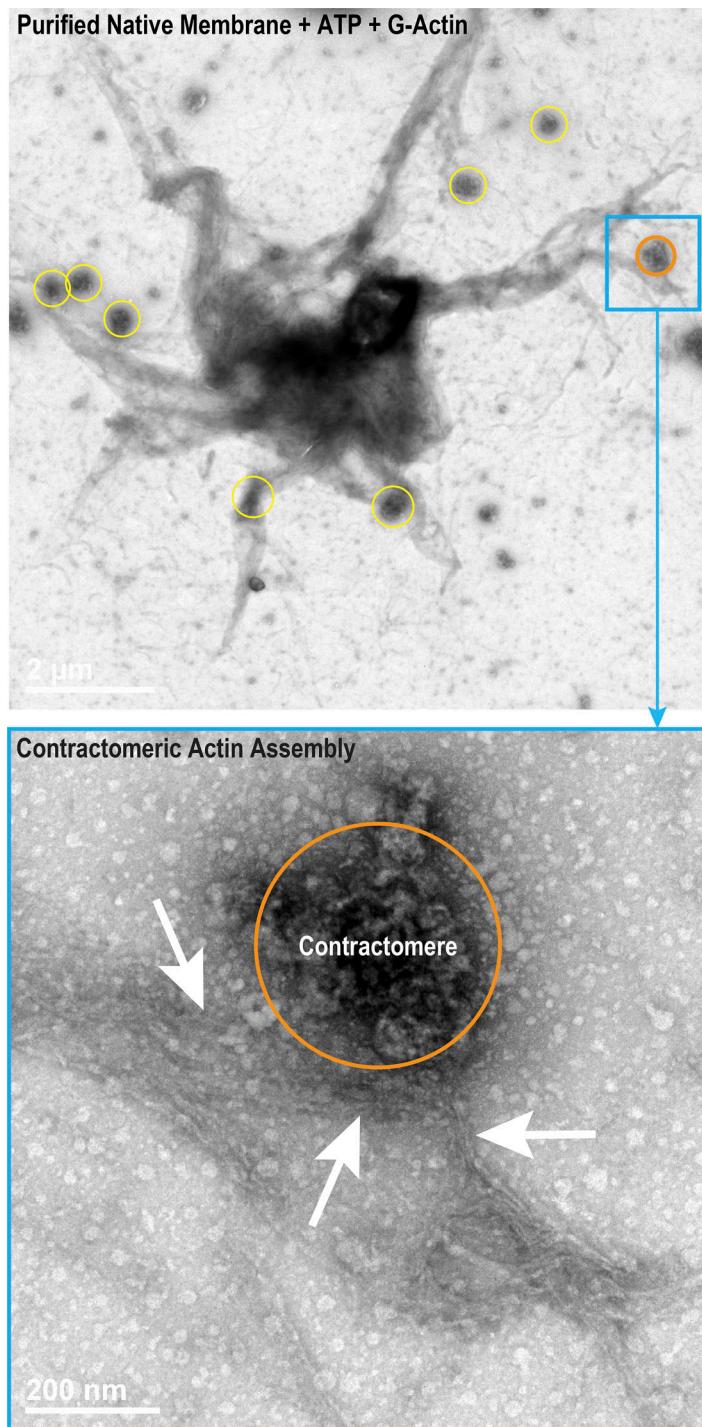
Purified Native Membrane + ATP + G-Actin

2 µm

Contractomeric Actin Assembly

Contractomere

200 nm

Figure S9. **Negative stain EM shows actin assembly at the contractomere.** Negative-stain electron microscopy of an actin assembly reaction (see Methods). Upper panel shows a membrane sheet containing contractomeres (circled) densely decorated with actin filaments. Lower panel shows an enlarge contractomere (circled) with attached actin bundles (arrows). An enlarged contractomere wrapped in actin is shown in Fig. S11 where the top panel is shown again illustrating the area of enlargement. Scale bars are 2 µm for the upper panel and 200 nm for the lower panel.

Morris et al.
Synaptopodin stress fiber and contractomere at the epithelial junction

Journal of Cell Biology   S10
https://doi.org/10.1083/jcb.202011162

Purified Native Membrane + ATP + G-Actin
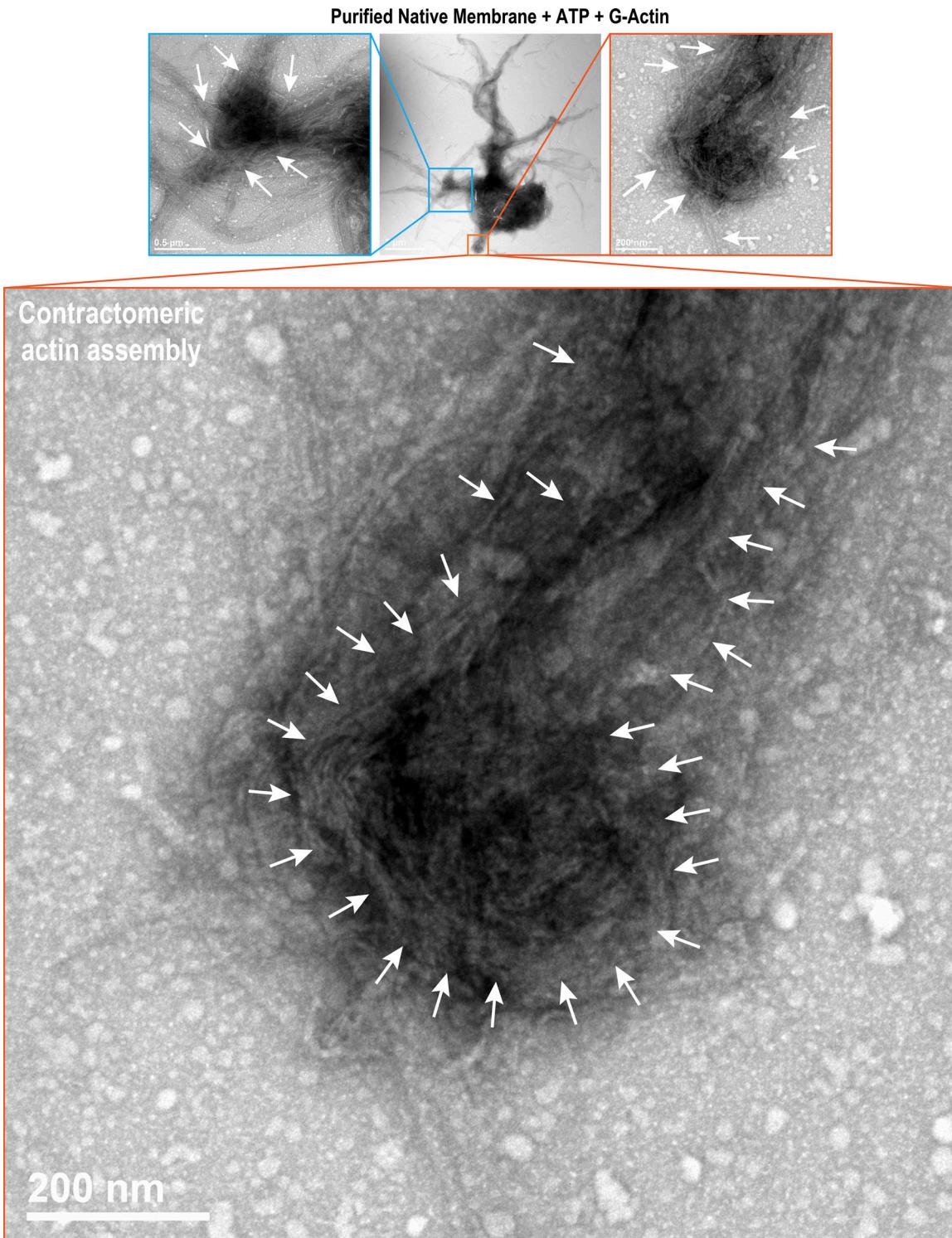
Figure S10. **Negative stain EM shows actin filaments buckling at the contractomere to generate an actin ball.** Negative-stain electron microscopy of an actin assembly reaction (see Methods). Upper middle panel show a membrane sheet containing contractomeres (squared) densely decorated with actin filaments. Lower, upper left, and upper right panels show contractomeres with buckled actin bundles (arrows) rolled into "balls". Scale bars are 2 µm for the upper middle panel, 500 nm for the upper left panel, and 200 nm for the upper right and lower panels.
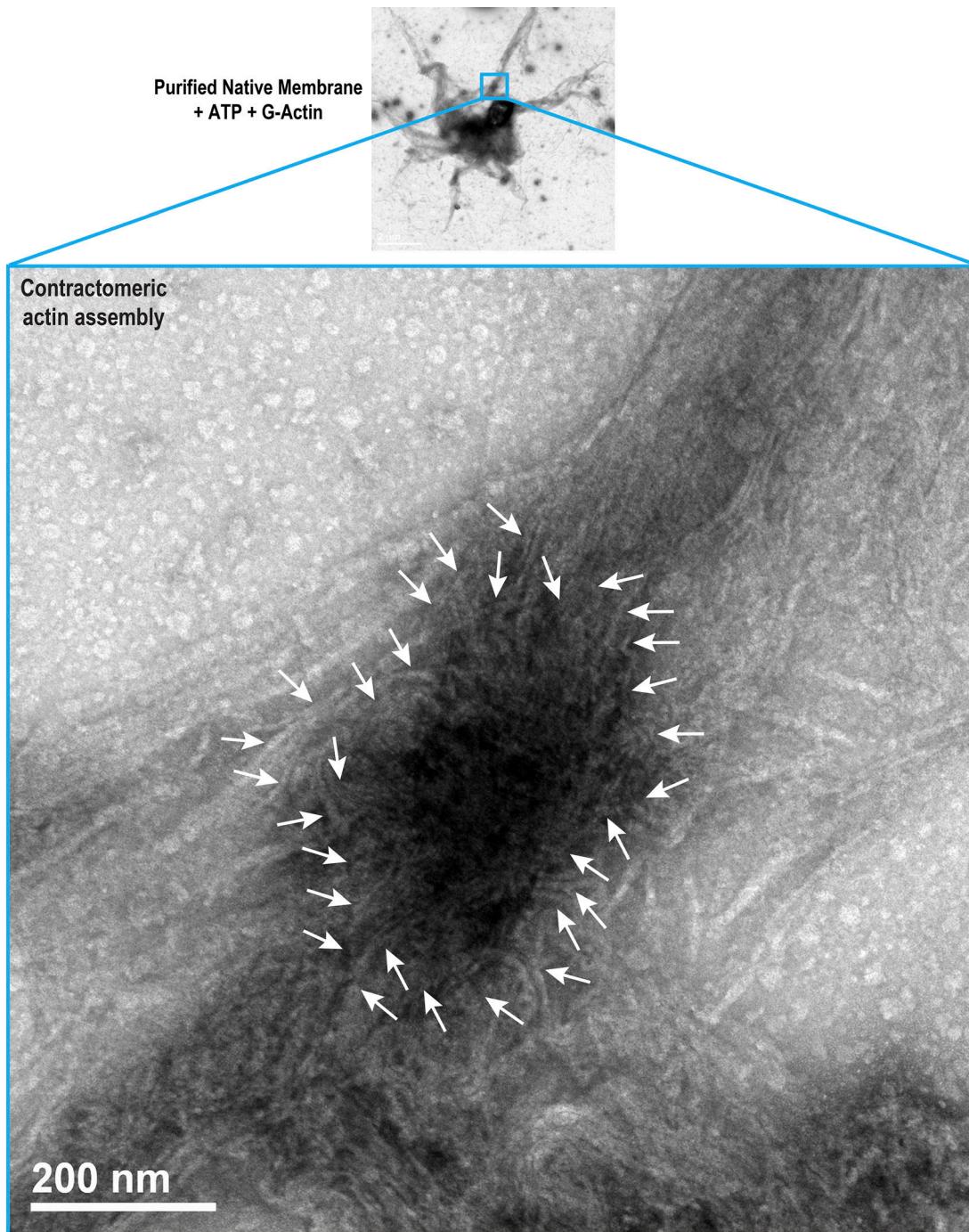
Figure S11.   **Negative stain EM shows actin filaments buckling at the contractomere to generate an actin ball.** Negative-stain electron microscopy of an actin assembly reaction (see Materials and methods). Upper panel shows a membrane sheet containing contractomeres (squared) densely decorated with actin filaments. Lower panel shows an enlarge contractomere with buckled actin bundles (arrows) rolled into a ball. An enlarged contractomere from the top panel is shown in Fig. S9 where the top panel is shown again illustrating the area of enlargement. Scale bars are 2 µm for the upper panel and 200 nm for the lower panel.
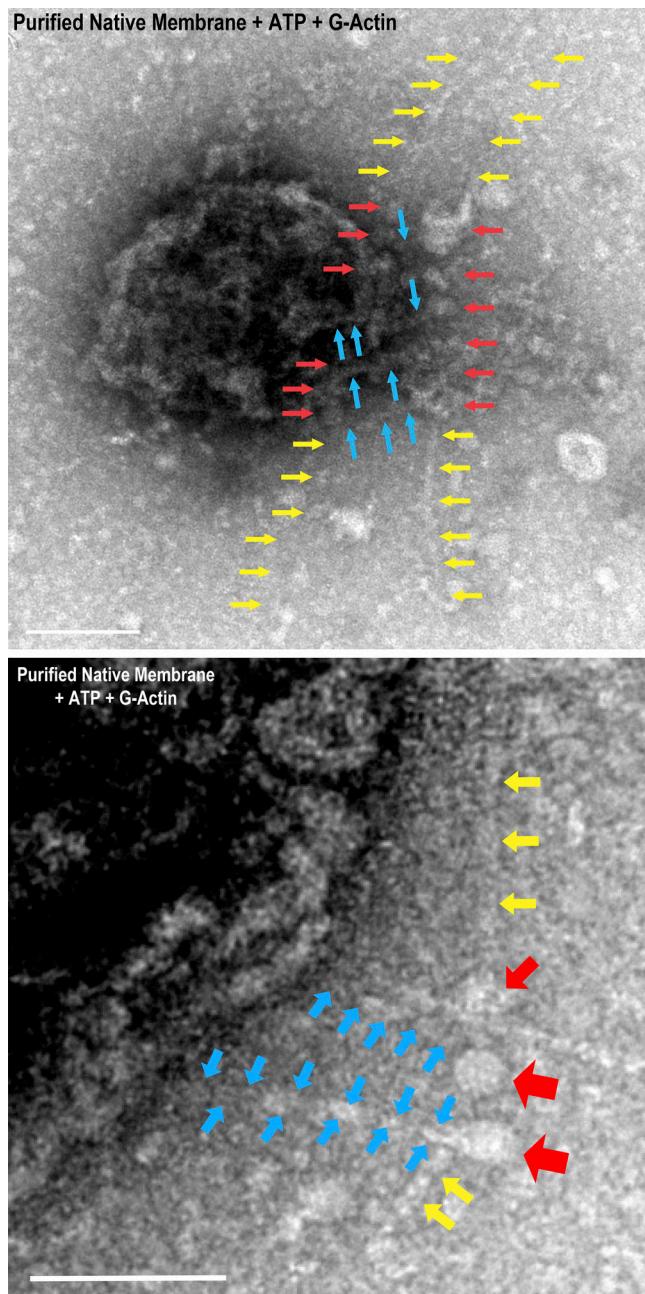
Figure S12. **Negative stain EM shows actin filaments buckling at the contractomere to generate an actin ball.** Negative-stain electron microscopy showing contractomere interacting with actin filaments (yellow arrows) via multiple electron densities (red arrows). Upper panel shows two rows of electron dense globular masses (red arrows) extending via linkers (blue arrows) from the contractomere to interact with actin filaments (yellow arrows). Lower panel is an enlarge image from Fig. 7 B showing interaction of actin filament (yellow arrows) with contractomere via multiple densities (red arrows) including a myosin-like coiled-coil linker extending from the membrane (blue arrows) and pear-shape myosin-like motor heads (red arrows). Scale bars are 100 nm.

Morris et al.
Synaptopodin stress fiber and contractomere at the epithelial junction

Journal of Cell Biology   S13
https://doi.org/10.1083/jcb.202011162

A Junction-enriched purified membrane

↓

High-salt (HS) Extraction

↓

Purify HS-stripped membranes by spinning through 20% sucrose cushion

↓

Add recombinant alpha-actinin-4-sstFRET522

↓ prebind 1 hour

Purify bound fraction + membranes by spinning through 20% sucrose cushion

↓

Actin Assembly Assay Red G-actin +ATP

α-actinin-4-sstFRET522 | Actin | Membranes (Phase Contrast)

α-actinin-4 -stFRET522 / Actin / Merge

Merge / Actin / Membranes (Phase Contrast)

B CFP & YFP Images of cells expressing α-actinin-4 containing either cerulean (CFP) or venus (YFP) inserted between aa 522 & aa 523 (same site as α-actinin-4-sstFRET522)

α4cfp + α4venus Expressing Cells

CFP | YFP | Merge

C Ratio of Excited Emission (FRET) to CFP in cells co-expressing α-actinin-4 containing cerulean (CFP) or venus (YFP) inserted between aa 522 & aa 523 (same site as α-actinin-4-sstFRET522)

α4cfp + α4venus Co-Expressing Cells

CFP | YFP | Merge

FRET/CFP (normalized to cytoplasmic pool)
Cytoplasm / Junction / Contractomere

Figure S13. **New α-actinin-4-sstFRET522 force sensor targets to contractomeres and supports actin assembly. (A)** Reconstitution actin assembly assay using stripped membranes and recombinant α-actinin-4-sstFRET522 (see Methods). Upper right image shows targeting of α-actinin-4-sstFRET522 to contractomeres on stripped membranes. Upper middle image shows actin assembly on contractomeres. Right images show membrane fragments under phase contrast microscopy. Lower middle image shows overlapping α-actinin-4-sstFRET522 and actin (circled). Scale bar is 2 µm. **(B)** Expression of α-actinin-4-CFP and α-actinin-4-venus, with CFP or venus inserted at the same internal site as α-actinin-4-sstFRET522 (see Method) in MDCK cells. Scale bar is 5 µm. **(C)** FRET between α-actinin-4-CFP and α-actinin-4-venus did not show difference between cytoplasm, junction, and contractomere. Wilcoxon-Mann-Whitney test P > 0.1 between cytoplasm (n = 16), junction (n = 8), and contractomere (n = 8). Scale bar is 5 µm.
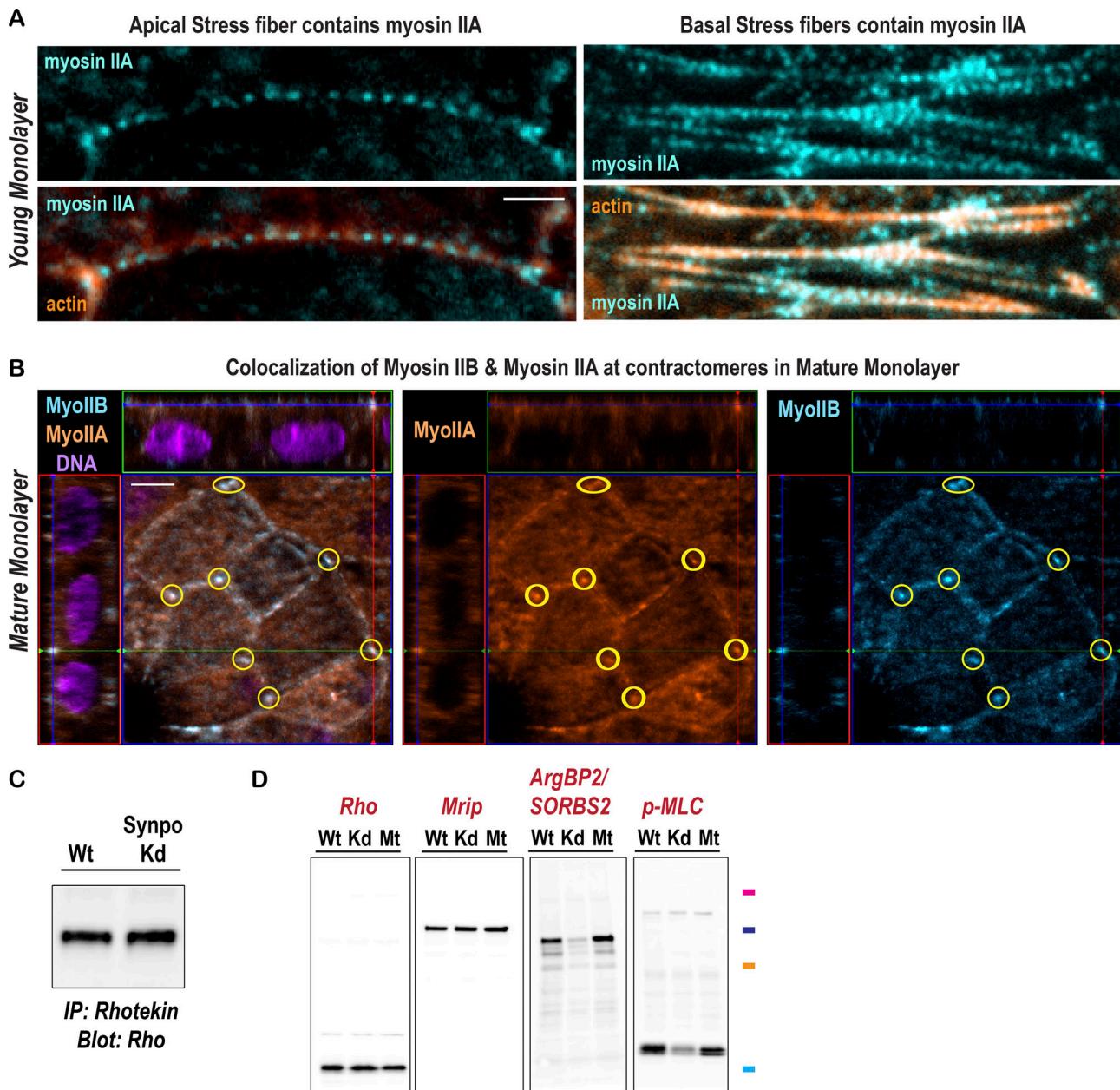
Figure S14. Synaptopodin knockdown does not affect RhoA. (A) Myosin IIA decorates apical and basal stress fibers in developing MDCK monolayer. Scale bar is 2 µm. **(B)** Myosin IIA colocalizes with myosin IIB at the contractomere in mature monolayer. Contractomeres are circled. Scale bar is 5 µm. **(C)** Synaptopodin knockdown does not affect RhoA activity in MDCK cells as assessed by Rhotekin pull-down and RhoA Western blot (see Materials and methods). **(D)** Western blots showing decreased ArgBP1/SORBS2 and phospho-myosin light chain levels in synaptopodin knockdown cells whereas RhoA and MRIP levels were unaffected. Markers are 100, 75, 50, and 25 kD.

Video 1. Live-cell time-lapse of Venus-synaptopodin and mCherry-ZO-1 showing contractions of apical stress fibers concomitant with junction remodeling.

Video 2. Live-cell time-lapse of Venus-synaptopodin and mCherry-ZO-1 showing contractions of apical stress fibers concomitant with reshaping of cell boundary and junction remodeling.

Video 3.   **Live-cell time-lapse of Venus-synaptopodin and mCherry-ZO-1 showing retrograde flow of synaptopodin from the basal cell junctions.**

Video 4.   **Live-cell time-lapse of Venus-synaptopodin and mCherry-ZO-1 showing contractions of basal stress fibers and retrograde flow of synaptopodin from the basal cell junctions.**

Video 5.   **Live-cell time-lapse of Venus-synaptopodin and mCherry-vinculin showing retrograde flow of synaptopodin from the basal cell junction.** Venus-synaptopodin and mCherry-vinculin are expressed in two neighboring cells showing synaptopodin stress fibers inserted at sites of vinculin enrichment in the neighboring cell.

Video 6.   **Live-cell time-lapse of Venus-synaptopodin and mCherry-ZO-1 showing retrograde flow of synaptopodin from the apical cell junction.** Synaptopodin network originated from the apical junction contracts to remodel the apical junction and the apical domain.

Video 7.   **Live-cell time-lapse of Venus-synaptopodin and mCherry-ZO-1 showing retrograde flow of synaptopodin from the apical cell junction.** Synaptopodin network originated from the apical junction has oscillating contractile behaviors and contracts to remodel the apical junction.

Video 8.   **Live-cell time-lapse of Venus-synaptopodin and mCherry-ZO-1 showing retrograde flow of synaptopodin from the apical cell junction.** Synaptopodin network originated from the apical junction has oscillating contractile behaviors and contracts to remodel the apical junction.

Video 9.   **Live-cell time-lapse of Venus-synaptopodin and mCherry-ZO-1 showing retrograde flow of synaptopodin from the apical cell junction.** Rows of synaptopodin originated from the apical junction has oscillating contractile behaviors.

Video 10.   **Live-cell time-lapse of Venus-synaptopodin and mCherry-ZO-1 showing clustering of ZO-1 complexes during contractions of synaptopodin stress fibers parallel to the apical cell junction.**

Video 11.   **Live-cell time-lapse of Venus-synaptopodin and mCherry-ZO-1 showing clustering of ZO-1 complexes during contractions of synaptopodin stress fibers parallel to the apical cell junction.**

Video 12.   **Live-cell time-lapse of Venus-synaptopodin and mCherry-ZO-1 showing clustering of ZO-1 complexes during contractions of synaptopodin stress fibers parallel to the apical cell junction.**

Video 13.   **Live-cell time-lapse of Venus-synaptopodin and mCherry-ZO-1 showing clustering of ZO-1 complexes during contractions of synaptopodin stress fibers parallel to the apical cell junction.**

Video 14.   **Live-cell time-lapse of Venus-synaptopodin and mCherry-ZO-1 showing anterograde movement of synaptopodin towards the junction vertex with concomitant movement of ZO-1 complexes towards the vertex.**

Video 15. **Live-cell time-lapse of Venus-synaptopodin and mCherry-ZO-1 showing anterograde movement of synaptopodin towards the junction vertex with concomitant movement of ZO-1 complexes towards the vertex.**

Video 16. **Live-cell time-lapse of Venus-synaptopodin and mCherry-ZO-1 showing motility of 2 vertices towards each other.**

Video 17. **Live-cell time-lapse of Venus-synaptopodin and mCherry-ZO-1 showing anterograde movement of synaptopodin concomitant with gliding of a contractomere along the junction.**

Video 18. **Live-cell time-lapse of Venus-synaptopodin showing oscillating behavior of contractomeres along the junctions in maturing monolayer.**

Video 19. **Live-cell time-lapse of Venus-synaptopodin showing oscillating behavior of contractomeres in mature monolayer.**

Video 20. **Live-cell time-lapse of Venus-synaptopodin showing oscillating behavior of contractomeres in mature monolayer.**

Video 21. **Structured-illumination live-cell time-lapse of Venus-synaptopodin and mCherry-ZO-1 showing wiggling of apical junction and oscillation of contractomeres in mature monolayer.**

Video 22. **Structured-illumination live-cell time-lapse of Venus-synaptopodin and mCherry-ZO-1 showing wiggling of apical junction and oscillation of contractomeres in mature monolayer.**

Video 23. **Structured-illumination live-cell time-lapse of Venus-synaptopodin and mCherry-ZO-1 showing wiggling of apical junction, oscillation of contractomeres in mature monolayer, and removal of synaptopodin along the junction during maturation.**

Video 24. **Live-cell time-lapse of mCherry-ZO-1 showing wiggling of apical junction and oscillation of contractomeres in mature monolayer.**

Video 25. **Live-cell time-lapse of venus-alpha-actinin-1 showing contractomere movement during apoptotic cell extrusion.** Blebbing of apoptotic cell is concomitant with cell extrusion.

Video 26. **Live-cell time-lapse of venus-alpha-actinin-1 in 4 focal planes showing contractomere movement during cell extrusion.**

Video 27. **Live-cell time-lapse of venus-alpha-actinin-1 showing contractomere movement during cell extrusion.**

Video 28. **Structured-illumination live-cell time-lapse of Venus-alpha-actinin-1 showing contractomere movement during live-cell extrusion.**

Video 29. **Structured-illumination live-cell time-lapse of Venus-alpha-actinin-1 showing contractomere movement during apoptotic cell extrusion.** Blebbing of apoptotic cell is concomitant with cell extrusion.

Video 30. **Live-cell time-lapse of mEmerald-occludin showing 3 cell extrusion events in a mature monolayer.**

Video 31. **Live-cell time-lapse of mEmerald-occludin showing 1 cell extrusion event in a mature monolayer.**

Video 32. **Live-cell time-lapse of Venus-synaptopodin and mCherry-ZO-1 in maturing monolayer showing wiggling of apical stress fibers in one cell and contractomere motility in an extruding neighboring cell.**

Video 33. **Live-cell time-lapse of mEmerald-occludin showing 3 cell extrusion events in a mature monolayer.**

Video 34. **Live-cell time-lapse of mEmerald-occludin showing 1 cell extrusion event in a mature monolayer.**

Video 35. **Live-cell time-lapse of mEmerald-occludin showing 1 cell extrusion event in a mature monolayer.**